UILU-ENG-95-2007

CIVIL ENGINEERING STUDIES
Hydraulic Engineering Series No. 45

ISSN: 0442-1744

FLOW STRUCTURE AND MIXING CHARACTERISTICS IN SALINE GRAVITY CURRENT FRONTS

By

Jeffrey D. Parsons

Marcelo H. García

Sponsored by
Office of Naval Research
Marine Geology and Geophysics Program
Grant N00014-93-1-0044
Grant N00014-94-1-0843 (AASERT)

DEPARTMENT OF CIVIL ENGINEERING
UNIVERSITY OF ILLINOIS AT URBANA-CHAMPAIGN
URBANA, ILLINOIS

September 1995

ABSTRACT

Saline gravity currents were studied in a steady-state reference frame with the aid of a laboratory facility. The facility, motivated by earlier work, was larger than any similar system. Its size allowed for observations of scale effects which were, until this point, undiscovered.

These scale effects were evident in the bulk dimensionless parameters of the flow as well as in the internal flow structure. The most striking differences appeared in the dimensionless mixing rate. This parameter was in some cases two to three times larger than in previous small-scale work, despite bulk densimetric Froude numbers being identical to earlier experiments. After reproducing the small-scale findings, dependence on a newly formulated Reynolds number was found. A simple relationship relating the dimensionless mixing rate to the dimensionless height, or height ratio, of the currents was also set forth for physically realizable, large-scale flows. Dimensionless mixing rates reached a maximum value of approximately 0.3, above which the fronts became extremely unstable and impossible to arrest. Accounting for the apparent invalidation of one-dimensional continuity (*i.e.*, an increase in mixing without an increase in size) meant that internal differences were present. Mean velocity and density profiles also varied from what was previously measured. Modifying previously formulated theory accounted for these differences in internal structure and matched experimental data fairly well. These internal differences demonstrate the need for modeling the vertical structure of gravity current fronts in nature. They also validated the bulk flow, dimensionless mixing rate findings.

Finally, flow visualization allowed for qualitative verification of the assertion of large scale behavior and spatial characteristics of the mixing. Two different types of behavior seemed to be present in the mixed overflow. The first was characteristic of intermittent billow events, most likely a result of the Kelvin-Helmholtz instability. The other, which occured on a longer time scale, was observed to be more of a slow, progressive frontal movement. This second type of mixing was not present in the smaller scale experiments. Further, the results of the flow visualization revealed that a number of different eddy length scales, as should be the case for a fully turbulent flow, were present in the larger scale flows, but were not found in the smaller scale experiments. These differences most likely manifested themselves in the differences in mean structure and bulk flow behavior found in the earlier experiments.

ACKNOWLEDGMENTS

We gratefully acknowledge the support of Dr. Joseph Kravitz and the Marine Geology and Geophysics Program of the Office of Naval Research. The work was completed under Grant N00014-93-1-0044 and Grant N00014-94-1-0843 (AASERT).

The work reported herein is part of a effort to understand the mechanics of sediment transport by gravity currents in continental shelves and slopes.

The impeccable design of the flume and its construction was possible thanks to the skills of Sig Anderson and his company, Engineering Laboratory Design, Inc., Lake City, MN. In the early stages of the experimental work, the help of Chris Dagiantis was crucial for 'debugging' the facility. Tony Dill also aided in the arrangement of the video and image acquisition equipment. Thanks also go to Dr. Yarko Niño (now of the University of Chile), Sung-Uk Choi and Fabián López for their many enlightening discussions as to the content of the final work.

This report is based on the Master's thesis of the first author under the supervision of the second author.

TABLE OF CONTENTS

LIST OF FIGURES

Figure Page

Figure Page

LIST OF SYMBOLS

A	fraction of the available light received
ADV	Acoustic Doppler Velocimeter
B	condensed variable in model equation
BS	Britter and Simpson (1978)
b	distance to point of interest from laser source
C	concentration of salt
C'	fluctuation in concentration of salt (or contaminant)
C_0	concentration of salt in the underflow (C(h=0))
c	concentration of fluorescein
D_d	turbulent (kinematic) eddy diffusivity
E	extinction coefficient of fluorescent dye
f	square of densimetric Froude number with respect to total water depth
g	acceleration due to gravity
g'	reduced gravitational acceleration due to excess density
h	height above zero velocity point
h_1	total water depth
h_2	height of clear water above front to the water surface
h_3	height of overflow (vertical distance between top of front to point of zero velocity in the laboratory reference frame)
h_4	height of underflow (vertical distance between zero velocity point and the bed)
h_5	visible height of the current behind the front
I_f	intensity of light received by camera
I_0	intensity of light emitted from laser
i	counter
L	side width of pixel
LIF	Laser-Induced Fluorescence
LUT	look-up table
n	exponent in the power-law expression for the concentration in the overflow
N	total number of samples
P	nonlinear incorporation of densimetric Froude and Reynolds number
Q	total flow rate of dense fluid mixed out of the front
q	flow rate per unit width into the front (equal to the mixing rate per unit width in the steady-state laboratory setup)
R_{xx}	autocorrelation of signal x

Re_f	Reynolds number with respect to entire front
Re_q	Reynolds number with respect to the mixing rate (internal processes)
r	number of samples lagged
TKE	turbulent kinetic energy
Δt	length of time between samples
U	velocity
U_1	oncoming flow velocity (constant with depth)
U_2	velocity above front (constant with depth)
U_4	velocity in underflow (if it is constant)
$\overline{U_4}$	mean velocity in the underflow (when it is not constant)
ΔU	velocity difference within billow used in definition of Richardson number
u'	streamwise fluctuation rms (or fluctuation, depending on use)
v'	lateral fluctuation rms
w'	vertical fluctuation rms
$\overline{w'c'}$	Reynolds flux
x	condensed variable in model equation
x_i	ith sample (signal)
α	shape factor relating momentum in the overflow
β	shape factor relating a kind of mixing efficiency
χ	coefficient for square term in cubic expression of velocity in the overflow
γ,ε	shape factors relating concentration in the overflow
δ	shape factor relating the square of velocity (mean kinetic energy) in the overflow
Φ	function of dimensionless variables
ϕ	height ratio of current to total flow depth
φ	quantum yield of fluorescence
μ	dimensionless mixing rate
ν	kinematic viscosity
ρ	density
θ	constant term in cubic expression of velocity in the overflow
ξ	coefficient for cubic term in cubic expression for velocity in the overflow; also is a simple function of the slope of the velocity profile at the zero velocity point
ψ	condensed variable in model equation
ζ	linear coefficient in cubic expression of the velocity in the overflow

1. INTRODUCTION

1.1 Generalities

Density differences are ubiquitous in nature. Under certain conditions, these density differences can manifest themselves into a gravity current. Gravity currents can be generated by differences in salinity, temperature or sediment concentration. These currents have been hypothesized to be important vehicles for contaminant and sediment transport in natural waters.

Problems in understanding this phenomenon arise because it is a complex process occurring in relatively inaccessible environments (*e.g.*, the bottom of the ocean, in the middle of extremely violent volcanic eruptions). A few studies of the dynamics of gravity current fronts using remote sensing technology have been attempted recently (*e.g.*, Hay, 1983, 1987; Inman et al, 1976). The results, however, could only describe the bulk parameters of the flow, and with considerable margin for error. Therefore, laboratory modeling provides a venue for understanding the internal structure of these fronts. Only recently, however, researchers have begun to understand the complex relationships between the numerous variables which regulate the development and propagation of gravity currents.

An important component of a current front is the amount of mixing that occurs there. Mixing not only regulates the speed at which the current propagates through the ambient fluid, but also determines how much of the contaminant will be moved by the flow. In turbidity currents, sediment laden flows, erosion and deposition at the bed also control the rate of propagation. All of these mechanisms regulate the flow because they alter the driving force of the front; the excess density difference.

According to Allen (1972), mixing occurs through several processes. The first, and probably most important, is the generation of billows due to Kelvin-Helmholtz instabilities at the 'head' of the front. Kelvin-Helmholtz instabilities manifest themselves in large billows that roll over the top of the front and continue propagating with it until they are dissipated by viscosity. Thorpe (1971, 1973) did considerable work on the subject, but research still continues today (*e.g.*, Sullivan and List, 1994). Additional mixing is due to 'lobes and clefts'. Lobes and clefts, that often combine and split unpredictably, have been speculated to be caused by flow underneath the elevated stagnation point at the very tip of the current, the so called nose. Flow underneath the nose, a result of the no-slip boundary condition, induces additional mixing of clear water underneath the front. A quantitative relationship between these latter types of mixing and the bulk flow parameters has yet to be ascertained.

Unsteadiness in gravity currents has also prohibited geophysicists and engineers from understanding and quantifying the structure and mixing of the flow. These currents evolve in time,

therefore, distance along their path, making data acquisition extremely difficult. In traditional, channelized 'lock-exchange' experiments, predicting the propagation speed of a front is necessary for understanding it. This paradox has plagued researchers intent on using traditional methods.

Pioneer work done by John Simpson and his colleagues in the late 1970's and early 1980's attempted to correct for this unsteadiness problem. Though their work provided considerable insight into the frontal mixing of saline gravity currents, several problems were incurred during the course of their experiments. These difficulties inspired the construction of the facility used in the present study. A picture of the facility, just after construction, is shown as Fig 1.1.

Later in this chapter, a literature review concerning works of Simpson, as well as a few others, is given. Chapter 2 describes the facility in detail. In Chapter 3, a basic dimensionless analysis of the fronts, as well as the general experimental procedure, is given along with the results from the initial runs. The discussion that accompanies the initial bulk flow runs is contained in Chapter 5. Chapter 4 presents the modified theory of Benjamin (1968) along with the adjusted velocity and concentration profiles obtained from the early experiments. This chapter also includes the results corresponding to the new interpretation of the profile. Further, experiments examining the spatial structure of the fronts and their turbulence characteristics are presented in this chapter. Analysis of both the mean and turbulent internal flow structure experiments is included in Chapter 6. Finally, Chapter 7 not only summarizes all of the results of experiments performed in the duration of the study, but also presents a plan for future work with the facility.

1.2 Early Results and Basic Theory

Prior to the 1940's, experiments performed on saline gravity currents were primarily of qualitative nature (*e.g.*, Schmidt in 1910 and Kuenen in the 1930's, from Middleton, 1966). The first researchers to consider the problem within a quantitative framework were von Karman (1940) and Keulegan (1957a, 1958). They also established the basis for the dimensionless equations that are now used to describe the nature of gravity currents. Von Karman (1940) used the Bernoulli equation, with the improper assumption of irrotational flow, to describe density currents. This classic mistake is noted in many hydraulic classes and warns budding engineers of the danger of overusing simplified equations. On the other hand, the work of Keulegan (1957a, 1958) was based on experiments of saline gravity currents. His studies, considered classic among researchers in this field, were exhaustive and incredibly advanced for their time. The range of his data covered a larger scope of dimensionless parameters (with the possible exception of Tesaker, 1969) than any set of works to date. However, due to the inherent unsteady nature of the front, only Froude and Reynolds numbers and geometric relations could be ascertained. Keulegan reflected upon the lack of data on internal velocity and density characteristics as a drawback of the work. Despite these

shortcomings, both researchers were the first to realize that dense fluid mixing with the lighter one has a strong impact on the propagation velocity and other geometric relations.

Benjamin (1968) disproved the use of the Bernoulli equation for gravity currents, as done by von Karman (1940), and set forth the most comprehensive, workable theory to date. Benjamin used the Boussinessq approximation and boundary-layer flow theory to simplify the incompressible form of the equations of motion to the point where dimensionless parameters could be analytically solved for, for all possible fronts. Although his primary application was air intruding into a narrow, emptying duct, his theory can be easily and justly applied to the case of a denser fluid (saline or sediment-laden) intruding at the bottom of larger, quiescent body of water. The theory of Benjamin (1968) was an integral part of the works of Simpson (Britter and Simpson, 1978; Simpson and Britter, 1979). Because of this, Benjamin (1968) will be discussed at greater length in the following section where Britter and Simpson (1978) and Simpson and Britter (1979) are presented.

As mentioned earlier, the Kelvin-Helmholtz instability, and the turbulence it produces, is the primary driving force of mixing between the two layers. One of the 'oldest' instabilities, the Kelvin-Helmholtz instability was first remarked upon by Helmholtz in 1868 and formally posed by Kelvin in 1871. Considerable analytical work has been done since on the subject by some of the most famous applied mathematicians of our time (Drazin and Reid, 1981; Taylor, 1950). The first 'modern' experiment was carried out by Thorpe (1969, 1971, 1973) and consisted of a small-scale (45 cm long), thin duct, filled with colored brine (in the case of the miscible experiments of 1971 and 1973) and water. Tilting the duct creates shear at the surface between the two fluids which, in turn, creates an instability. The billows created grow with time until reaching a critical size, after which they are dissipated. The eloquent theory formulated by Thorpe (1973) revolves around a Richardson number which relates the density difference and the billow size to the velocity difference in the two layers. He concluded that the Richardson number would reach an asymptotic value (approximately equal to 0.35) after a given amount of time. Britter and Simpson (1978) would later imply that the Richardson number defined by Thorpe was equal in all of his experiments because he obtained the profiles where Kelvin-Helmholtz billows reached their full equilibrium size. Turner (1973) compiled much of this early work, both mathematical and experimental, on the Kelvin-Helmholtz phenomenon and provided simple explanations to much of the complicated mathematics developed by the researchers mentioned above.

1.3 Modern Work and Mixing

The idea of setting up gravity current experiments where the front of a gravity current can be studied in stationary, steady-state reference frame is a relatively new one. In this type of facility

the front usually is arrested at the end, or on top of, a conveyor belt which moves at a velocity equal to that of the overbearing flow. Therefore, the front is arrested in time and space while the dynamics of the front appears as it would if the front was moving through still water. A complete summary and history of the various applications that employed this 'moving bed' technique is contained in Tamburrino and Gulliver (1992). They attributed the beginnings of this technique to Riabouchinsky and his experiments with air flow in 1909. They also discussed Bagnold (1974) and his classic experiment with shear effects on immersed bodies. Measurements of turbulence and velocity structure in these types of facilities were also included. One of the first goals of this study, was to reproduce this data.

The first person to explore the use of a moving-bed device for the study of saline currents was John Simpson, then at the University of Reading. He brought his flume from the University of Reading to Cambridge University where he completed an exhaustive study of gravity current fronts. Most of the current state of knowledge on gravity current fronts can be attributed to Simpson or one of his students. Preliminary work by Simpson that served as the basis for the design of his facility will not be discussed in detail, but can be found in Simpson (1969, 1972).

Britter and Simpson (1978), hereafter referred to as BS, was the first in a series of papers generated with the help of such an apparatus. This work also has the most relevance to the work presented here, particularly in Chapters 3, 4 and 5. In the introduction, BS described their facility and the differences between salt wedges and saline fronts. The difference between these two phenomena is in the boundary layer, or lack thereof, in the clear water flow. In salt wedges, as has been examined by Keulegan (1957b) and others, the boundary layer in the clear water is fully developed (as a river flowing into the ocean) and mixing between the two fluids, dense and clear, is virtually nonexistent. In saline fronts, however, the dense fluid is propagating into quiescent clear fluid and no boundary layer exists. As BS pointed out, this is simply the Galilean transformed system of the laboratory apparatus of their study. In this case (*i.e.*, saline fronts), mixing does exist and plays an important role in regulating the behavior of the flow field as a whole. Next, BS proceeded to present their version of the theory of Benjamin (1968).

The original theory of Benjamin (1968) was developed for an air cavity propagating though a duct filled with water. This theory, therefore, was developed for immiscible fluids only. In addition to assuming immiscibility, Benjamin assumed the flows to be two-dimensional, incompressible, steady and inviscid. He also applied the boundary layer approximation (*i.e.*, length scales in the vertical are small when compared to longitudinal length scales, and changes in the direction normal to the flow are much greater than changes in the longitudinal). Along with the Boussinessq approximation (ignoring buoyancy effects, except for in the body force terms) and some geometric constraints the equations of motion were simplified significantly to a closed-form solution. The final solution has the dependent variable as the thickness of the current downstream

of the front and the independent variable in the form of a densimetric Froude number of the quiescent fluid.

The modified theory of BS included effects caused by the mixing between the two fluids. This complication yielded another dimensionless, independent variable; namely, a dimensionless mixing rate or mixing Richardson number. In addition, shape factors, which would need to be found experimentally, were introduced to account for the distribution of the mixing and velocity in the mixing layer. They assumed a form of the velocity and density profiles, where the underflow of dense fluid was constant (both in velocity and density) and the variable of interest varied as a power law in the mixing region. With these assumptions, a closed form solution was found, though it was more complex than the immiscible case. BS compared their experimental data to the adapted theory and found reasonably good results. This is despite the fact that their basis for mixing insensitivity to Reynolds number was based on the work of Keulegan (1958) which only accounted for Froude number effects. The primary difficulty encountered was measuring the mixing rate. Because of the characteristics of the apparatus, short-circuiting of dense fluid was a serious problem. Short-circuiting occurs when the dense fluid gets pulled over the weir (because of the high velocities there) without propagating along the bed into the channel and forming a density current. This loss could have been prevented (or at least minimized) with the use of a guard plate, as in the experiments herein. In order to account only for the amount of dense fluid mixed out by the density current front, they measured mixing rates in the channel by integrating a velocity profile near the front. They used dye streak measurements to measure the velocity (they used a hot-film for the overflow velocity profiles, however). Although integrating a dye streak velocity profile was found to be the best way to measure mixing rates, errors using this method were estimated to be about 30%. Though, they did not show a plot, or give a quantitative relationship, they later described in Thomas and Simpson (1985) that the dimensionless mixing rate found in these experiments was "approximately 0.15 and a weak function of h_4/h_1 [the height ratio, where h_4 is the height of the current behind the front and h_1 is the total flow depth]".

The discussion and conclusions of BS centered around comparison to the work of Thorpe (1973) and the limit of the height ratio or dimensionless thickness of the current going to zero. They acknowledged that Thorpe was correct in assuming an equilibrium Richardson number, defined by the velocity difference across the mixing region and length and density difference of that mixing region. The discussion of how their theory would apply to extremely deep flows (small dimensionless thickness or height ratio) continued with various attempts at obtaining a simple solution to the complex equations, however, nothing was proposed. No discussion of viscous effects, the combination of viscous and scale effects on their fronts, or graphs of Reynolds numbers versus other parameters of the flow were presented. Also, no discussion of the internal turbulence generated by the fronts was shown.

The next effort by the Simpson team was Simpson and Britter (1979). In this work, they followed virtually the same procedures as in BS. However, here, they discussed the effects of a no-slip boundary condition on the theory. The original theory of Benjamin and BS was designed for a moving bed. Although this is unrealistic for real environmental problems, its simplicity and ease to manipulate both in the lab and on paper make it preferable to work with, as will be shown later. The differences between the two situations were found to be relatively small. Again, because of their experimental method and setup, this run of experiments proved to generate less error than the movable experiments. Nevertheless, the error was still larger than the error accounted for in the experiments presented herein. Simpson and Britter (1979), unlike BS, presented a graph of some of their dimensionless mixing rate data. The data fell on somewhat of a line with an intercept near the origin and slope of about one. Simpson and Britter (1979) also included a section on Reynolds number effects in their discussion. They quote field numbers, derived in part from their theory, of dimensionless mixing rates of 0.35 for relatively shallow flows. Though their observations would predict a value nearly 50% less than this, an explanation of the difference merely stated that the field results "are larger but still comparable to the laboratory results." Most of the discussion of Reynolds number, however, effects centered around comparison of densimetric Froude numbers with other laboratory researchers working with large-scale lock-exchange flows (*e.g.*, Keulegan, 1958).

Later works, like Thomas and Simpson (1985) and Simpson (1986), focused on the effects of a turbulent environment on the mixing and other parameters of the arrested saline gravity currents. Both of the above works described the mixing of their apparatus as a function strictly of background turbulent intensity. The fronts seemed to lose their identity (as in Figure 4, Thomas and Simpson, 1985) at high background turbulent intensities and began to look more like gravity layers. This phenomenon was also studied by Thomas and Simpson (1985) for this reason. At high turbulent intensities, the dimensionless mixing rates are also large and seem to be proportional to the length of the current exposed to the flow. Gravity layers also behave in this way. However, neither work established a quantitative relationship between the turbulent intensity of the background and the rest of the parameters. Also, little evidence was provided on how the data collected could be used for quantitative analysis of environmental-scale flows. One section of Thomas and Simpson (1985) proposed a general form of the equation that would describe how the turbulence and the mixing interact to regulate the fronts propagation velocity. The arguments that they proposed, however, were speculative and could be used only as first-order approximations.

Despite this considerable body of work on conservative, saline gravity currents, little work has been done in quantifying mixing in non-conservative, sediment-laden (turbidity) currents. Though most of the knowledge learned from saline gravity currents can be applied to fine sediment, virtually conservative turbidity currents (García, 1993), a steady-state, laboratory

examination of turbidity currents would be helpful in determining mixing rates in natural non-conservative flows (*i.e.*, turbidity currents on the continental shelf). Due to the unsteady nature of the front in traditional density current experiments (*e.g.*, Middleton, 1966; Altinakar et al, 1990), mixing has been almost impossible to quantify. Future work, outside of the scope of the current study, will be started on this problem with the facility presented herein.

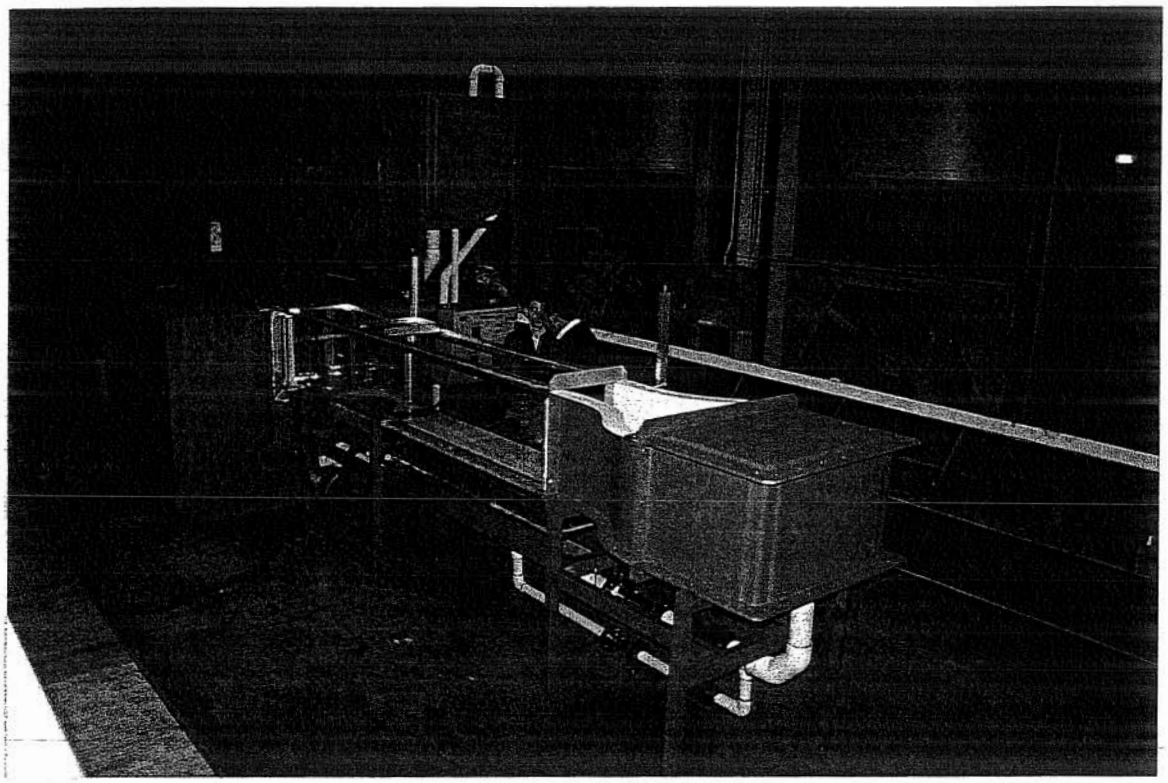

Figure 1.1 Picture of steady-state gravity current facility with graduate student and advisor for scale

2. EXPERIMENTAL FACILITY

The facility used to arrest the fronts of steady-state saline gravity currents was designed by Marcelo García of the University of Illinois and Sig Anderson of Engineering Laboratory Design, Inc. of Lake City, MN. Fig 1.1 shows a picture of the facility just after manufacture and a small copy of its blueprints can be seen in Fig 2.1 and 2.2. Fig 2.3 gives a schematic flow diagram of the system. Dimensions, along with descriptions of particular features, are included for reference and as an explanation to the figures mentioned above.

The facility consists of two components, a saline portion and a clear (uncontaminated) water portion. The clear water portion begins with a 4000 L tailbox. A 3-phase, 60 Hz, 1.5 HP pump with a bronze-lined impeller is attached to the base of this tank and drives the closed-circuit clear water portion. An approximately 8 cm diameter pipe connects the tailbox to the headbox. A venturi along this line measures the flow rate in the clear water section. It is capable, with a built-in manometer, of measuring anywhere between 1 L/s and approximately 12 L/s. The headbox outlet has a honeycomb flow straightener which controls the size of the eddies leaving the headbox. The headbox narrows, after the straightener, to a 30 cm wide by 50 cm high channel. The channel is 3.2 m long, from contraction to weir, with a conveyor belt for the first 1.5 m (proceeding from the headbox). The belt is controlled by a 1/4 HP motor which can move the belt, and thus the bed, up to 25 cm/s. A main control box controls both the conveyor belt and the pump. Different panels on the main control box adjust the frequency of each motor. The remaining portion of the bed (about 1.7 m) has a portion (about 75 cm, 5 cm from the toe of the belt) containing a false bottom which was not used in the experiments herein, but will be important in future erodible bed studies. Finally, a slot valve (discussed later in the saline portion) and an adjustable weir are located at the end of the channel. The adjustable weir can be varied the entire height of the channel (0-50 cm) and regulates the discharge and the flow depth.

The saline portion of the system begins in the saline holding tank, or mixing tank. Like the clear water portion, this tank also has a capacity of 4000 L. However, it also has a stirring mechanism consisting of a 1/16 HP motor connected to a shaft with three, 5 cm blades, capable of rotating at 1750 Hz. These blades generate the turbulence that mixes the salt used in the experiments. The base of the mixing tank contains a 3-phase, 1/4 HP, 60 Hz pump with a bronze lined impeller which pumps the saline water up to the constant head tank. If fluid flows over a weir inside the tank that is 3 m above the laboratory floor, this excess fluid discharges back to the mixing tank. This provides additional turbulence to counteract stratification. Another pipe (about 2 cm in diameter) coming out the bottom of the constant head tank leads to the slot valve in the channel. Along this line another venturi measures the flow rate of the dense fluid delivered to the channel. In the case of steady-state, arrested currents, this corresponds to the mixing rate of the

current (by continuity). A ball valve located just below the venturi regulates the flow of dense fluid to the channel. Before the slot valve, but after the venturi, a Plexiglas section allows flow to gradually widen. This prevents flow separation . On top of the slot valve a 30 x 30 cm guard plate prevents short-circuiting. The dense flow enters along the bottom of the channel at this point. As the dense flow reaches the belt, mixing initiates and gravity front behavior is achieved. The front can be arrested anywhere along the top of the belt or at the toe (end) of the belt by regulating the discharge of dense fluid.

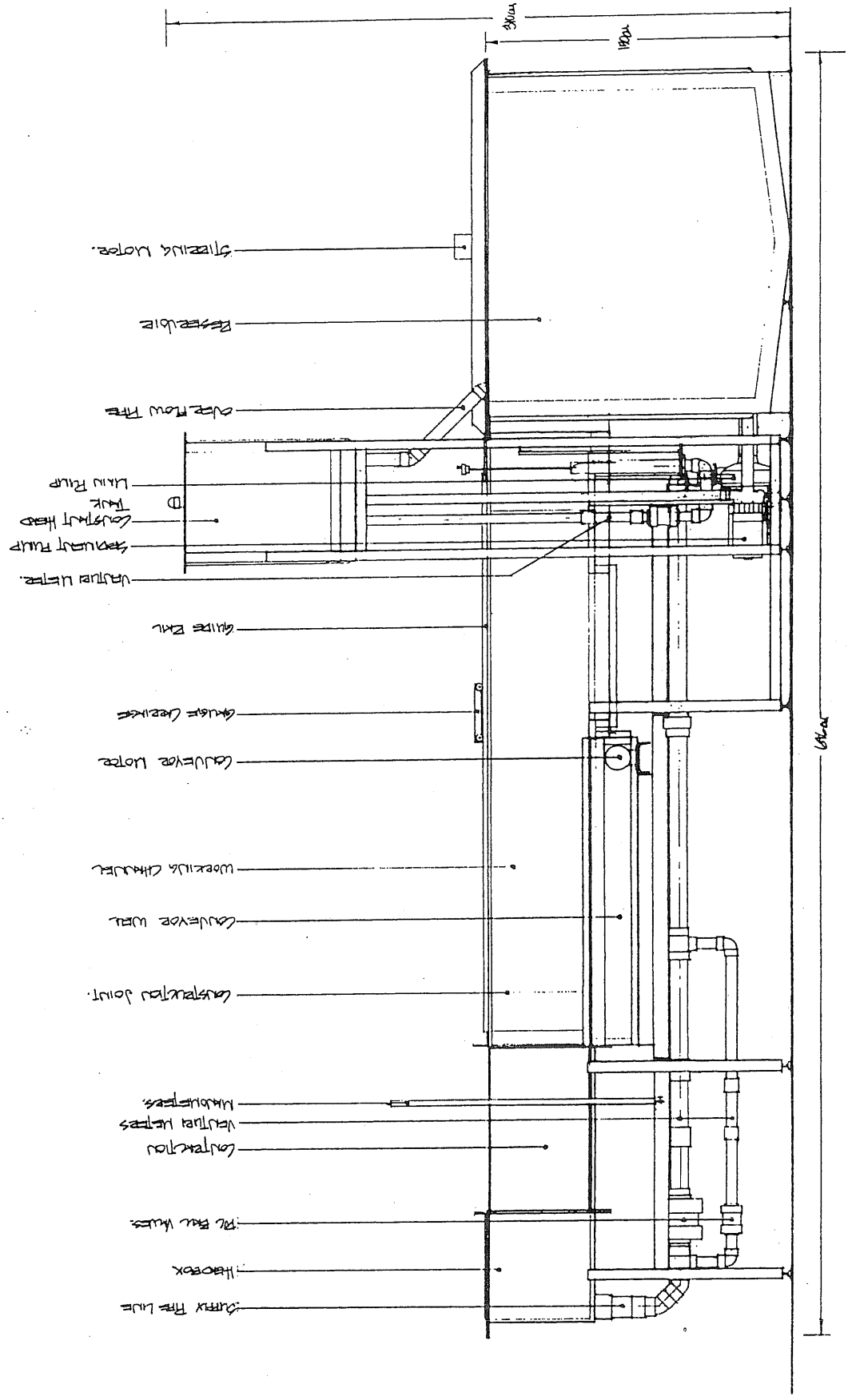

Figure 2.1 Side view of experimental facility

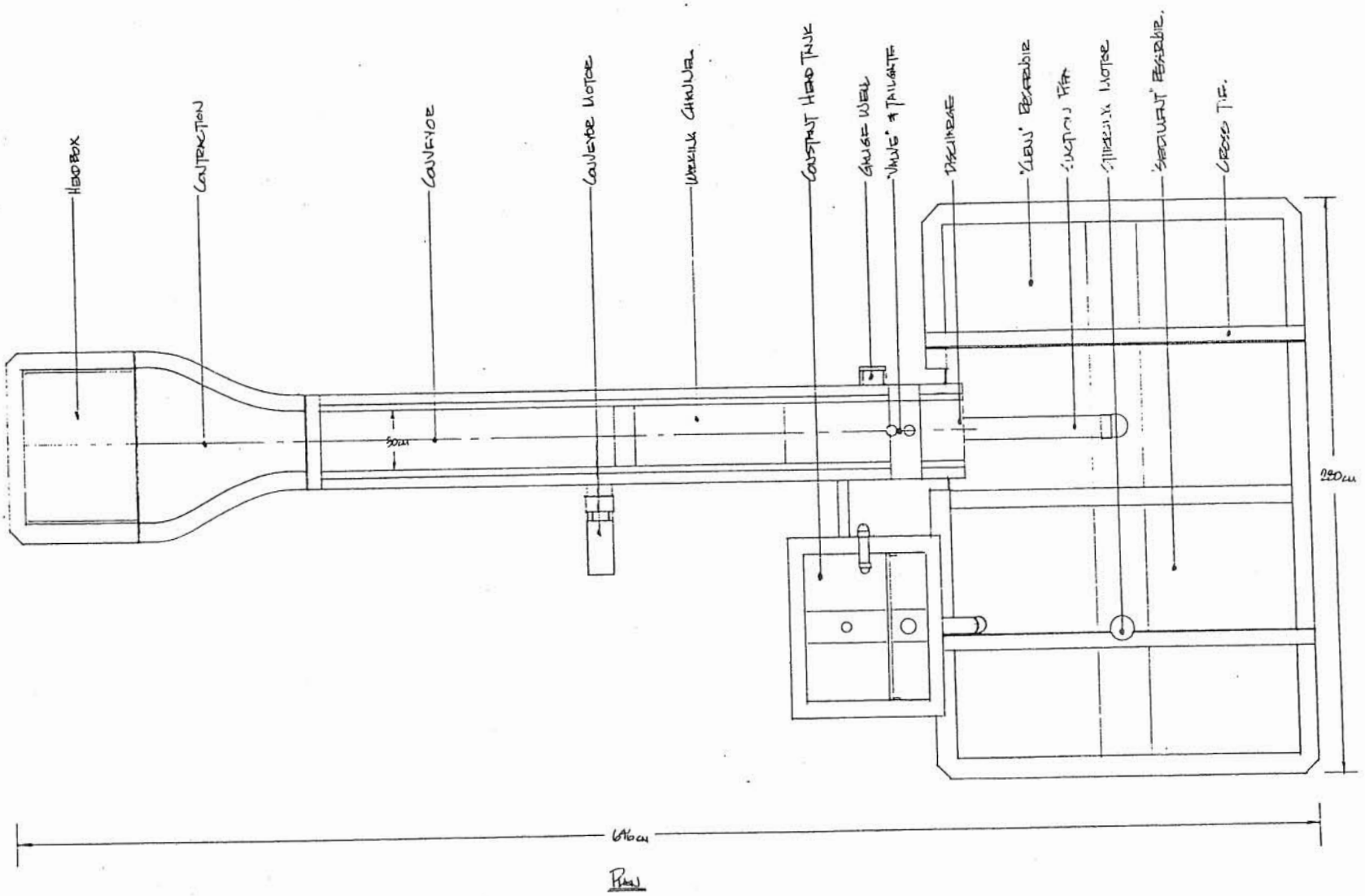

Figure 2.2 Plan view of experimental facility

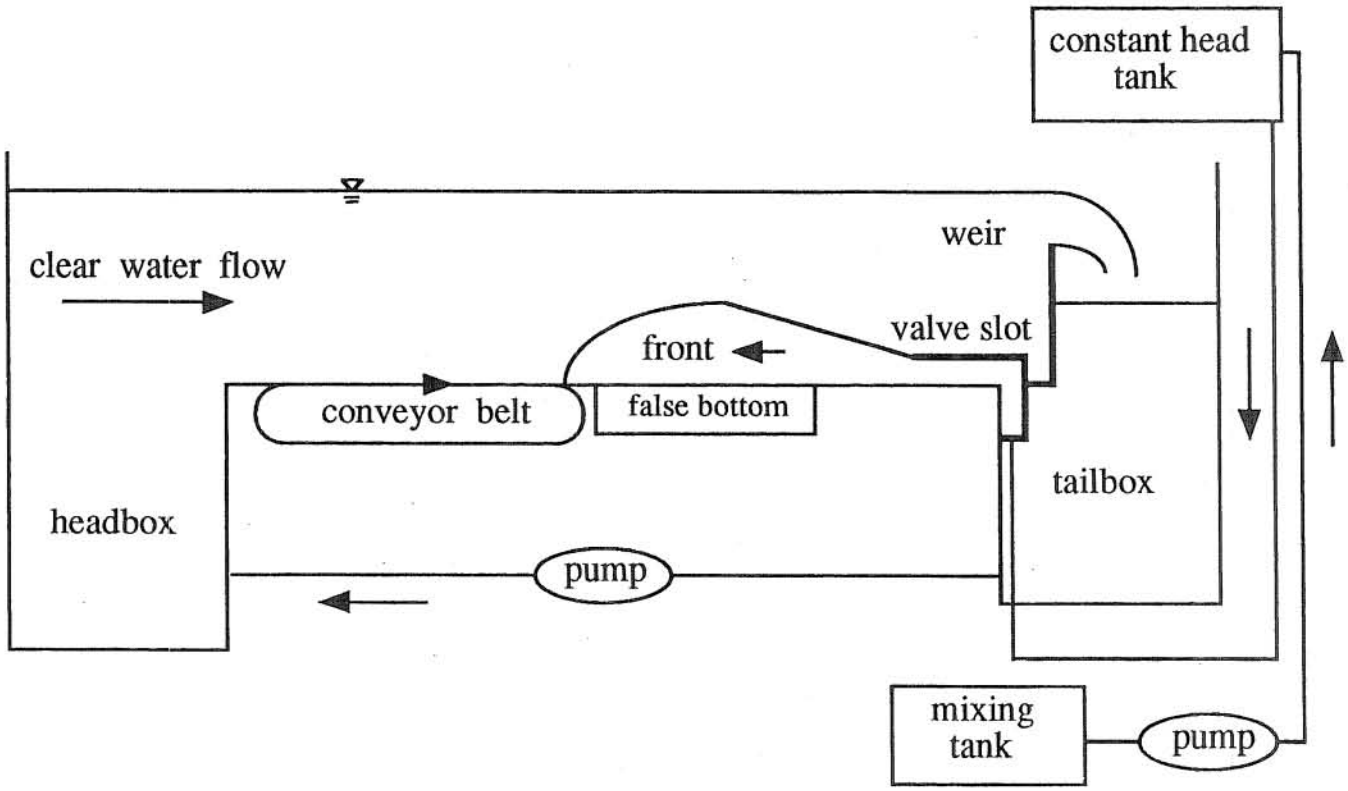

Figure 2.3 Schematic of steady-state gravity current facility

3. BULK FLOW EXPERIMENTS

3.1 Generalities

One of the main goals of this study was to understand how the facility operates and realize its limitations and strengths. This was easiest accomplished by setting up several different runs, under a wide range of conditions, trying to generate and arrest the currents. In this first set of experiments, only the bulk flow parameters were measured (*e.g.*, the total mixing rate, front velocity, front height, *etc.*). Dimensional analysis used by BS and originally proposed by Benjamin (1968) formed the basis for the analysis. In this portion of the study, the primary objective was to reproduce BS and Simpson and Britter (1979) results to ensure that the flume was performing properly.

In addition to fundamental calibration of the facility, a simpler model was hoped to be found that would be independent of possible scale effects encountered by BS and Simpson and Britter (1979). The rather complicated BS model presented in Section 2 of this chapter requires a relatively detailed code for generating all three of the important dimensionless parameters (densimetric Froude number, Richardson number, and height ratio). Moreover, the empirical constants in the model proposed by BS can be difficult to find and verify experimentally and tend to lump many effects in a rather arbitrary way. Therefore, a simpler model would aid engineers and geophysicists in 'back of the envelope' calculations of the front velocity, mixing rate and height of fronts in the field.

3.2 Dimensional Analysis

The analysis of BS provided the basis for the discussion of theory and dimensionality. Their theory was similarly based on that of Benjamin (1968). The difference between their analysis and the one presented herein was the inclusion of viscous effects. For the benefit of the reader, the theory is illustrated from beginning to end, even though much of it can be found in BS and Benjamin (1968).

Five independent variables can describe a gravity current front: the flow velocity in the channel (U_1), the total flow depth (h_1), the reduced gravity (g') due to excess fractional density, the discharge per unit width of dense fluid (q), and the kinematic viscosity of the dense fluid (ν). These variables are shown in Fig 3.1 with their relationship to the gravity current front. The dependent variables of interest are the density current propagation velocity (U_f) and the depth of the current body behind the front (h_5). From Buckingham's Pi Theorem, the following expression can be obtained

$$\frac{U_f}{U_1}, \frac{h_5}{h_1} = \Phi_{1,2}\left(\frac{g'q}{U_1^3}, \frac{U_1}{(g'h_1)^{1/2}}, \frac{q}{\nu}\right) \tag{3.2.1}$$

For a given U_1 and h_1, the buoyancy discharge ($g'q$) can be adjusted, as in the laboratory experiments, until the velocity of the front (U_f) is equal to zero. This yields the following relationship

$$\Phi_1\left(\frac{g'q}{U_1^3}, \frac{U_1}{\sqrt{g'h_1}}, \frac{q}{\nu}\right) = 0 \tag{3.2.2}$$

which can be manipulated to

$$\frac{g'q}{U_1^3} = \Phi_3\left(\frac{U_1}{\sqrt{g'h_1}}, \frac{q}{\nu}\right) \tag{3.2.3}$$

From (3.2.2) we can also show the relationships found by BS with the addition of the Reynolds number (q/ν) term

$$\frac{U_1}{(g'h_1)^{1/2}} = \Phi_4\left(\frac{h_5}{h_1}, \frac{q}{\nu}\right) \tag{3.2.4}$$

and

$$\frac{g'q}{U_1^3} = \Phi_5\left(\frac{h_5}{h_1}, \frac{q}{\nu}\right) \tag{3.2.5}$$

In a steady state, as the one studied in the present experiments, q corresponds to the amount of dense fluid 'mixing out' of the front, as well as the flow rate in the underflow behind the front. This situation is by definition always true, but only in the mean and only for steady-state fronts. Therefore, (3.2.5) provides an expression for dimensionless mixing rates where the Reynolds number, defined by q/ν, can be considered either the Reynolds number of the current behind the front or a Reynolds number for the dimensional mixing rate. For the remainder of this study, this Reynolds number will be referred to as the mixing Reynolds number.

The most important parameter for the present study, however, is the dimensionless mixing rate; $g'q/U_1^3$. The analysis should try to obtain a function of the other parameters in terms of this. In fact, if (3.2.1) is manipulated with the help of (3.2.3) such that

$$\frac{h_5}{h_1} = \Phi_6\left(\frac{U_1}{(g'h_1)^{1/2}}, \frac{q}{\nu}\right) \tag{3.2.6}$$

then the ratio of (3.2.5) and (3.2.6) can be taken to find

$$\frac{g'q}{U_1^3} = \frac{h_5}{h_1}\Phi_7\left(\frac{U_1}{\sqrt{g'h_1}}, \frac{q}{\nu}\right) \tag{3.2.7}$$

where $\Phi_7 = \Phi_3/\Phi_6$. The dimensional analysis, however, says nothing about the character of Φ_7, and Chapter 5 will show that this function is quite complex. Again, the difference between this and the dimensional analysis of BS is that the function that they finally obtained is only a function of the Froude number $(U_1/(g'h_1)^{1/2})$ and the height ratio (h_5/h_1). Viscous effects in their theory were not considered. The impacts of this exclusion will be discussed below in Chapter 5.

3.3. Description of Experimental Technique

As mentioned previously, the purpose of the bulk flow experiments was twofold; to reproduce the data of BS and to establish the simple, linear relationship found in (3.2.7) for large scale density current fronts. The facility, as described in the preceding chapter, however, was used for all experiments reported herein. Therefore, the reader is referred to Chapter 2 for specifics about the basic operation and size of the facility. In the first type of experiments, more like flows in reality, the experiments used a high downstream weir height and were performed to assess effects of scale on the results of BS. These experiments were constrained by the height of the channel (50 cm) and the capacity of the main clear water pump. The main pump was calibrated (as will be discussed in the following paragraph) using the same head in the clear water tank for three heights of the downstream weir (22, 30, 38 cm). A Venturi meter measured flow rates in this portion of the facility at the bottom of the headbox. In the experiments designed to reproduce the results of BS, the pump was calibrated for a 15 cm weir height. At this height, it had to be run at a much lower frequency to ensure that the fronts did not short-circuit at the downstream weir. Again, short-circuiting occurred when dense fluid was entrained into the water passed over the weir without making it down the channel in the form of a density current. This was particularly pronounced for high mixing rate fronts. Therefore, the 'typical calibration' (as explained below) was invalid in this situation and the pump and the conveyor belt speed had to be calibrated before each experiment. At the other extreme, measuring smaller flow rates (< 100 cm^3/s) of dense fluid

accurately became increasingly difficulty at smaller scales. However, a window of feasibility was found between these two extremes for the 15 cm weir height.

Because the Venturi meter at the upstream headbox was undersized for the facility, the measurements contained considerable fluctuations (approximately 5%) from the nearby pump. These fluctuations were difficult to separate when the reading was recorded manually. However, consistency and manageability became possible by calibrating the main pump for a given mean flow velocity. This was accomplished by equating the main pump frequency denoted on the main control box to mean velocity in the channel. The mean flow velocity was calculated from the flow rate divided by the cross-sectional area. The flow rate was measured from a Venturi meter mounted just downstream of the pump, while the flow depth was measured using a point gauge. Channel flow width was fixed at 30 cm. The head behind the pump remained constant for all of the runs with little variation during each experiment.

The conveyor belt speed was controlled similarly with another meter at the main control box. The frequency read at the main control box (corresponding to the conveyor belt) was calibrated to the conveyor belt speed. Therefore, the main pump (calibrated to a mean flow speed) and the conveyor belt could be matched for a given weir height. Matching meant that the mean flow velocity in the channel was equal to conveyor belt speed. This ensures a constant, uniform velocity profile (*i.e.*, no boundary layer) and was previously referred to as the 'typical calibration'. This, however, requires different calibrations for different weir heights. The final calibration for each of the three weir heights used in these experiments resulted in a well-correlated linear relationship which can be seen in Fig 3.2. This occurred because the speed of conveyor belt was obviously linearly related to its frequency, and the mean velocity of the flow was linearly related to the frequency of the motor in the range of frequencies used in these experiments. Another reason for the high correlation was that the calibration procedure was performed twice, once to find the approximate belt speed for a given flow rate, and a second time for the final calibration. Difficulties occurred when the pump was run at well below maximum power (in the low weir height experiments, approximately half-power) and the linear relationship between the different frequencies was lost. For example, Fig 3.3 illustrates the calibration curve for the experiments that were intended to duplicate BS. In these low weir height experiments, however, fluctuations from the pump were minimal and the velocity of belt and mean velocity of the clear water flow were matched directly and individually for each experiment.

Once the saline flow reached the channel, careful monitoring of the front was needed to ensure that the front stopped at the correct point (*e.g.*, at the front seal of the conveyor belt in the moving boundary experiments, or at some point on top of the belt in the fixed boundary experiments). The amount of saline water was regulated by a ball valve located on the pipe leading from the head tank to the slot valve. A Venturi meter located just above the ball valve measured

this flow rate. Two Venturi meters with different constrictions were used in the experiments. The first Venturi meter used was a small constriction device. The ratio of the minimum diameter of the Venturi to the diameter of the pipe was 0.75. This degree of constriction did not provide enough pressure difference for accurate measurements of lower mixing rate fronts. Therefore, a more severely constricted Venturi meter (with a diameter ratio, β, of 0.47) was used which produced adequate pressure differences in most experiments. This Venturi was used in all of the low weir experiments, as well as most of the later high weir experiments. Calibration curves of the two Venturis are located in Fig 3.4.

A certain amount of time was required for the saline current to develop, or in other words, reach steady-state. Generally the current began like a saline wedge, with little to no mixing at its head, and propagated slowly to the seal. This generally took a couple of minutes depending on the mixing rate (higher mixing, less time; lower mixing, more time). After some experience, the saline mixing rate was able to be altered exclusively in this time for the front to stop at the intended point. This optimized the amount of time the front could be observed. After the front had been arrested for approximately one minute and the train of billows started to equilibrate, measurements were taken of the height of the front (h_f), the height of the current body (h_5), the total flow depth (h_1), saline flow rate (q = Q/width = Q/30cm), and the temperature of the water (T). The other parameters discussed in Section 3.2 were set beforehand, such as the reduced gravity (g') and the oncoming flow velocity (U_1). Fronts remained in this steady-state for approximately fifteen to twenty minutes, at which time the overbearing flow became slightly polluted (about 5-10% of the total density difference) with the denser fluid.

3.4. Moving Boundary Results

The raw results can be found in tabular format in Appendix 1. Note that the summary of experiments in Appendix 1 begin with experiment number 15. Early trials were run in an incoherent manner to adjust the facility and methodology (*i.e.*, some with a rough bottom, some with and without a shield plate, *etc.*) and were incomparable and meaningless to the later results. In addition, occasionally an experiment was run to push the limits of the facility and failed for a variety of reasons (*e.g.*, short-circuiting of dense fluid, inability to arrest the front, *etc.*). Therefore, the numbering of experiments in Appendix 1 (because an experiment was numbered regardless of its success) is discontinuous.

Most of the early runs were moving bed experiments (*i.e.*, the fronts were stopped at the toe of the conveyor belt). From the dimensional analysis in Section 3.2, a couple of interesting relations can be seen. First, Fig 3.5 demonstrates the relation between the Froude number ($U_1/(g'h_1)^{1/2}$) and the height ratio (h_5/h_1) with a comparison to the data range of BS. Data from

the two different sets (the study reported here and BS) collapse fairly well. However, the dimensionless mixing rate ($g'q/U_1^3$) versus the height ratio, as depicted in Fig 3.6, increased for increasing weir height, or scale of the experiment. Asymptotic behavior seemed to occur for the largest scales. An alternative Froude number ($U_1/(g'h_5)^{1/2}$) was also useful for comparison to BS because it is a parameter that will be used in the following chapter about internal flow structure. Its relation with the height ratio is seen in Fig 3.7. Two graphs relating the front Reynolds number (U_1h_f/ν) and the mixing Reynolds number (q/ν) to the height ratio can be found in Figs 3.8 and 3.9; respectively. In all of the graphs mentioned in this paragraph, the data are subdivided by the weir height they were performed at to emphasize the effects of scale on the results.

3.5. Fixed Bed Results

Only a few fixed bed experiments (*i.e.*, the fronts were arrested on top of the conveyor belt) were run over the course of the study for several reasons. The most prominent reason pertained to the internal flow structure experiments and will be discussed below in Chapter 4. Another reason was the relative invariance of the dimensionless parameters of interest due to the change in boundary condition. This is illustrated in Fig 3.10 with a graph of dimensionless mixing rate versus height ratio. A plot of the comparison in Froude numbers ($U_1/(g'h_5)^{1/2}$) is also included as Fig 3.11. Both of these graphs are for experiments run only at one weir height (30 cm). The other weir heights followed the same trends. Raw, fixed bed experimental data is available in Appendix 2.

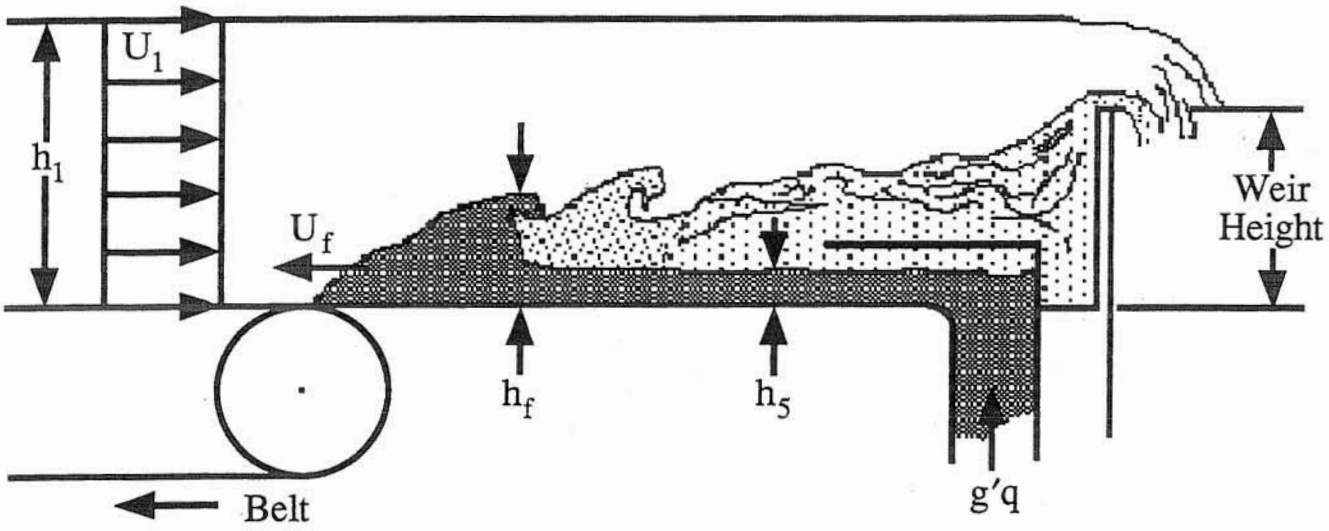

Figure 3.1 Definition diagram

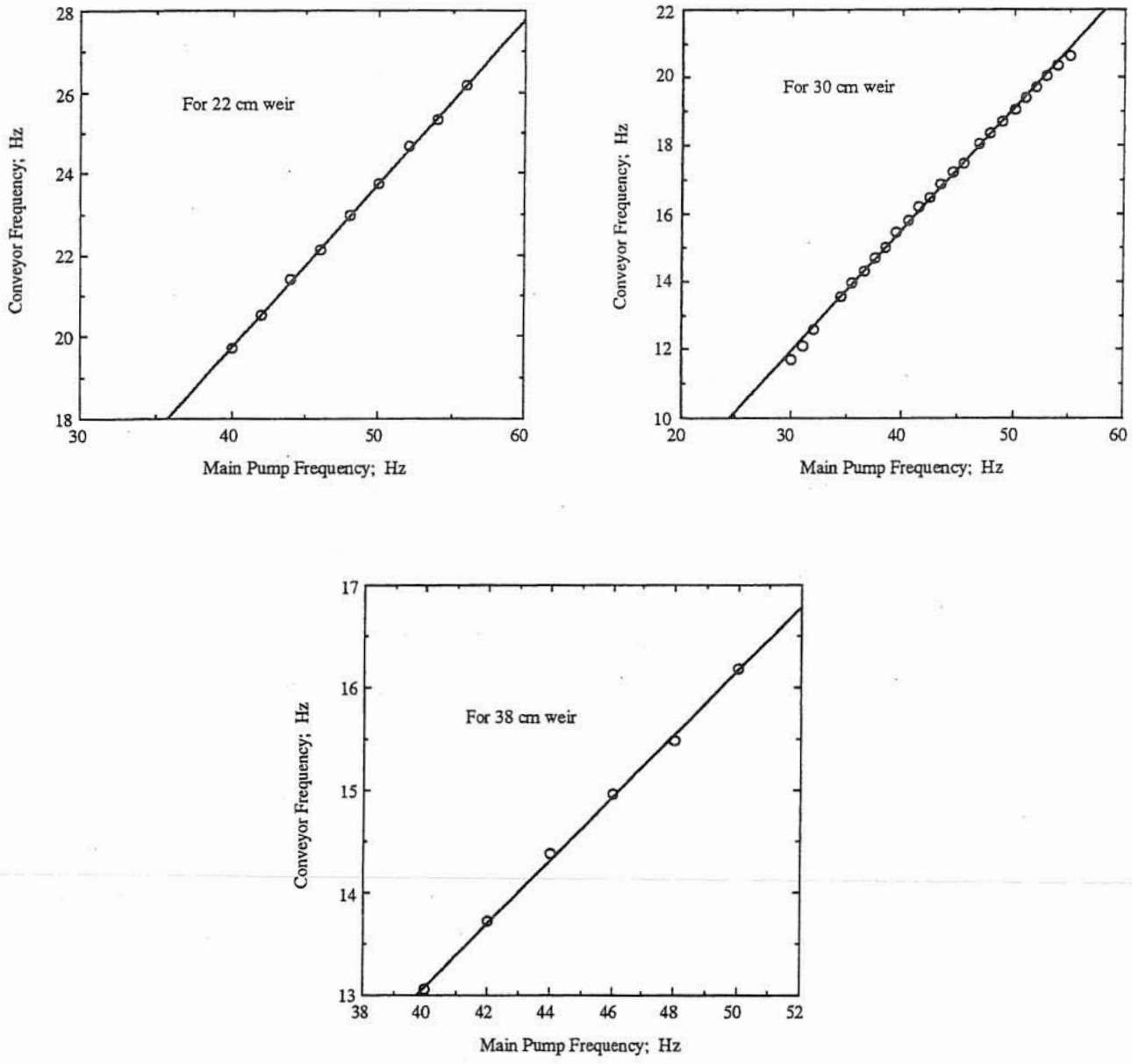

Figure 3.2 Main pump-conveyor calibrations for weir heights 22, 30, 38 cm.

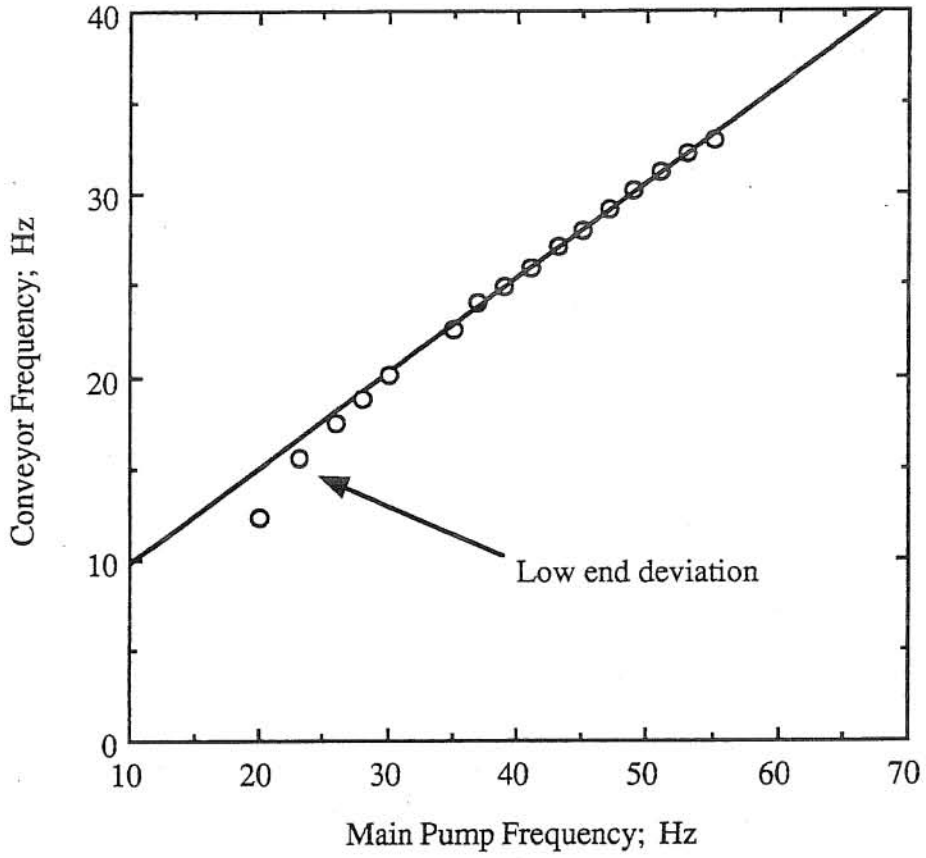

Figure 3.3 Calibration for smallest weir height, 15 cm.

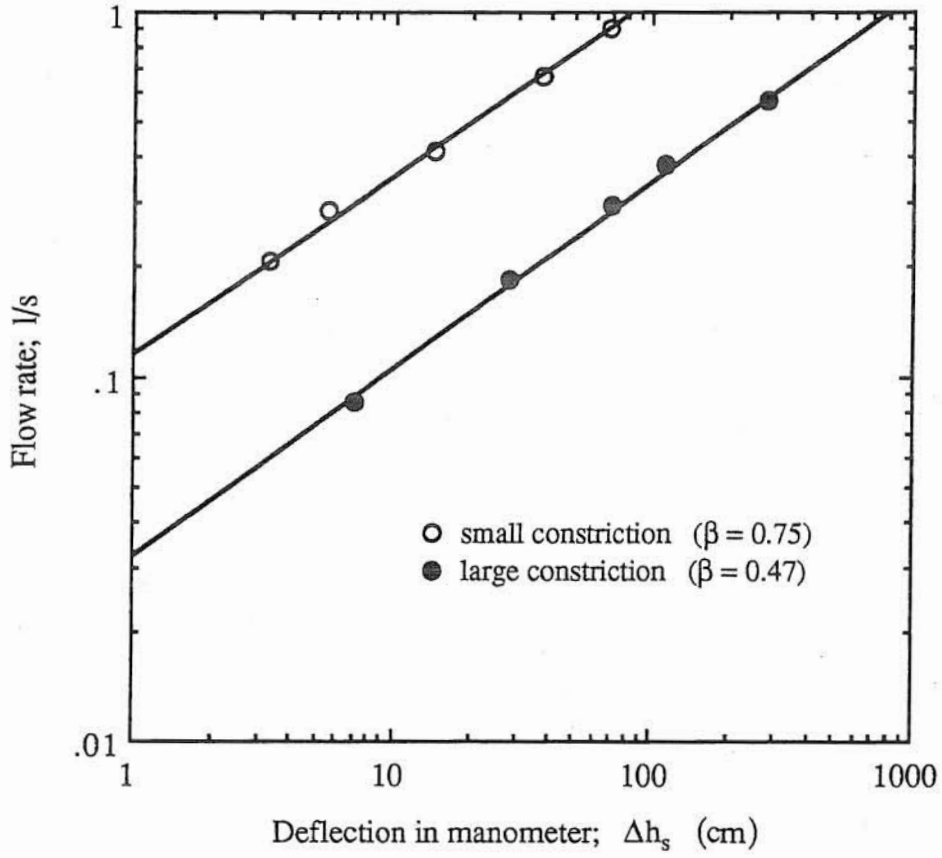

Figure 3.4 Calibrations of both Venturi flow meters used in the experiments

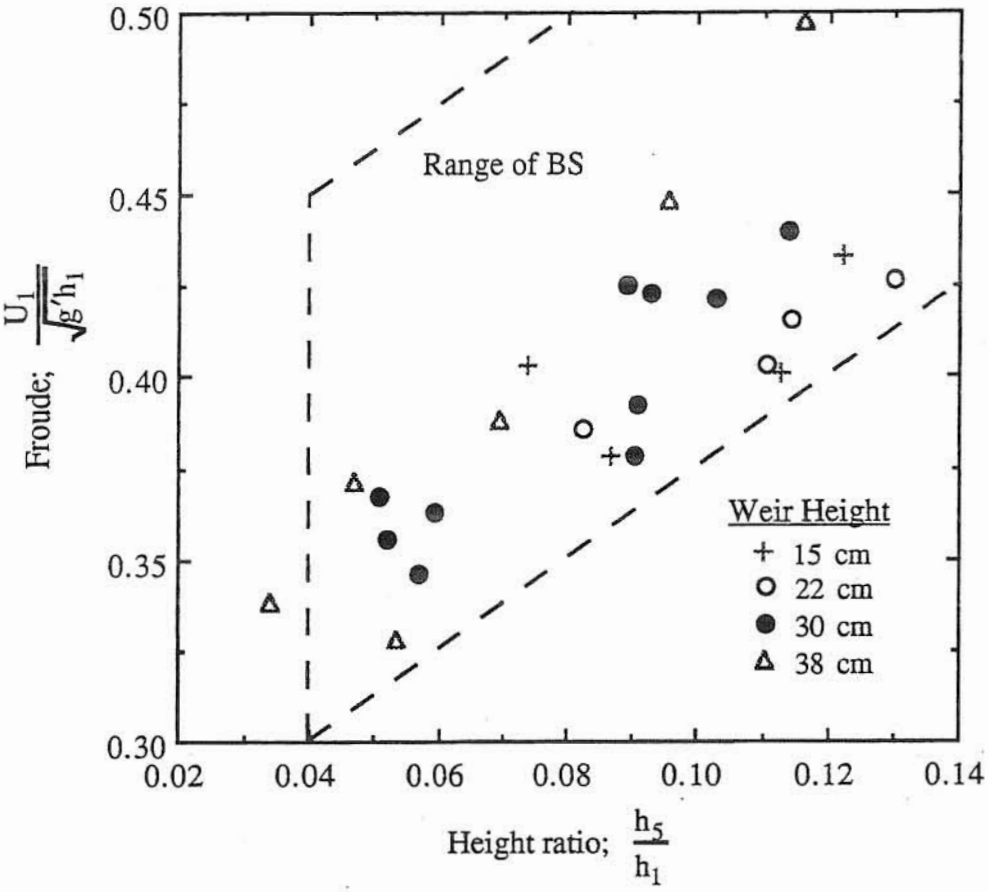

Figure 3.5 Froude number versus height ratio with comparison against the data range of Britter and Simpson (1978)

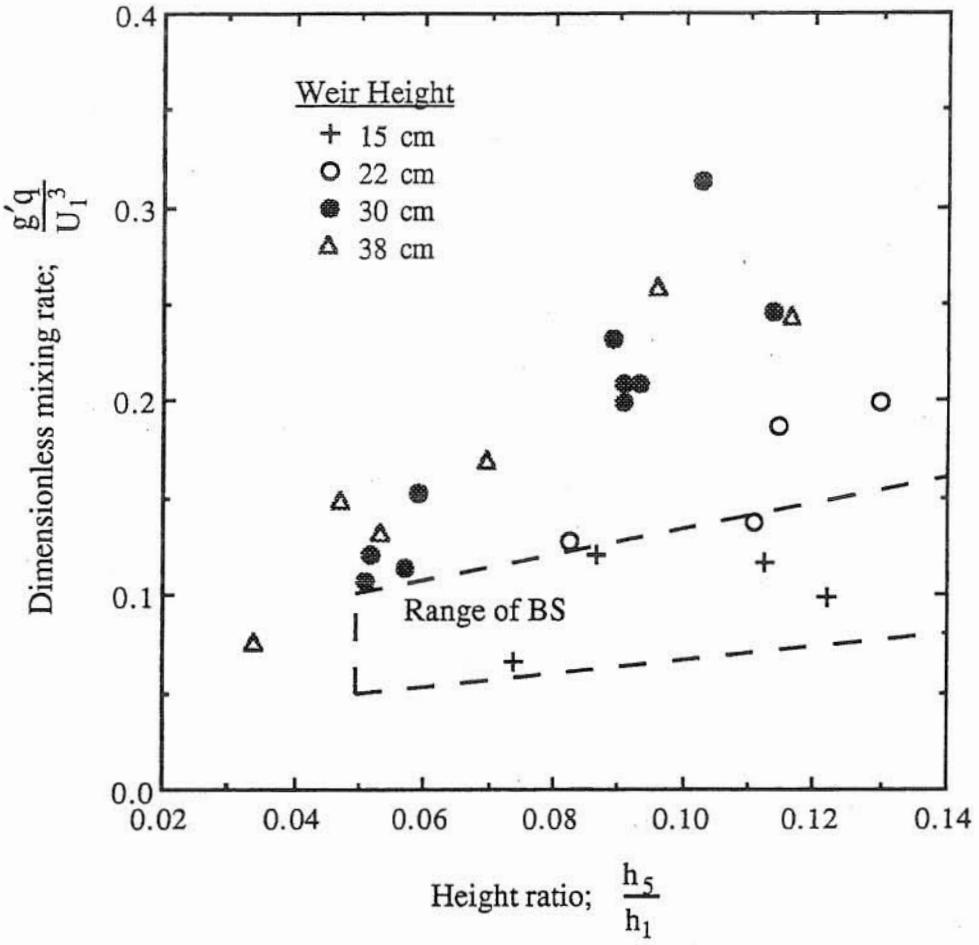

Figure 3.6 Dimensionless mixing rate versus height ratio with comparison to the data range of Britter and Simpson (1978).

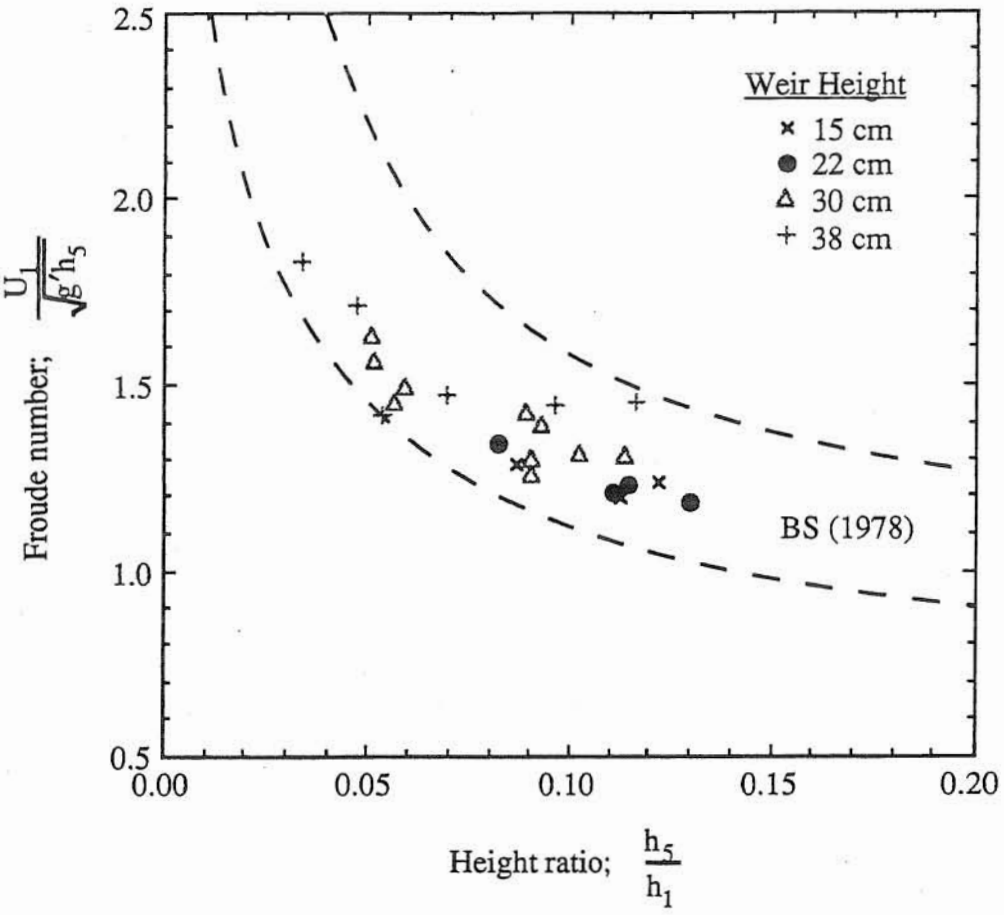

Figure 3.7 Alternative Froude number versus height ratio

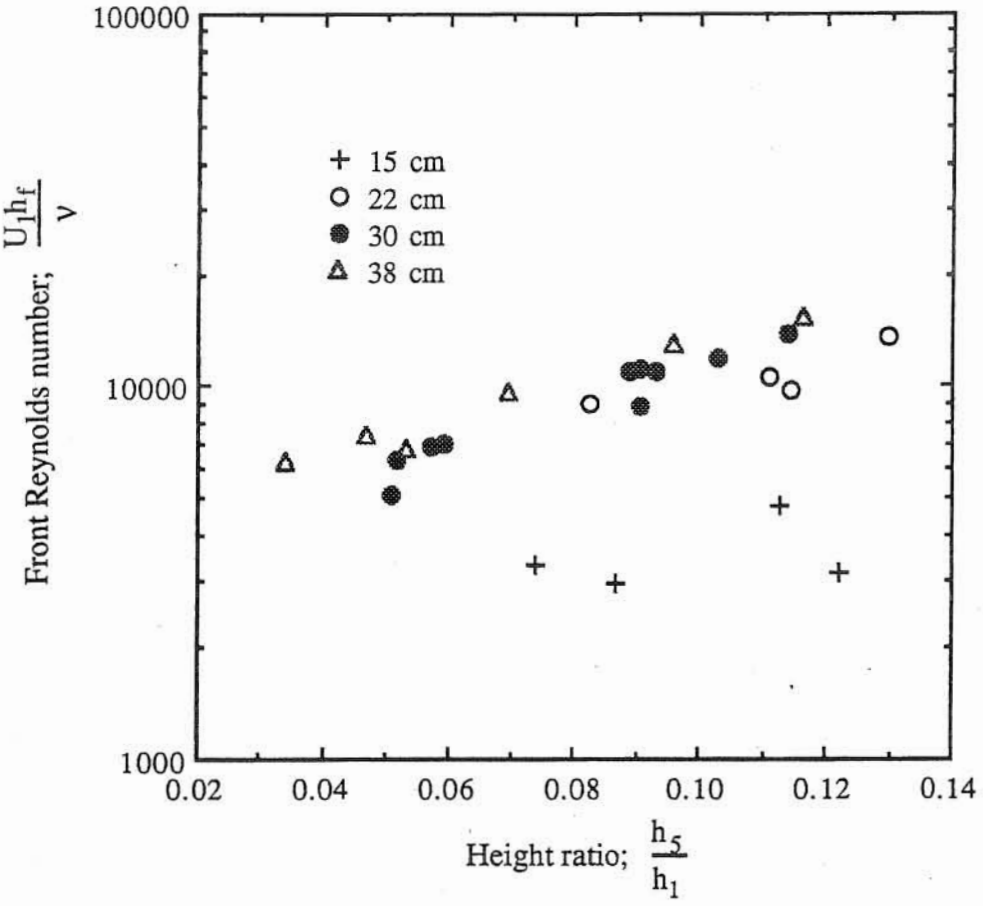

Figure 3.8 Front Reynolds number versus height ratio

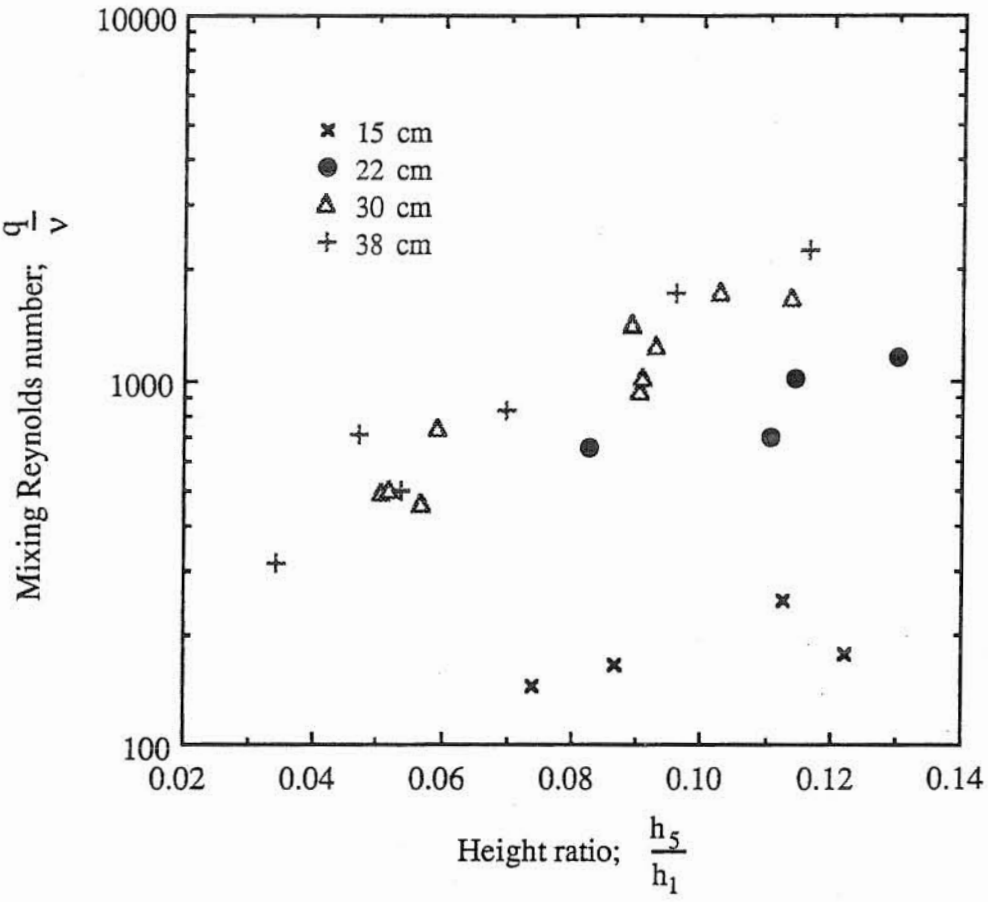

Figure 3.9 Mixing Reynolds number versus height ratio

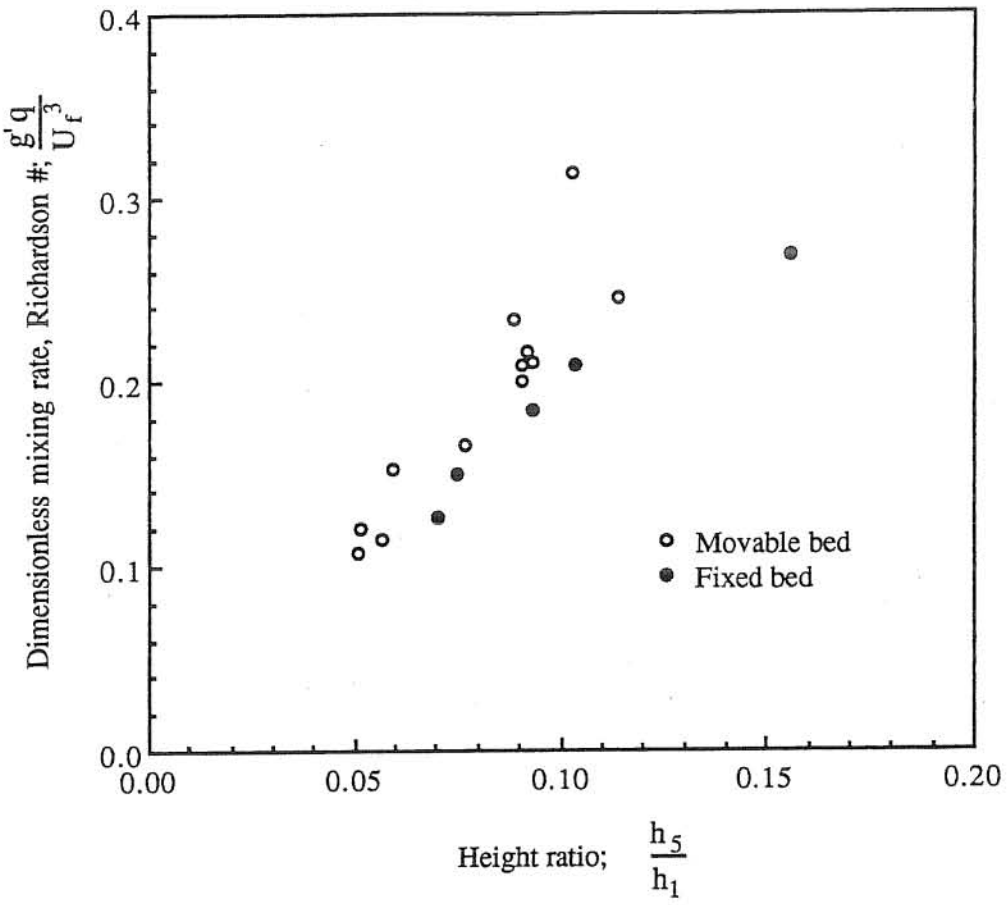

Figure 3.10 Comparison of boundary condition on dimensionless mixing rates for a single weir height (30 cm)

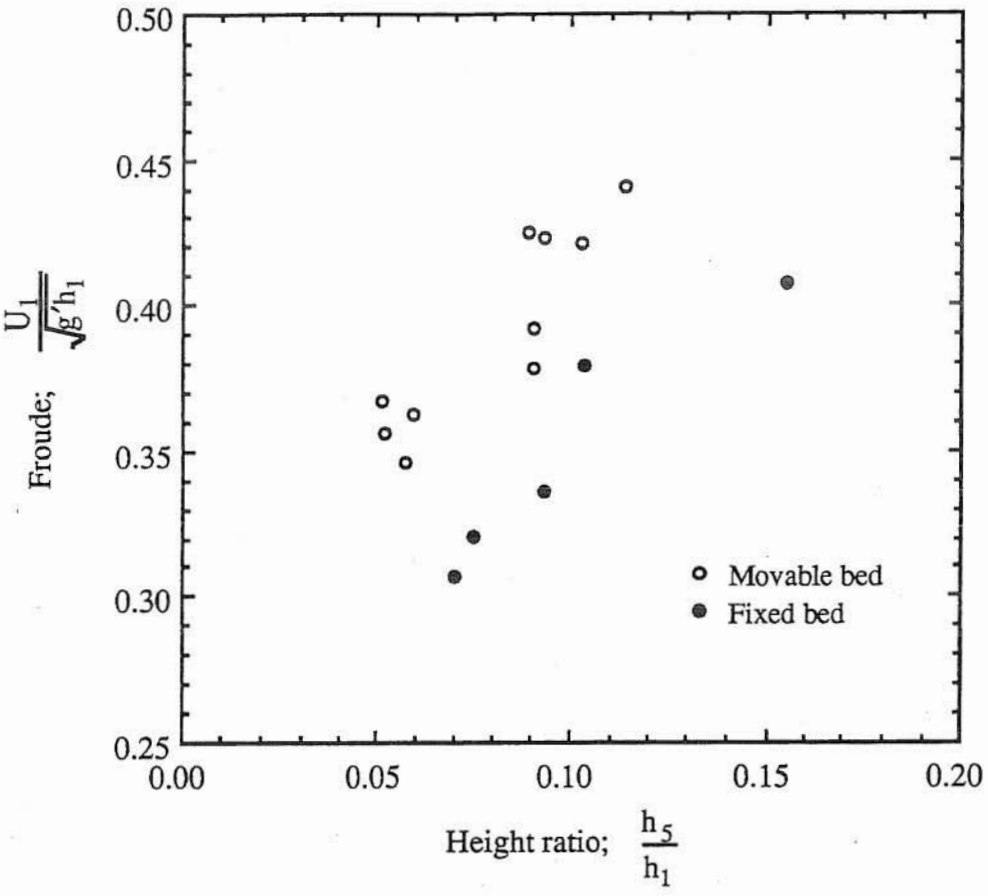

Figure 3.11 Boundary condition comparison of Froude numbers as defined by the flow depth. Data was taken at a single weir height (30 cm).

4. INTERNAL FLOW STRUCTURE EXPERIMENTS

4.1 Generalities

In this course of experiments, an Acoustic Doppler Velocimeter (ADV) was used in conjunction with a Laser-Induced Fluorescence (LIF) technique to produce both a mean velocity and mean concentration profile. The resulting experimental setup was extremely complex due to several different types of equipment being used virtually simultaneously. As a result velocity profiles were taken, along with bulk flow measurements, without concentration measurements. This ensured complete understanding of the ADV probe, which was necessary because this device had not been thoroughly proven in stratified flow environments. LIF measurements were similarly taken with bulk flow measurements, but without ADV (velocity) measurements. Both measurement techniques were rigorously tested in controlled situations (*i.e.*, open-channel flow, constant concentration solutions, *etc.*) to ensure that the devices were working properly.

The goal of this set of experiments was to determine whether the scale effects observed earlier on the overall parameters were influenced by changes in the internal velocity and concentration structure. Many models describing bulk flow behavior depend on some kind of information about the mean profiles (both velocity and concentration). Early observations had indicated that profiles for a range of dimensionless mixing rates were not similar, as should be the case, according to BS and Simpson and Britter (1979). The dimensional analysis presented below takes into account these early observations of the altered structure of the velocity profiles (the concentration profiles appear relatively unaffected) and proposes a modified model which encompasses these scale effects.

The analysis of Benjamin (1968), BS and Simpson and Britter (1979) accounted for only conservation of mass and momentum. However, complete understanding of the front also requires an analysis of the energy characteristics of the flow. Conservation of energy expressions for a density current front have been formulated by Wood and Simpson (1984), assuming energy conservation in the clear fluid, and Denton (1990), assuming energy conservation in the denser fluid. Though Denton (1990) showed both solution methods were physically realistic, he claimed that his approach was superior because his results matched the data of Wood and Simpson (1984) better, for a wider range of height ratios. Both of these models, however, were simplified in several aspects. With respect to geometry, they were based only on heights of characteristic parts of the front (*e.g.*, flow depth, current body height, front height, *etc.*). Also, all of the energy losses were lumped into a single loss coefficient. No strict accounting of turbulent production and dissipation was attempted. And finally, as result of being 'layer-averaged' models, they could not

account for the vertical distribution of density in the overflow (not even with shape factors), an important artifact of the mixing rate.

Experiments were planned to try to extract information about some of the basic energy characteristics of the flow. Also, some flow visualization was planned to qualitatively examine the scale effects seen in the bulk flow behavior and the general form of the turbulent mixing. Prior studies to characterize turbulent mixing (*e.g.*, LIF on mixing layers, Sullivan and List, 1994; LDA on jets, Giger et al, 1992; PIV on wall bounded flows, Adrian, 1991; and PIV and LIF on jets, Simoens and Ayrault, 1994) have been attempted. However, the phenomena in these experiments were simpler, or radically different, than a complex gravity current front. Despite this, the results of these simpler experimental setups lay a useful groundwork for describing the turbulent mixing and energy characteristics of gravity current fronts.

4.2 Dimensional Analysis

The theory of BS appeared to work well for low mixing Reynolds number flows (Re_q < 500), despite being based on inviscid approximations. However, for larger Re_q flows, the assumption of a top-hat profile was poor. In an attempt to correct for the differences in the shape of the profile for large scale flows, an alteration to the theory was made. The modified theory is identical to theory set forth by BS, except that the new assumed profile has a different shape. For completeness the entire theory will be reiterated here. For a more thorough treatment, the reader is referred to Benjamin (1968).

The governing equations are subject to a control volume at the front of the current. This control volume is illustrated in Figure 4.1, by the rectangle ABDEFG, along with slightly altered variable definitions (*e.g.*, h_4, the point of zero velocity, instead of h_5, the visible height of the current behind the front). Equations of motion are developed for incompressible, inviscid and steady-state flow. Other simplifications include the assumption that cross-section AB is far enough upstream such that the front does not affect the velocity (*i.e.*, there is constant uniform flow), the billows at DEFG are fully developed, no free surface effects exist (*i.e.*, rigid lid approximation). The Boussinessq approximation is also invoked. The assumption of inviscid flow and its ramifications are infinitely important and the basis for this study. This assumption is extremely difficult to verify and was most probably violated in nearly all of the steady-state experiments to date (in this study, BS and Simpson and Britter, 1979). Verification can come only from comparison to field data, where Re_q is on the order of 10^6. But as it was shown in Chapter 1, field measurements of mixing rates and internal flow structure (at the resolution needed) are a practical impossibility. A stagnation point is also assumed to exist on the floor, or bed. This point occurs at the foremost point of the front (point O in Figure 4.1) for the moving bed experiments

performed herein. This theory can only model this type of front, as mixing underneath the front due to the no-slip boundary condition (as in Simpson and Britter, 1979) is ignored. At the stagnation point, the pressure is zero. The equations that result are layer averaged, however, they do include information about the vertical structure through the use of several shape factors. The expression for conservation of water is therefore described by

$$U_1 h_1 = U_2 h_2 + (\alpha - \beta) U_2 h_3 \tag{4.2.1}$$

where

$$\alpha U_2 h_3 = \int_0^{h_3} U(h) dh \tag{4.2.2}$$

and the conservation of salt equation is

$$\beta U_2 h_3 = q = \int_0^{h_3} C(h) U(h) dh \tag{4.2.3}$$

where the lower limit of integration is taken at the zero velocity point (*i.e.*, the transition from the underflow to the overflow). The upper limit of integration is taken at the top of the overflow. This convention also applies in the slightly more complicated conservation of momentum equation

$$\frac{1}{2} U_1^2 h_1 + \frac{1}{2} g' h_1^2 + \frac{1}{2} \overline{U_4}^2 h_1 = U_2 h_2 + q\left(\frac{\delta}{\beta} U_2 - \frac{1}{2}\overline{U_4}\right) + \frac{1}{2} g'\left[h_2 + (1-\gamma) h_3\right]^2 + \frac{1}{2} g'\left(2\varepsilon - \gamma^2\right) h_3^2 \tag{4.2.4}$$

where

$$\gamma h_3 = \int_0^{h_3} h C(h) dh \tag{4.2.5}$$

$$\delta U_2^2 h_3 = \int_0^{h_3} U^2(h) dh \tag{4.2.6}$$

and

$$g' = \frac{g(\rho_2 - \rho_1)}{\rho_1} \tag{4.2.7}$$

$$\overline{U}_4 = \frac{q}{h_4} \tag{4.2.8}$$

Concentration is used as a surrogate for density in the theory above, as well as in BS. This substitution, made for experimental data acquisition reasons, implies a linear relationship between density and concentration. Salt followed this assumption well for the range of concentrations in the experiments herein and in those of BS.

All that is required to solve the equations above, (4.2.1) through (4.2.8), is a knowledge of the velocity and salt concentration profiles. The profiles can be expected to be similar for fully turbulent flow. However, similarity can vary with respect to three parameters: dimensionless mixing rate, densimetric Froude number and height ratio. BS assumed that the shape parameters (α, β, γ, δ, ε) were also independent of these three parameters (*i.e.*, there is one velocity and concentration profile shape for all fronts). The analysis below extends the theory so that this assumption can be discarded and includes the differences seen in the fronts herein.

As mentioned above, the possibility of scale effects on the shape parameters was not examined in BS or Simpson and Britter (1979). Previously, the limit of scale was considered to be a Reynolds number greater than 1000. This Reynolds number will from now on be referred to as the front Reynolds number and is defined by

$$Re_f = \frac{U_1 h_f}{\nu} \tag{4.2.9}$$

where h_f is the total height of the front (h_3+h_4, see Fig 4.1) and ν is the kinematic viscosity of the dense fluid, which is assumed to be the same as the overbearing clear fluid. However, as shown in the previous chapter, scale effects can occur beyond this limit. As a result of these scale effects, the velocity profile will most likely be altered. The Reynolds number examined in the analysis of Chapter 3 was one defined by the mixing rate or flow rate of the underflow. The Reynolds number corresponding to this part of the flow could be defined by

$$Re_q = \frac{q}{\nu} \tag{4.2.10}$$

The point at which scale no longer plays a role with respect to this Reynolds number was difficult to ascertain because of the difficulty of producing fronts with a large value of Re_q in the lab. It appeared, however, that the limit of scale lies near the physical limit of the facility (*e.g.*, Re_q = 500-1000). A discussion of the physical limit and other size limitations of the facility is contained in Chapter 3. Discussions of these size limitations and their relevance to the scale limit are also given in Chapter 5.

For the underflow in the model proposed by BS, a constant mean velocity was assumed. The type of profile generated from this approximation will from now on be referred to as a top-hat

profile. Preliminary analysis herein indicated that the velocity in the underflow will not be constant in high Re_q fronts, but will vary linearly with the height above the bed, as shown in Fig 4.1. Therefore, a new profile was sought out to match the behavior seen in the early experiments.

Instead of assuming a top-hat profile (*i.e.*, BS), one was assumed that better fit the preliminary data supplied by the ADV. Fig 4.2 compares this profile to a top-hat profile. The new profile is more comprehensive than the traditional top hat profile. This is because the new profile does not disregard the information contained in the continuity of the velocity profile, it allows, with the same amount of variables, for dependence of the dimensionless mixing rate (and the rest of the dimensionless parameters for that matter) on the shape.

The most important section of the front is the overflow because this section experiences the largest change in velocity. The traditional top hat theory assumed a power law relationship between the dimensionless height and dimensionless velocity in this region. Following BS, the power law is as follows

$$1-\frac{U(h)}{U(h_3)}=\left(1-\frac{h}{h_3}\right)^m \tag{4.2.11}$$

where h is the height above the point of zero velocity (or the point in the Galilean transformed frame where fluid is moving at the propagation rate). From the very beginning, the profiles of this study resembled polynomials rather than a power law. Therefore, trial and error showed that instead of using a power law relationship, where the end was to find the power in the expression above, using a third-order polynomial was more beneficial. The new profile, in the overflow region, is described by

$$1-\frac{U(h)}{U(h_3)}=\xi\left(1-\frac{h}{h_3}\right)^3+\chi\left(1-\frac{h}{h_3}\right)^2+\zeta\left(1-\frac{h}{h_3}\right)+\theta \tag{4.2.12}$$

where U and h are defined as in Figs 4.1 and 4.2 and ξ, χ, ζ, θ are coefficients to be determined. The constant (θ) and first order (ζ) terms of the polynomial can be shown to be zero by continuity of U(h) and its derivative evaluated at h_3 (necessary from the constant, uniform velocity profile in the overbearing flow and basic fluid mechanics). The relationship between ξ and χ, the resulting empirical parameters of this profile, can be solved for by noting that at h = 0, U(h = 0) = 0. The relationship that results is simply $\xi+\chi = 1$. The results presented here indicate $-1.5 < \xi < -0.4$, and therefore $2.5 > \chi > 1.4$. These values were backcalculated from the bulk flow parameters, using

(4.2.13) below. In other words, q, h_4, h_3, U_2 were found from experimental data (as in Appendix 3) and used (from (4.2.13) below) to find ξ.

As mentioned previously, the final portion of the front, the underflow, seemed most different from what BS found. The traditional, top-hat approximation assumed a constant value for the velocity in the underflow. However, the measurements in this study indicated a linear increase of velocity to the bed. Although this may have been accentuated by the effects of the ADV, as will be mentioned later, the trend of this behavior was unmistakable. A linear velocity profile in the underflow region was just as easy to manipulate in (4.2.4) as the constant profile presented in BS. In addition, the derivative of the dimensionless profile of (4.2.12) can be related to the mixing rate, q, without the addition of another velocity (*e.g.*, U_4). That relation is as follows

$$\left.\frac{d\left(1-\frac{U(h)}{U(h_3)}\right)}{dh}\right|_{h=0\,(U=0)} = 3\xi + 2\chi = \frac{2qh_3}{h_4^{\,2}U_2} \qquad (4.2.13)$$

where the variables are defined in Fig 4.1. The substitution of (4.2.13) into the mass and momentum balances of Benjamin ((4.2.1), (4.2.3), (4.2.4), here) relates the shape of the profile to the mixing rate, making it possible to describe the front more completely without adding any parameters describing the internal velocity structure of the front. The only empirical information that is now needed is for concentration and the final expression can be shown generally as

$$\Phi\left(\frac{U_1^{\,2}}{g'h_4}, \frac{h_4}{h_1}, \frac{g'q}{U_1^{\,3}}\right) = 0 \qquad (4.2.14)$$

which is identical to (3.2.1), if viscous effects are ignored, found from basic dimensional analysis.

The precise function Φ can be found by solving (4.2.1) and (4.2.3) simultaneously and by noting that $h_1 = h_2+h_3+h_4$ from geometry. This allows for U_2, h_2, h_3 to be found in terms of the remaining variables. Doing this mathematically results in

$$U_2 = \frac{U_1h_1\beta + q(\beta-\alpha) + q}{\beta(h_1-h_4)} \qquad (4.2.15)$$

$$h_2 = \frac{(h_1 - h_4)(U_1 h_1 + q(\beta - \alpha))}{U_1 h_1 + q(\beta - \alpha + 1)} \tag{4.2.16}$$

$$h_3 = \frac{q(h_1 - h_4)}{U_1 h_1 + q(\beta - \alpha + 1)} \tag{4.2.17}$$

By substituting (4.2.15), (4.2.16) and (4.2.17) into (4.2.4), an equation in terms of only U_1, g', q, h_1, h_4 results. Multiplying each side of the resulting equation by $2/(g'h_1h_4)$ and manipulating it to form a function of the three principal dimensionless numbers shown in (4.2.14) above gives the final model equation. This derivation is exactly the same as what BS did to find their final model equation (Equation 2.9a, BS), though it was not elaborated upon there. The final equation presented here differs slightly due to the alteration of the momentum distribution in the underflow. The fourth term in (4.2.18a), however, is the only one that is different in the final mathematical expression. Instead of $\mu^2 f^3(1-\phi)$, as found below, Equation 2.9a of BS has the fourth term reading $\mu^2 f^3(2-\phi)$. It was found that this alteration was insignificant (< 1%) for small values of dimensionless mixing rate and densimetric Froude number. The difference was larger for large values of the dimensionless mixing ($\mu > 0.25$), but was still no larger than 10% for any physically possible set of parameters. The new model equation is thus described by

$$\begin{aligned} &f - 2fx(1-\psi)^2 - 2\delta\beta^{-1}\mu f^2\phi x(1+\psi) + \mu^2 f^3(1-\phi) + \\ &\left\{1 + \frac{\gamma B}{1+B\phi}(1-\phi)\right\}\left\{2 - \phi - \frac{\gamma B\phi}{1+B\phi}(1-\phi)\right\} + \frac{B^2\phi}{x^2}\left(\gamma^2 - 2\varepsilon\right) = 0 \end{aligned} \tag{4.2.18a}$$

where

$$\phi = \frac{h_4}{h_1} \quad f = \frac{U_1^2}{g' h_4} \quad \mu = \frac{qg'}{U_1^3} \quad \xi = 2\left\{\left[\frac{\mu f \beta^{1/2}(1-\phi)}{\beta(1+\mu f\phi) + \mu f\phi(1-\alpha)}\right]^2 - 1\right\} \quad \alpha = \frac{8+\xi}{12}$$

$$\gamma = \frac{1}{n+1} \quad \beta = \frac{2n+8+\xi(n+1)}{(n+4)(n+3)(n+1)} \quad \gamma = \frac{1}{n+1} \quad \delta = \frac{2\xi^2 + 21\xi + 112}{210} \quad \varepsilon = \frac{1}{n+2}$$

$$\psi = \left(1 - \frac{\alpha}{\beta}\right)\mu f\phi \quad B = \frac{\mu f}{\beta(1+\psi)} \quad x = \frac{1+B\phi}{1-\phi} \tag{4.2.18b}$$

The solution of (4.2.18a) required two iterative loops. The inner loop solved for ξ (for a given combination of μ, f, ϕ), while the outer loop solved the main equation. Both iterations converged rapidly for physically realistic parameter combinations. Equation (4.2.18a) was relatively insensitive to changes in ξ for reasonable parameter values. The limits of the range of

these parameters (*e.g.*, high dimensionless mixing, high Froude numbers), however, presented a significant effect on the profile through the shape factor ξ. The model equation, however, could also be solved for constant values of ξ. The physical meaning and the results of this will be discussed below.

Concentration profiles seemed to exhibit power law behavior, even for the larger scale flows presented here. The parameter n, in (4.2.18b) above, corresponds to the exponent in the power law expression in the concentration profile. Mathematically, this is described by

$$\frac{C(h)}{C(0)} = \left(1 - \frac{h}{h_3}\right)^n \qquad (4.2.19)$$

The same form was obtained by BS. Furthermore, the value of n = 4 (the value found by BS) is similar to the preliminary results for the large scale flows. Therefore, the power law expression (with the value of n = 4) was retained in the modified model herein. A further discussion of concentration profile characteristics is given in the remaining sections of this chapter and in Chapter 6.

4.3 Experimental Plan

The plan of these experiments was to capture the mechanics and structure of the saline current fronts. The most interesting and well studied portion of the front was the region in which the Kelvin-Helmholtz billows appeared. The ADV probe in combination with an LIF technique allowed for the complete study of current profiles. These profiles can be used to describe and explain mixing processes which regulate the front on a bulk, or global, scale.

Velocity profiles were obtained with an Acoustic Doppler Velocimeter (ADV). The first several experiments where the ADV was used attempted to validate the assumption of constant, uniform flow at the end of the belt. The resulting cross-sectional velocity field exhibited two secondary cells, one strong and one weak. These secondary currents were thought to be a result of the pump and varied with distance down the conveyor (*i.e.*, they weaken and oscillate with distance in a helical pattern). An illustration of the complex nature of the secondary currents is illustrated in Fig 4.3 which is an areal plot of approximately 60% of the cross-section (primarily in the middle of the channel). This cross-section was taken 50 cm downstream from the constriction. Other cross sections were taken at various other locations in the streamwise direction to ascertain the structure of the flow along the streamwise direction of the conveyor belt. Fig 4.4 illustrates the weakening of the primary secondary cell and decay of overall (cross-sectionally averaged)

turbulent intensity with distance downstream of the constriction. Concerns over turbulence effects on the mixing characteristics of the fronts as scale increased prompted a study of the intensity of the turbulence of the overbearing flow. The result of the analysis is summarized in Fig 4.5. As can be seen fairly well in this graph, turbulent intensities actually decreased as the scale (or weir height) of the facility was increased. This was most likely a result of the fixed and limited supply of turbulent energy from the pump being spread over a larger volume (as was the case in a larger scale setup).

Concentration profiles were obtained by Laser-Induced Fluorescence (LIF). Although the experimental technique was not established prior to the completion of the first experiments, several papers, such as Walker (1987), were reviewed for the particulars beforehand. The LIF technique allowed for large amounts of information (both spatial and temporal) to be gathered from just one experiment. However, many difficulties had to be overcome, as described in the following section.

All of the profiles (regardless of technique, ADV or LIF) were taken at the point in which the billows seemed to be fully developed. The streamwise position of the profile is illustrated with respect to the front in Fig 4.6. The same streamwise position was used in the data acquisition efforts of BS and Simpson and Britter (1979) and is required by the analysis of the previous section.

In addition to finding information about the mean structure of the front, information about the spatial and turbulent energy characteristics of the front was also sought out. One of the most fundamental quantities calculated was the turbulent kinetic energy (TKE). Though it was hoped that viscous dissipation could be measured, from the beginning, it was found that dissipation rates were impossible to resolve from the poorly sampled (25 Hz or 30 Hz) record. Profiles of turbulent kinetic energy (TKE), however, along with profiles of turbulent intensity in both the streamwise and vertical directions, were produced. These plots yielded some knowledge of the internal structure which regulates the fronts on a larger scale. Autocorrelations were also produced. As was mentioned before, the ADV has the capability to only sample at 25 Hz, well below what is necessary to capture all of the frequencies in a flow of this nature. However, the primary mixing process at the front, the Kelvin-Helmholtz billows, operate at much lower frequency than the higher frequencies of viscous dissipation. Therefore, these phenomena could be studied with the ADV and a standard (30 Hz) video camera.

Autocorrelations were generated for the clear water flow without a front to get an idea of the integral time scale of the overbearing flow and whether the ADV was working properly. An example of one of these trials is Fig 4.7, taken 22.6 cm above the bed. After these preliminary tests, the data collected in the fronts was analyzed. The length of the data record was an unavoidable problem and the results revealed some inconsistencies as a result. Later, power

spectra of the velocity data were also made. Sampling rate problems (*i.e.*, aliasing) were a major difficulty here and only small portion of the frequency domain could be realized.

Areal information was also needed to grasp the overall nature of the front. Because the steady-state front varies dramatically in the two dimensions examined in the study, a plane of concentrations and, if possible, velocities would be very beneficial. Therefore, LIF experiments were designed in such a way to obtain a fairly large areal view of the portion of the front studied. The area included the vertical line where the profiles were typically taken, along with a significant portion of the front not analyzed previously . However, space constraints limited the amount of the front that could be sampled. The goal of these experiments was to find qualitative information about how saline water is mixed out of the front. This part of the study was conducted simultaneously with the mean internal structure LIF work of the previous chapter. In other words, the images used to produce the areal pictures of concentration were the same images that produced the time-averaged, dimensionless concentration profiles. The acquisition procedures of the concentration profiles are described in detail below.

4.4 Detailed Description of Measuring Devices and Techniques

ACOUSTIC DOPPLER VELOCIMETER (ADV)

The ADV probe was used first to understand the dynamics and structure of the velocities inside the front. Before these experiments, looking nonintrusively at the mean and turbulent structure of a steady-state saline current had never been accomplished. From approximately 5 cm away, the ADV can record a time series of three components of flow. Fig 4.8 illustrates the logistics of data acquisition. The ADV module required a DOS compatible computer and a substantial software acquisition package. The software package, supplied by Son-Tek (the manufacturer of the probe), calculated a three dimensional velocity vector from Doppler shifts of ultrasonic waves that reflect off small particles (acoustically speaking) suspended in the flow. Implicitly assumed in this analysis was that the particles move with the flow. The particles utilized were naturally occurring in the water tanks. Although the origin of the particles was unknown, they were most likely microbubbles produced from the different pumps in the apparatus (personal communication, Atle Lohrmann). Preliminary flow visualization indicated that the particles were probably on the order of 10 μm, therefore they were adequate representations of fluid particles.

Because the ADV used sound waves to measure Doppler shifts, factors affecting the speed of sound were inputs to the data acquisition routine. For instance, temperature and salinity were input for each data set taken. The temperature was measured at the beginning of the experiment with a digital thermometer with an accuracy of a tenth of a degree Celsius. Salinity was assumed to be zero in the overbearing flow and equal to the salinity of the saline tank in the underflow. In

the overflow, one-half of the salinity of the underflow was assumed. Concern over the effect of the speed of sound due to salinity prompted an experiment where various, widely-varying values of salinity were input into the acquisition software. Results showed that the impact of salinity on the output velocities was of little importance. As can be seen in Table 4.1, the differences in mean velocity and turbulent values were small for large, unrealistic changes in salinity. Table 4.1 represents point data from a preliminary run inside a billow in a moderately concentrated front (with respect to the rest of the experiments herein). This setup was thought to produce the most error in the resulting mean and turbulence values. The salinity of the underflow in this experiment was approximately 14 ppt and the sampling height was 6 cm above the bed. The distance to the bed output also varied little over the wide range of salinities input. One of the manufacturers of the probe (personal communication, Atle Lohrmann) validated this conclusion by insisting that from the physical principles of the probe the percentage errors in the speed of sound will be only magnified twice. Because the speed of sound only changed by 1-2% over the entire salinity range of the experiments studied here (and the trial of Table 4.1), errors in velocity and distance to the bed due to incorrect assumptions in salinity should be negligible (or at worst, a few percent as in Table 4.1). This is a great advantage of the ADV in saline, stratified flow experiments, as compared to most other methods (*e.g.*, hot-film, LDV, *etc.*). The problems with these methods will be explained further in the following paragraph and in Chapter 6.

Most of the common velocity measurement techniques (*e.g.*, hot-film, LDV) cannot be implemented in these experiments because of critical violations of their operating standards. The LDV must be used in a fairly constant index of refraction continuum (non-stratified flows), in order to avoid refraction and reflection problems. Hot-films have extreme difficulty in dealing with flow reversal (the most important point in the flows here). They also do not deal well with high turbulent intensity environments. This is despite the fact that BS and Simpson and Britter (1979) found velocity profiles from a hot-film probe. How they detected the flow reversal and dealt with other problems of using a hot-film in this type of flow is still unknown. Hypotheses are formulated in Chapter 6 as to the ramifications of using a rather inappropriate measuring device, as they did, in the front region.

Even using the ADV, several limitations existed on data collection. The first, and probably most significant, was that the probe was unable to accurately record velocities at a sampling rate faster than 25 Hz. Surprisingly, sampling faster than this, up to 100 Hz, was found later (after all of the experiments were completed) to be possible with minor alterations to the startup routine. The manufacturer, however, felt that an unacceptable amount of acoustic noise existed in a signal above 25 Hz and did not recommend sampling faster than that (personal communication, Atle Lohrmann). This operating sampling frequency was too slow to capture all of the frequencies in the flow. Viscous dissipation occurred in the channel, according to the Kolmogorov frequency

scale, on the order of 100 Hz. Therefore, obtaining a complete (all relevant scales) power spectrum of turbulent motions was impossible due to aliasing problems. However, the overall turbulent energy was resolved fairly well (assuming that acoustic noise compared to the turbulent fluctuations was small for a sampling frequency of 25 Hz) because of the acquisition of all three velocity components and the fact that most of the energy occurred in frequencies smaller than 10 Hz (*i.e.*, the billows).

Another drawback of the probe was that it integrated velocities over a relatively large volume rather taking a true 'point' measurement. As a result, measurements extremely close to the bed were not possible. The manufacturer recommended in Kraus et al (1994) that no measurements be taken below 5 mm because the typical volume of integration is an ellipsoid has a major axis of 9 mm and a minor radius of 4.5 mm, and therefore part of the sampling volume. Again, Fig 4.8 describes this layout. After completing all of the experiments, it was found that the volume of integration could be reduced. However, like with the sampling rate, acoustic noise becomes important (personal communication, Atle Lohrmann) for smaller sampling volumes than the 'default size' (the size used in the experiments herein). Another problem with the finite averaging volume, besides the inability to get close to the bed, was the possibility of smearing the velocity profile. This smearing, however, occurred on a much smaller scale than the distance between the sampling points. In other words, even if individual realizations near the underflow-overflow interface were biased because of the irregular gradient in velocity there, the overall shape should remain intact because of the quantity of well-spaced points used in the profile calculations. Also, because the probe was more likely to 'track' particles (because of the physics of the sound reception) moving closer to the center of the sampling volume, velocities were biased towards the theoretical point of measurement (*i.e.*, the center of the measuring volume).

Velocity data, as mentioned before, was acquired at rate of 25 Hz. Preliminary analysis, performed at the same time as the test for salinity sensitivity, demonstrated that sampling at 25 Hz required at least 45 sec of data to establish a representative mean and standard deviation (rms value) at that point. The integral time scale of flow varied from experiment to experiment, but typically ranged between 1-3 sec. This was confirmed later by calculation of autocorrelations (therefore, theoretically establishing an integral time scale) in the billow region. Fig 4.9 demonstrates the results of the preliminary analysis.

Generally ten to fifteen points made up a profile. As stated above, time constraints due to pollution of the overbearing flow made a complete, densely-sampled profile with long sampling times impossible regardless of the equipment used. The points were weighted spatially towards the bed because most of the overbearing flow, outside of its basic characteristics, was unimportant for the analysis. Generally eight to ten points were taken inside the region of the front, again, with

further weighting near the interface of the underflow where the velocity gradient was highest and most critical.

The effects of boundary conditions were quite substantial on the ability to obtain consistent, repeatable profiles of both velocity (with the ADV) and concentration (with LIF, explained below). A comparison of bulk flow results for the fixed and moving boundary conditions is Fig 3.10. From this graph, little differences existed in the dimensionless parameters. The reasons for this are speculated upon in Chapter 5. The difference in stability and steadiness of the two types of fronts, however, was radically different. When the fronts were stopped on top of the belt (as in the fixed bed experiments) the front moved, even after it was 'arrested', back and forth in a wave-like pattern. This motion moved the front as much as 10 cm in a minute or two and then back again. Such a motion also occurred in the moving bed experiments. However, the overall position of the front in the streamwise direction in those experiments did not change enough to bother the measurements (*e.g.*, enough to perturb the mean concentration and velocity when sampled over a 45 sec record). As will be shown below in the results, the oscillations of the front position also made assessing consistent velocity profiles difficult. Due to the combination of insignificance and complexity of altering the boundary condition, fixed bed experiments were disqualified from the internal flow analysis (in both the case of the ADV and LIF), though a plot is included (Fig 4.12) to illustrate the anomalies described above. In addition, the theory of Simpson and Britter (1979), which included the effects of the mixing underneath the front in the fixed bed case, was slightly different than the theory derived above. A treatment of the oscillations was also made from the areal LIF experiments and will be briefly discussed below.

The ADV turbulent profiles that were taken came from the same data set as the mean profile results. The mean results were only one part of a system of statistical analyses. The time series that was recorded was also used to find a standard deviation for each of three velocity components. With this, it was possible to find the turbulent kinetic energy per unit mass. This can be described by the following equation

$$TKE = \frac{1}{2}\left(u'^2 + v'^2 + w'^2\right) \qquad (4.4.1)$$

where u', v' and w' are the root mean square of the fluctuations of each of the velocity components. Power spectra and autocorrelations of the time series of the velocity signals were also produced. Aliasing problems again plagued these attempts. The short record length prevented good realization of the peak in energy due to the billows. Remember, contamination of the overbearing, clear flow prevented accurate experiments lasting longer than 10-15 minutes. The inability to use multiple data sets for each point also compounded the other sampling problems.

Future experiments will concentrate more in the billow region (for reasons explained below in Chapters 5 and 6), rather than attempt to obtain an entire velocity profile. This will allow for multiple, long record lengths to be obtained for a single point in the flow.

LASER INDUCED FLUORESCENCE TECHNIQUE

The overall setup for the Laser-Induced Fluorescence (LIF) experiments is illustrated in Fig 4.10. The fluorescent front was created by a adding certain amount of disodium fluorescein (MW 376.3) to the mixing tank along with the salt required for the experiment. The amount of fluorescein used was less than 10 mg. An ILT Model 5500A air-cooled Argon Ion laser attached through a Dantec fiber-optic cord to a cylindrical lens illuminated the fluorescein-laden front. The power of the laser was 300 mW with a frequency range of 457-514 nm. A Yashica Model KD-H170 video camera recorder sampled the front at a rate of 30 Hz. The camcorder had the option of viewing frame-by-frame. In conjunction with a Perceptics frame-grabber, the camcorder was used to transfer a 480 x 640 pixel field to the computer (a Macintosh IIci). This output matrix was displayed by using Image 4.4.1, a public domain software package available from the National Institute of Health (NIH).

The LIF technique applied here was based on the work of Walker (1987), which summarized the current state of knowledge on LIF applications to stratified flow visualization. The first parameter determined was the amount of fluorescein needed to add to the mixing tank to produce consistent results. In order to find this value an analysis was performed on the laser sheet to ensure that attenuation of light intensity did not occur. To this end, Walker (1987) presented the equation

$$I_f(b) = I_0 A \varphi E L c(b) \exp\left(-E \int_0^b c\, dz \right) \qquad (4.4.2)$$

where I_f is the fluorescence intensity at a point b, I_0 is a reference intensity (*e.g.*, the intensity of laser at the lens), L is the length along the laser sheet for each sampling volume (pixel), φ is the quantum yield of fluorescence, A is the fraction of available light collected (approximately equal to the sampling frequency divided by 16), E is the extinction coefficient and c is the concentration of dye. The most crucial part of this equation is the exponential term. Note that for values of $\log(Ebc) < -1$, the concentration at a point is nearly linearly related to the intensity at that point (b). In physical terms, the exponential component of (4.4.2) describes the loss of energy due to photons absorbed into individual fluorescein molecules. Therefore if this effect is small, (4.4.2) becomes

$$I_f(b) = I_0 A \varphi E L c(b) \qquad (4.4.3)$$

which indicates that if only relative concentrations are required then the ratio (I_f/I_0) is the only necessary variable, assuming I_0 is constant. Therefore, using (4.4.3) makes the determination of relative concentration profiles and analysis of variations of concentration within the billow region, for this range of log(Ebc) relatively simple.

The threshold of the linear portion of the curve, therefore, depended on the extinction coefficient (E), which has been shown to be dependent on experimental conditions (pH, Walker, 1987; temperature, Guilbault, 1973), the total path length of the laser light exposed to the fluorescein (b) and the concentration of the fluorescein (c). The temperature effects were negligible on E for small (1-2 degrees C) changes in temperature, however pH effects were substantial for pH < 8.0. Therefore, the tap water used (pH = 8.7) was not allowed to stand before running the experiment. Initial calibrations confirmed a value of E (approximately 80000 $Lmol^{-1}cm^{-1}$), close to that for the pure base case of Walker (1987). The experimental setup constrained the value of b to be about 10-15 cm (the maximum height of the front). Therefore, for log(Ebc) to be less than -1, the concentration (c) needed to be less than 5×10^{-8} mol/L. For safety, the concentration of fluorescein in the mixing tank was kept at 1×10^{-8} mol/L (typically 5-10 mg for the entire mixing tank).

After determining the correct amount of fluorescein to add and after beginning the experiment, the camcorder recorded the illuminated front. The camcorder sampled a single field sixty times a second (60 Hz). However, a complete picture required two fields, making the actual sampling rate 30 Hz, typical of most video equipment. The camcorder was mounted on a tripod approximately 2-3 cm from the side of the channel and was typically tilted slightly (< 5 degrees) in order to capture the bed in the viewfinder. This angle of inclination was extremely important in the final quality of the image because if the angle was not chosen correctly reflection and refraction of reflected light (from the bed) or fluoresced (from the front) light between the image plane and the camera can irreversibly affect image quality. Difficulties associated with refraction and reflection of light are commonly dealt with by index matching (matching the indices of refraction of both the dense and clear fluid). However, due to the large scale of the experiment, this would be an extremely difficult and costly measure. In defense of the procedure used herein, the differences in index of refraction of clean and low salinity water (20-30 ppt) were not enough to cause significant problems. The vigorous mixing of high mixing rate fronts also minimized refraction effects.

Image processing was an important step in the technique as well. Much of the knowledge of the process can be found in Goldstein (1983). Also, personal communications with Professor

Ronald Adrian, a noted expert in the field, and Dr. Yarko Niño aided in complete understanding. The image began as a matrix of voltages, where each voltage was described as a pixel. These pixel voltages were converted via a look-up table (LUT) to 8-bit strings. Several LUTs could have been used with Image 4.4.1, but the clipped-linear LUT, where the maximum and minimum were set by the camcorder gain, was most useful for the application at hand. Errors due saturation at both ends of the intensity spectrum (present due to limitations of the photo-electronics) were expected and necessarily assumed to be small. A spatial filter (the default 3 x 3 kernel in Image 4.4.1) was applied to the images after being grabbed. This smoothing eliminated the unnatural (not apparent when the analog signal was viewed) graininess generated in the digitization process without losing information about the character of the front. In addition, natural scatters were present in the flow, predominantly in the clear water, which tended to create unnatural spikes in the intensity matrix. Simoens and Ayrault (1994) have shown, with the aid of a high-pass filter, that a fluoresced image can be optimized and separated from particle spikes. These spikes, however, were distinguishable from the front on the camera and were removed manually, without a high pass filter, with the use of the 'eraser' function inside Image 4.4.1. Due to the extremely low concentrations (relative to the size of the field of view used by Simoens and Ayrault, 1994, which was ten times smaller than that used here) involved, it was felt that an analog filter would eliminate too much information about the front. In other words, too much fluoresced light intensity would be lost if a filter was to be used. The results of the image processing consist of matrix of light intensities varying from 255 (extremely bright, white) to 0 (dark, black) for each frame processed.

After the processing, the matrix of intensities was ready for analysis. The algorithm of basic processing described above was identical for all of the LIF experiments, including the turbulent and areal measurements described below. When obtaining a mean concentration profile, a column of the resulting matrix was recorded. The column used in the profile analysis was the centerline of the laser, insuring no effects of attenuation due to the lateral spreading of the laser beam. Sampling at 1 Hz for 45 seconds yielded consistent results (identical to the required velocity sampling time). Next, a column of the intensity matrix was extracted and saved to a text file. This column of numbers was then transferred to an Apollo workstation and processed with the help of a FORTRAN code. The code found the statistical properties of each pixel above the bed. The bed was found by scanning the entire column and finding the most intense pixel. It was found that the immobile grit affixed to the Plexiglas bed reflected a large portion of the laser light. Reflected bed intensity typically exceeded the intensity produced by the fluorescein tracer by a factor of at least two. This procedure was needed for two reasons. First, the slightly angled camera tended to make strict definition (by the vertical position in the column) of the bed difficult. Also, the frame grabber experienced occasional difficulty in holding the sync of the incoming signal. This caused the screen to flip erratically, making the vertical position of the bed vary frame by frame.

Areal LIF experiments sought out spatial information on the qualitative character of turbulent mixing. In these experiments, the image acquisition process was the same as previously described. In this analysis, however, a small portion of the total intensity matrix was saved to the hard drive. Typically this matrix, which will be referred to as the image frame, consisted of about 100-120 pixels on either side. Because a pixel was usually 200-400 μm, the image frame was typically 4x4 cm. Billows of most of the fronts were about this size when fully developed. Once the image frame was saved, it was transferred to Spyglass, a image manipulation software package. The cylindrical lens did not produce a uniform sheet of light perpendicular to the source, but rather a Gaussian in this direction. This is typical of most cylindrical lenses and can also be derived from basic optical theory. To correct for this lateral attenuation, the bottom row of the image frame was extracted and recorded. Assuming that the concentration of fluorescein (and therefore dense fluid) was uniform in this lateral, streamwise direction, and that the degree of attenuation did not change much in the vertical, the average intensity signal of this bottom row was considered to be representative of the lateral attenuation of light intensity of the laser. The bottom row was then copied into a matrix, row by row, with the same dimensions as the image frame. Each term in the new matrix was then inverted, and then multiplied to the image frame. The resulting matrix was smoothed with a 3x3 kernel (the same one used earlier) and used as the final image of the front. False color (rainbow, here) was used to enhance the differences in concentration. False colorization works by assigning a color (violet-red) for each intensity (0-255).

Typically, the image frame was taken a significant distance from the source of the laser and was considerably smaller (*i.e.*, its edges) than this distance. Particular attention was paid to the image size and placement. The bottom row was chosen to have constant concentration and the edges (in the streamwise direction) were made within the well-illuminated part of the front. This allowed for a fairly smooth, consistent picture of the billows. Though both of the assumptions made above (*e.g.*, not much change in the lateral attenuation in the vertical direction and constant concentration in the streamwise direction in the underflow) were most likely valid, quantitative error estimates were difficult.

Oftentimes, to observe the development of features similar to the ones discussed below, it was necessary to skip (3-10) frames. It was found that, if the flow was sampled frame by frame, the image did not change very much. This was a testament to the ability of the LIF technique to capture most scales of the flow in terms of relative concentration, even at 30 Hz. Therefore, in all of the results, the time separation in the images is noted with the figure. A video was made with approximately one second of information (30 frames) showing the evolution of a billow for a large-scale front. A copy of the video can be obtained via computer disk from the author.

4.5 Acoustic Doppler Velocimeter (ADV) Results

The raw velocity profile results can be found in Appendix 3. Some early problems with the ADV, resulted from reflection off the bed for heights between 2.5 and 6 cm. These problems only amplified the noise in the signal and did little to the mean signal over time. The problems were corrected after the third ADV experiment shown (after EXP37) with an optimization of the source code (*i.e.*, the software). An asterisk denotes questionable data in the first few runs.

Fig 4.11 illustrates the dimensionless velocity versus the dimensionless height in the overflow region. Theoretical shapes, derived previously, are shown for contrast against the data and the theoretical shape of the collapsed curve of BS. A typical profile for the entire depth is given in Fig 4.12, which also includes a profile of a fixed bed front. The discontinuity in the profile resulted from the unsteadiness mentioned above. Because the accuracy and consistency of the velocity profiles was necessary for the theory outlined above, a discussion of the unsteadiness and its possible source and consequences will be given at greater length in Chapters 5 and 6. The theory derived above also suggested two important relationships (densimetric Froude number and dimensionless mixing versus height ratio). The experimental data is plotted along with corresponding theoretical curves in Fig 4.13 for the relationship between Froude number and height ratio for fixed values of the dimensionless mixing. The theoretical curves are denoted with the corresponding value of the fixed dimensionless mixing rate (μ_{NEW}, for the solution of (4.2.18a) here, and μ_{BS}, for the solution of (2.9a) of BS). In Fig 4.14, the dimensionless mixing is plotted while the Froude number (f) is held constant. The data set is identical to that used for the Chapter 3 plots when the data from experiments where velocities profiles were not taken are removed. These data were omitted because the determination of h_4 cannot be found without knowledge of the velocity profile.

TKE profiles for various types of fronts (differing degrees of mixing) were also calculated and are shown in Fig 4.15. These three experiments were run at the same weir height (30 cm). All of the turbulent profile data can be found with the mean profile data in Appendix 3. As was mentioned above, autocorrelations and power spectra were generated with marginal success. Autocorrelations were produced from the streamwise and vertical velocity records for three different dimensionless mixing rate fronts (EXP38, EXP39, EXP40). These were the same three experiments as the ADV TKE profiles mentioned above. The autocorrelations can be seen in Figs 4.16, 4.17 and 4.18. Heights above the bed and degree of dimensionless mixing are shown along with the figures. Precise measurements of all of the relevant dimensionless parameters for these experiments can be found in Appendix 1. All of the autocorrelations were taken at the point which corresponded to the highest TKE measurement. The variation of these points with dimensionless height can be seen in Fig 4.15, as well as the general shape of the TKE profiles. The

autocorrelations were not produced from the power spectrum, as is common practice, because of problems with aliasing and record length. The records were rather run through a more basic, 'direct' autocorrelation equation. This equation is described by

$$R_{xx}(r\Delta t) = \frac{1}{N-r}\sum_{n=1}^{N-r} x_n x_{n+r} \qquad (4.5.1)$$

where x_n is the nth realization, N is the record length, r is the number of records lagged, Δt is the separation in time of the samples and R_{xx} is the autocorrelation. This formula was also used to produce the autocorrelation of Fig 4.7. Equation (4.5.1) can be found along with a rather exhaustive discussion of autocorrelation estimation in Bendat and Piersol (1986). Though power spectra were calculated, none were shown because of the aforementioned aliasing and record length problems. The experiments presented herein were conducted in such a way to produce consistent, quality mean and bulk turbulence measurements. Techniques and procedures used were not designed or capable of producing repeatable, 'clean' (free from noise and aliasing) power spectra. Further discussion of the turbulence data that can be extracted from the experiments can be found in Chapter 6.

4.6 Laser-Induced Fluorescence (LIF) Results

Because of the complexity of producing relative concentration profiles using this method, few were produced in course of this study. However, the resolution of each profile was remarkable (approximately 400 points, with almost 100 in the billow region). An illustration of one of these profiles can be seen in Fig 4.19. Note that the concentration is only relative (with respect to the mean in the underflow) and that the concentration drops suddenly towards the bed (which was not included in the calculation of the mean in the underflow). A slight deviation from pure mean behavior near the bed (< 1 cm) resulted from some unknown process discussed in Chapter 6.

Many mixing events were identified and cataloged in just the few experiments described herein. Mixing seemed to occur in two different modes. The first and most familiar, was billowing (*i.e.*, from the Kelvin-Helmholtz instability at the front), which was identified by short bursts of concentrated fluid ejecting high into the flow. This type of mixing is illustrated at the top of Fig 4.20. These events are highly intermittent for large-scale fronts. A characteristic frequency of the billows can defined by the velocity difference between the top and bottom of the billow and the height (diameter) of the billows. Matching of this frequency (most probably predicted well by

the theory of Thorpe, 1973) with the frequency of the internal waves on the interface of the current body will be discussed loosely in Chapter 6.

A smaller scale (smaller Re_q) billow event is shown in Fig 4.21. Here, attenuation effects did not need to be adjusted for because of the smaller size of the image frame with respect to the width of the laser. In other words, the image frame was unadulterated, except for the obvious false colorization. The image frame of Fig 4.21 was slightly less than 2x2 cm. Also, the billows of the smaller scale fronts did not seem to grow like the larger scale fronts. They (smaller scale billows) also did not change in character (*e.g.*, shape), retaining their form far downstream of the front.

Another type of mixing witnessed, only in the larger scale fronts, was what could be described as nibbling. An illustration of this process is shown at the bottom of Fig 4.20. This type of mixing, observed by others in mixing layers, occurred on a much larger time scale than the billowing. Nibbling moved in slow advances and retreats and appeared to mix a small amount of fluid continuously. A more detailed description and discussion can be found below in Chapter 6.

Table 4.1 Results of salinitiy sensivity test on ADV

Trial Number	Sampling Time (sec)	Estimated Salinity (ppt)	Mean Streamwise Velocity (cm/s)	Height Above Bed (cm)
1	59.15	7	3.42	6.32
2	59.15	0	2.71	6.18
3	40.95	20	3.19	6.43
4	40.95	7	3.50	6.23

Trial Number	Mean Transverse Velocity (cm/s)	Mean Vertical Velocity (cm/s)	Mean TKE (cm^2/s^2)
1	-0.181	-0.404	3.65
2	-0.011	-0.235	3.51
3	0.308	-0.425	4.21
4	-0.022	-0.328	3.68

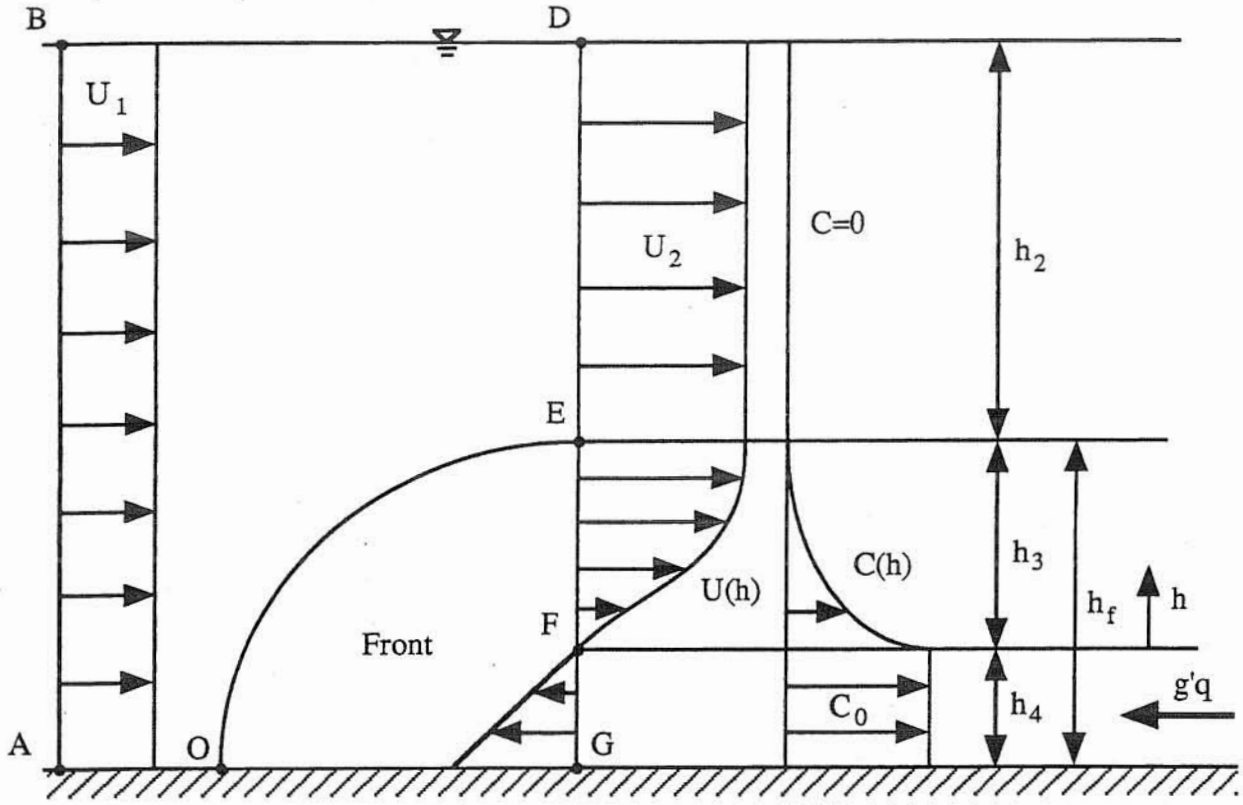

Figure 4.1 Illustration of variables and control volume used in the conservation of momentum and mass analysis.

* Note that all profiles (velocity and concentration) were obtained at the same cross-section, DEFG. All height measurements also refer to this cross-section. The length of DEFG is equal to h_1.

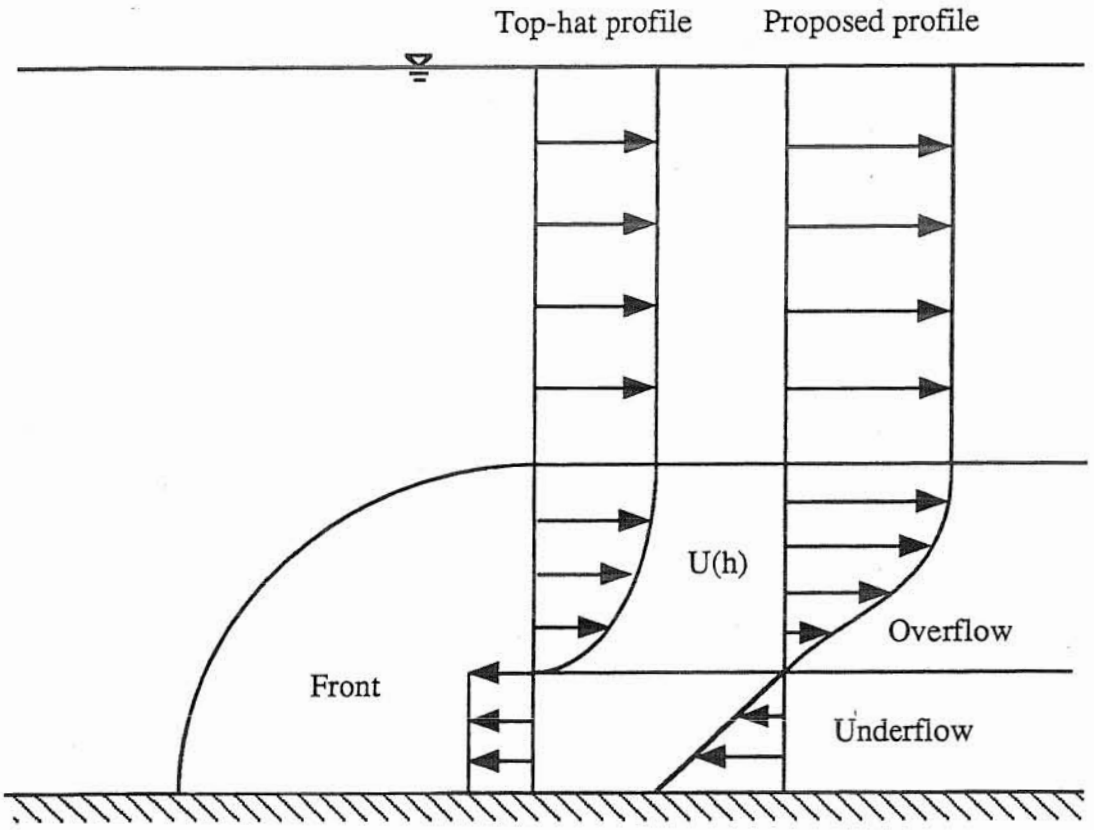

Figure 4.2 Comparison of BS, top-hat profile to the profile proposed herein

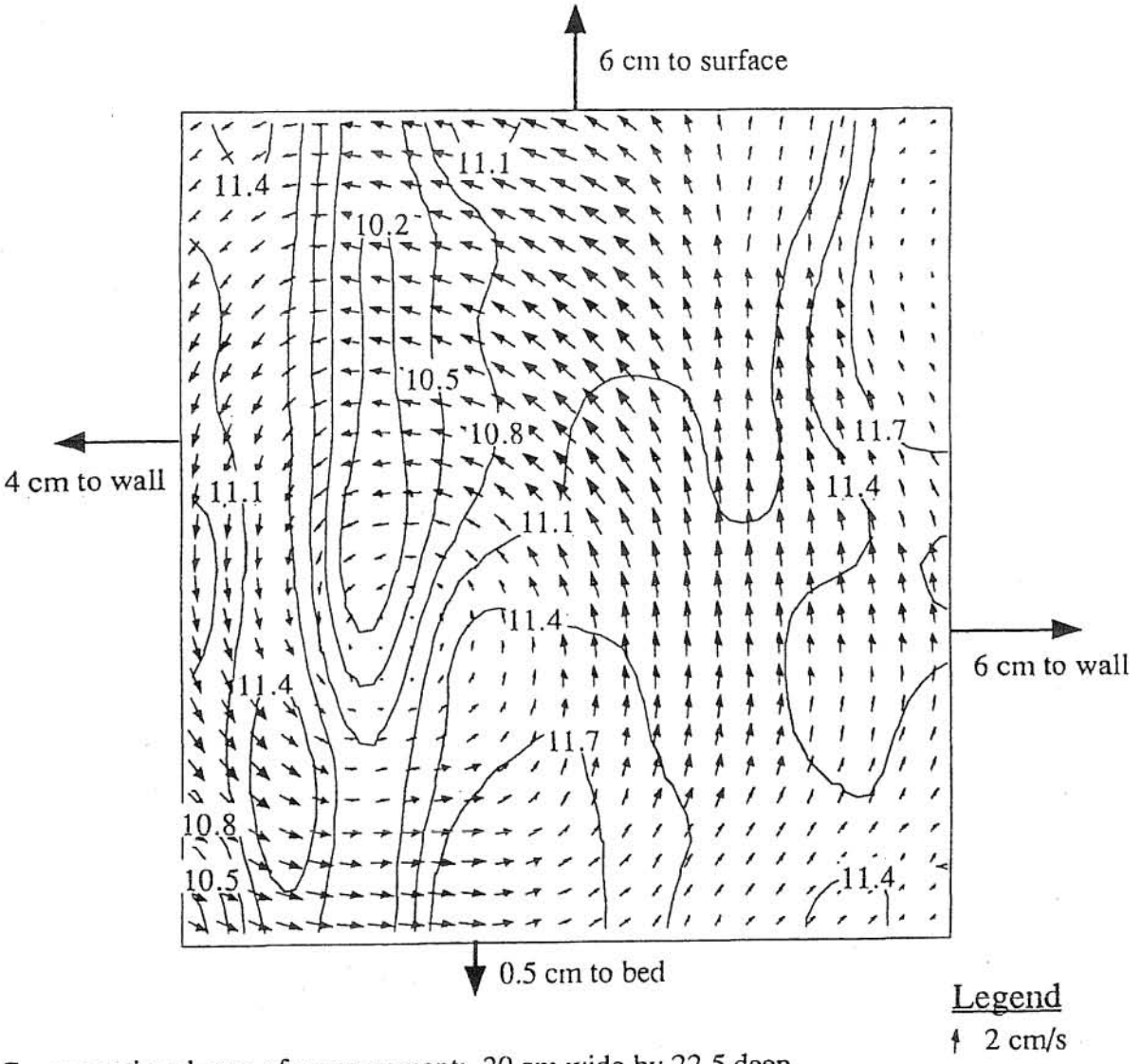

Cross-sectional area of measurement: 20 cm wide by 22.5 deep

Location of the profile: middle of conveyor belt (with the conveyor running)

Contours of mean streamwise velocity are in cm/s

Figure 4.3 Three-dimensional velocity cross-section taken with the ADV. Arrows outside the box indicate how far the measurement area is from the boundaries of the flow. Arrows inside the box indicate transverse and vertical components of mean flow with the scaling shown.

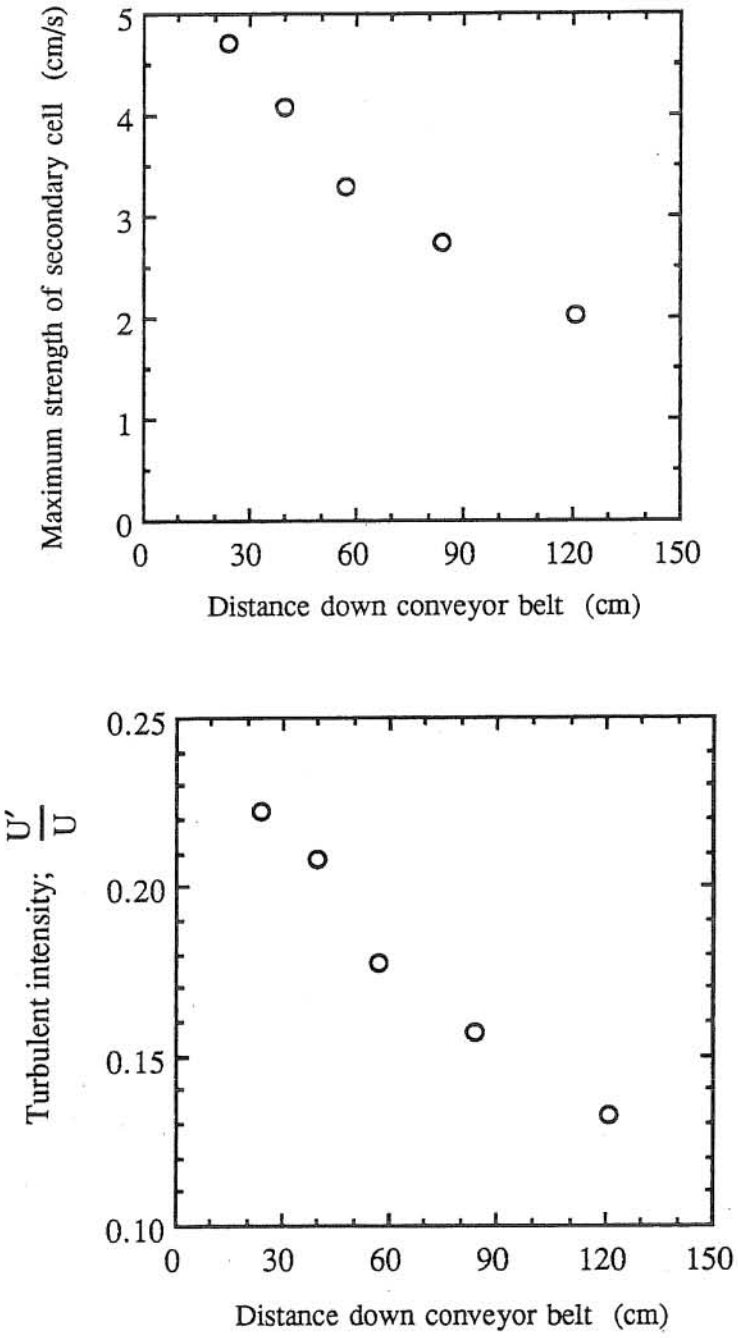

Note: The toe of the belt is located
150 cm downstream of the constriction.

Figure 4.4 Illustration of decay of secondary cells and turbulent intensity downstream of the constriction

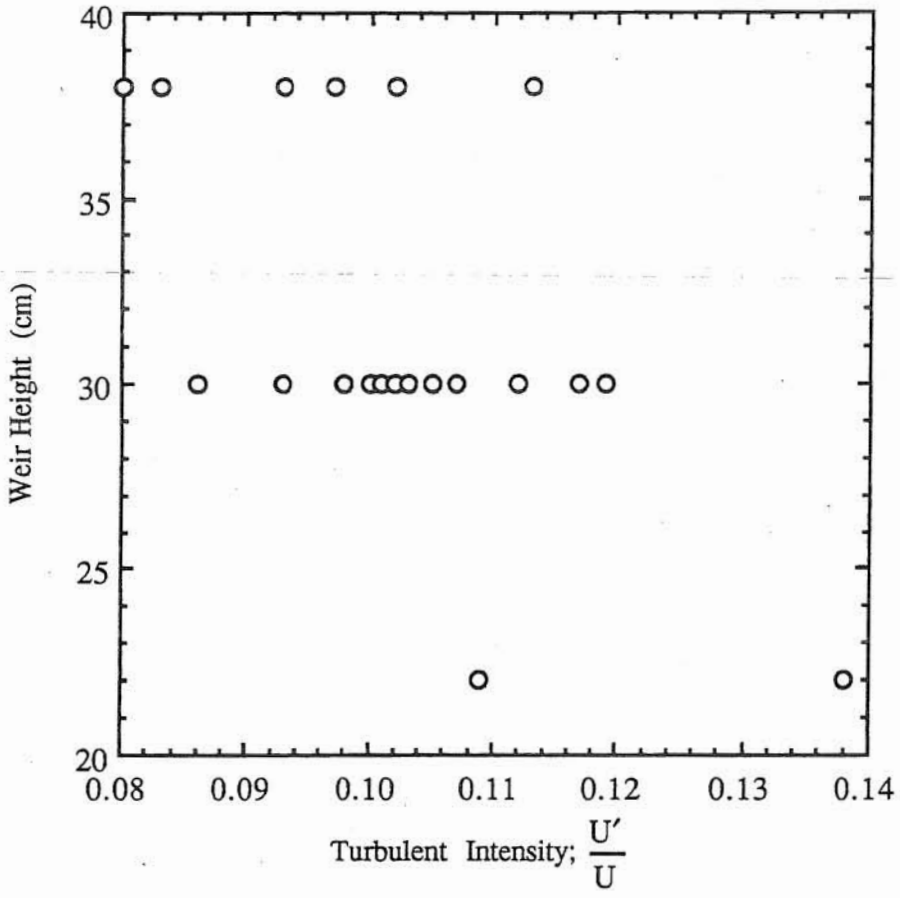

Figure 4.5 Background turbulent intensities for all experiments as a function of weir height

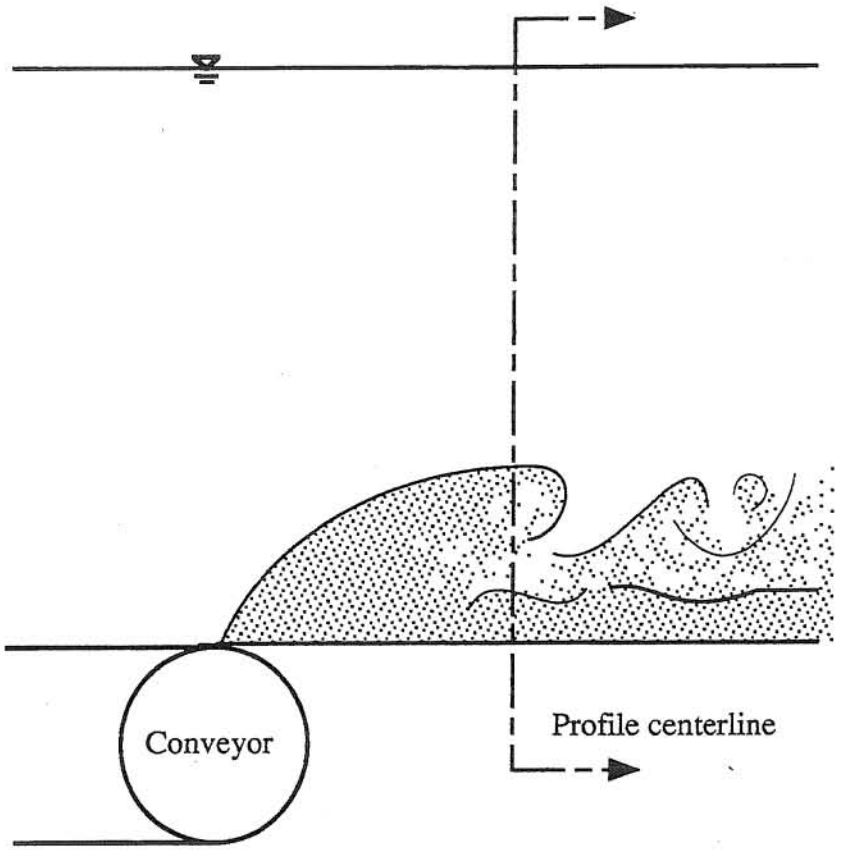

Figure 4.6 Illustration of profile centerline

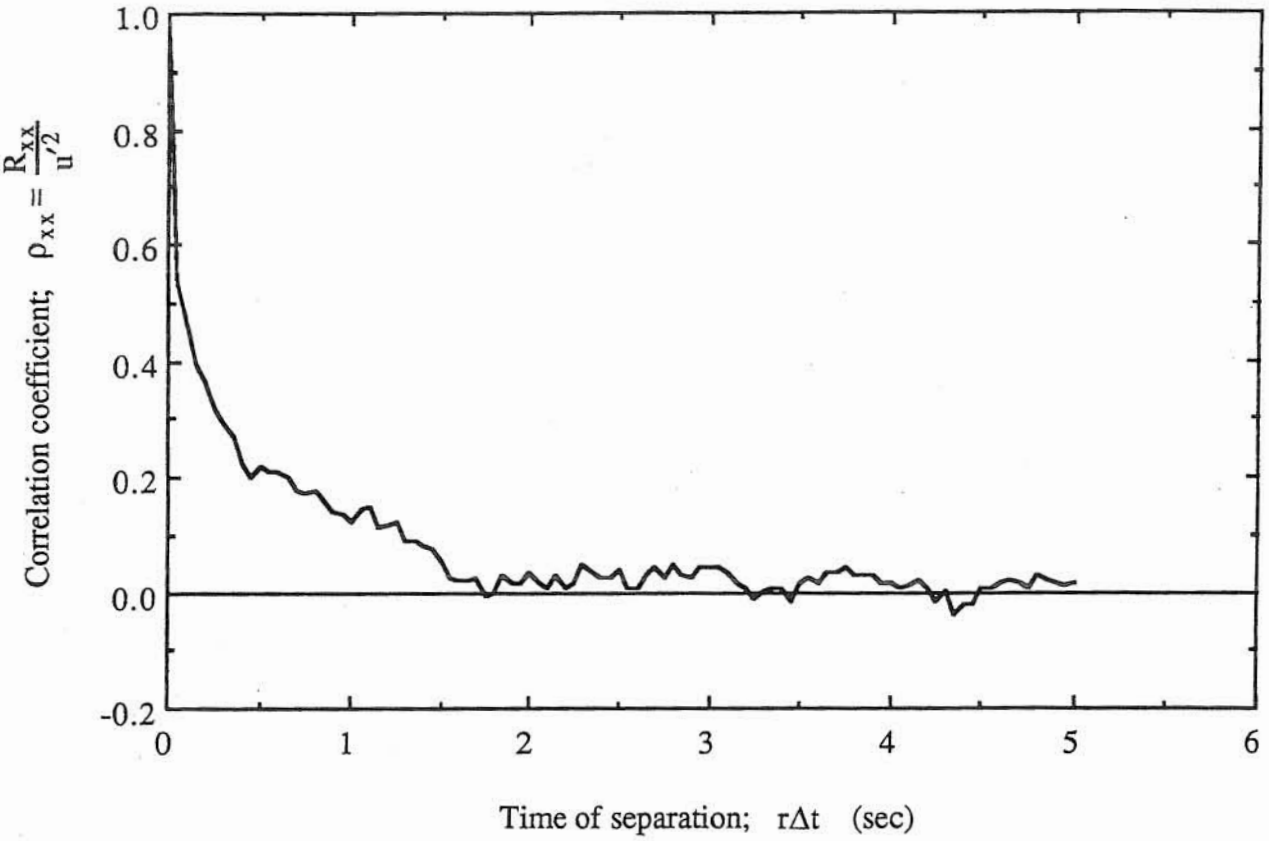

Figure 4.7 Streamwise velocity autocorrelation in channel without front (*i.e.* wall bounded flow). Experimental conditions were open channel flow with mean velocity about 9 cm/s. Flow depth was approximately 40 cm and the sampling height was about 22 cm above the bed.

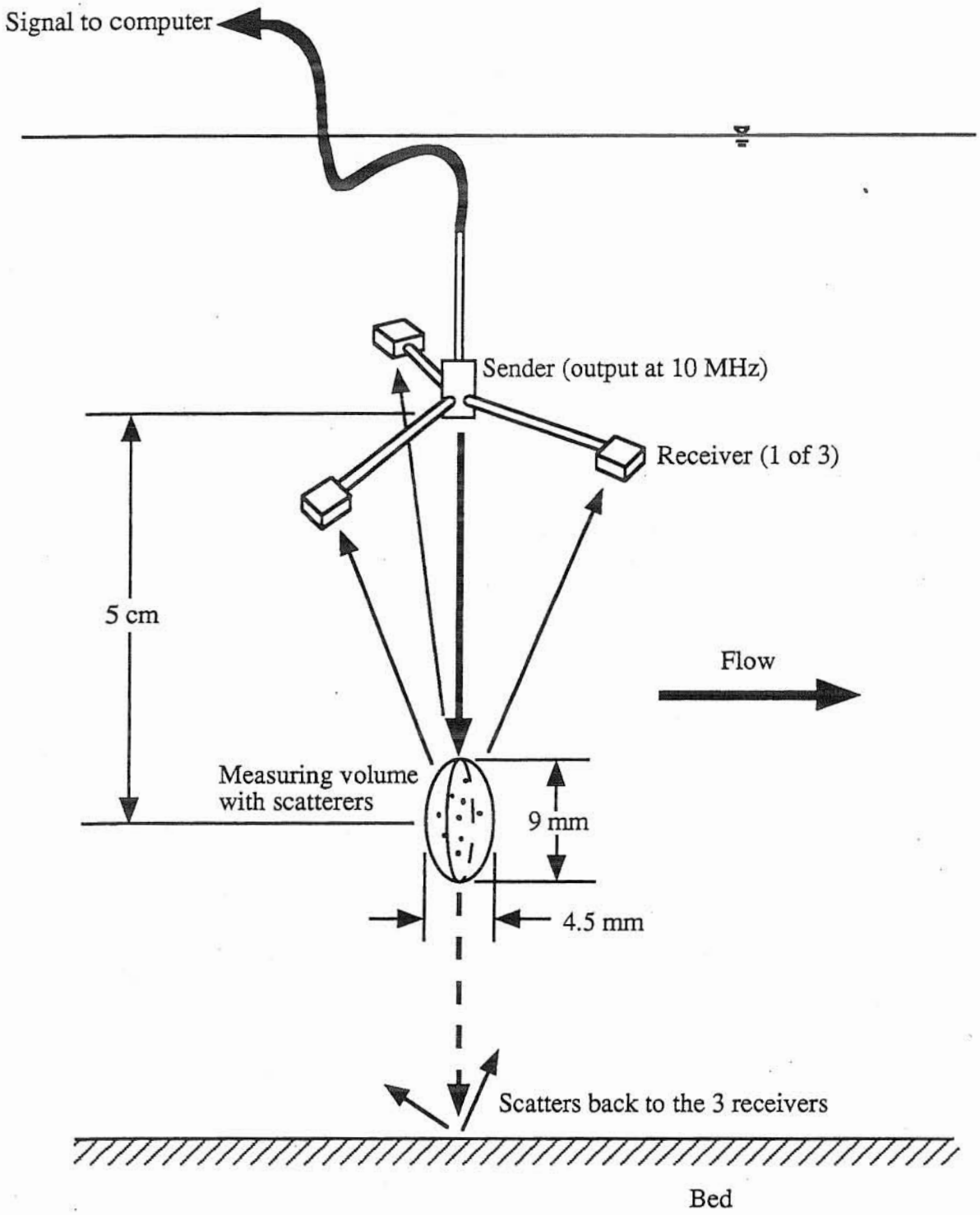

Figure 4.8 Schematic of Acoustic Doppler Velocimeter (ADV)

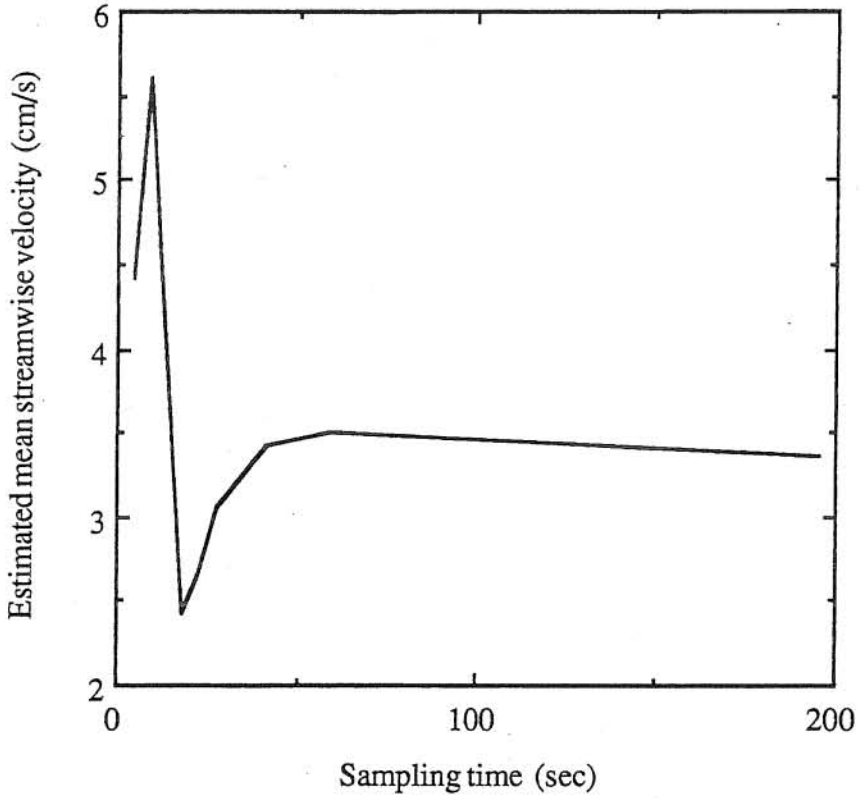

Figure 4.9 Effect of sampling time on mean velocity (sampling rate is 25 Hz)

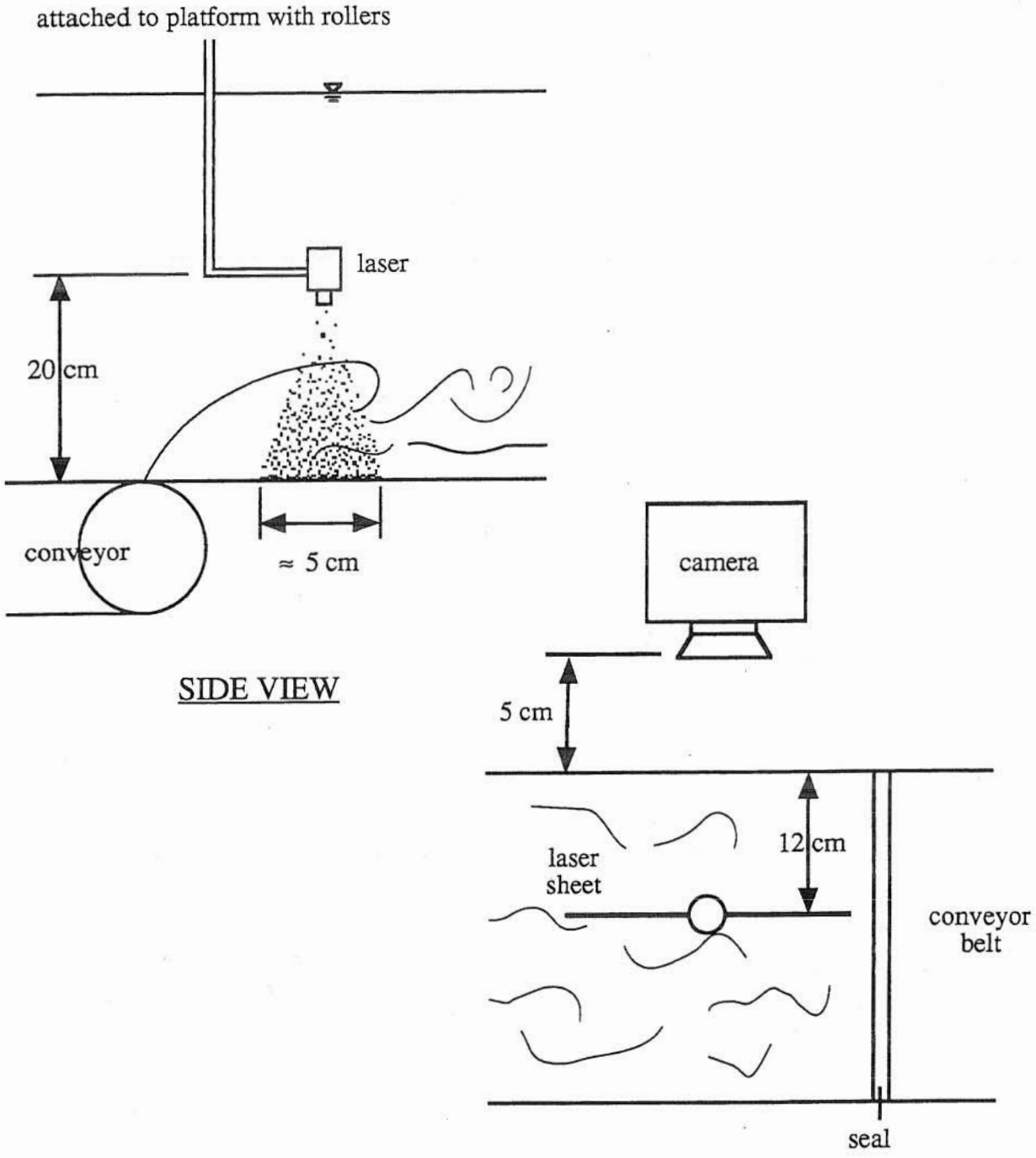

Figure 4.10 Illustration of experimental setup of the Laser-Induced Fluorescence (LIF) technique

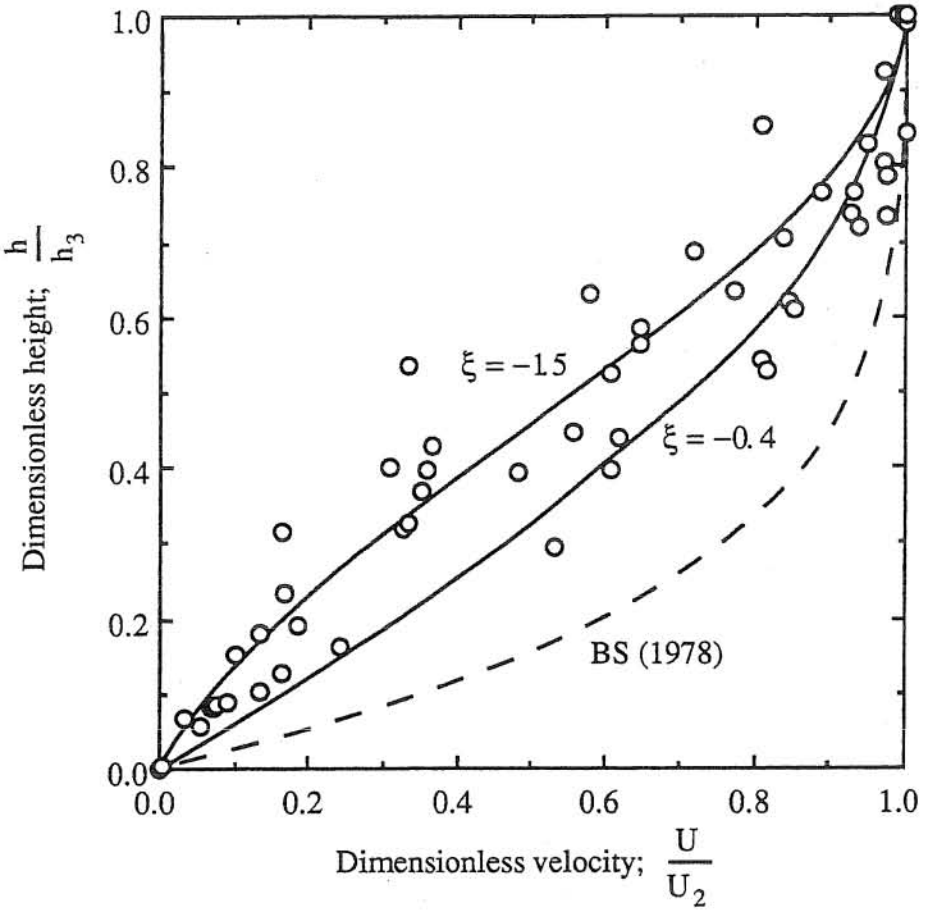

Figure 4.11 Dimensionless velocities versus dimensionless height for the overflow. The present theory (solid lines) and the theory of BS (dashed line) are also plotted for comparison to all of the velocity profile data taken over the course of this study (open circles).

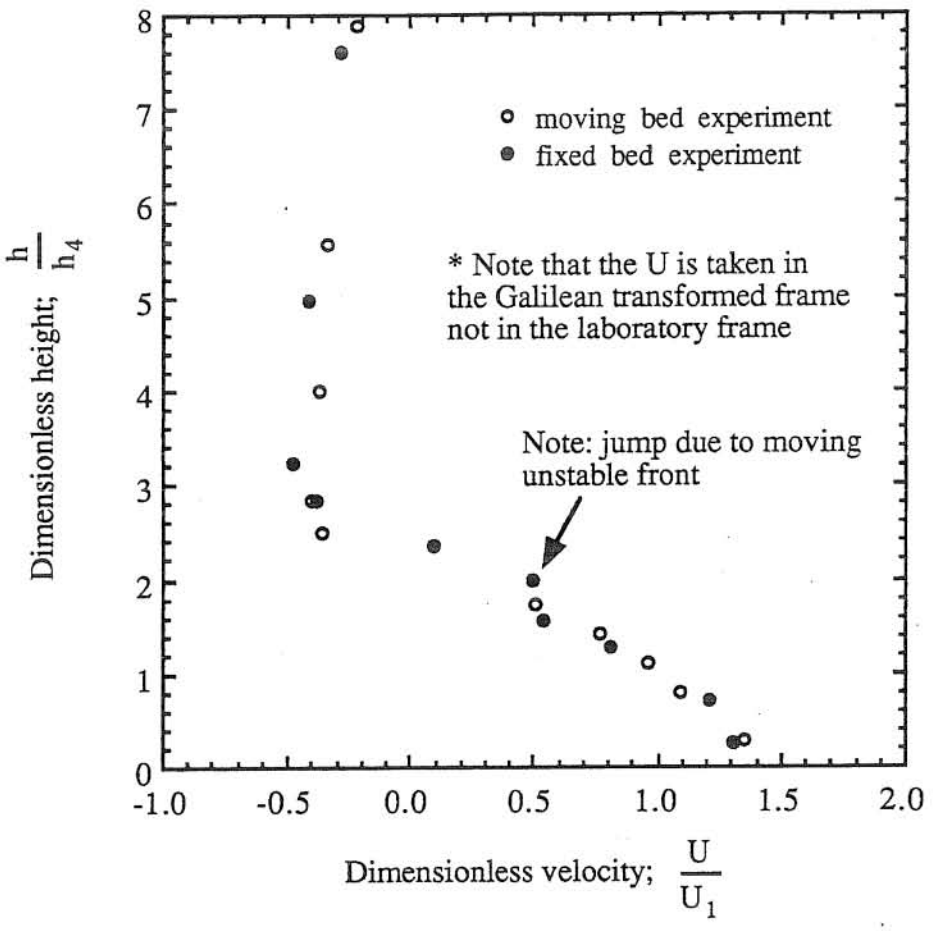

Figure 4.12 A comparison of boundary condition to the profile shape and experimental feasibility of two similar fronts. Experimental conditions are similar to EXP39 and can be found in Appendix 2.

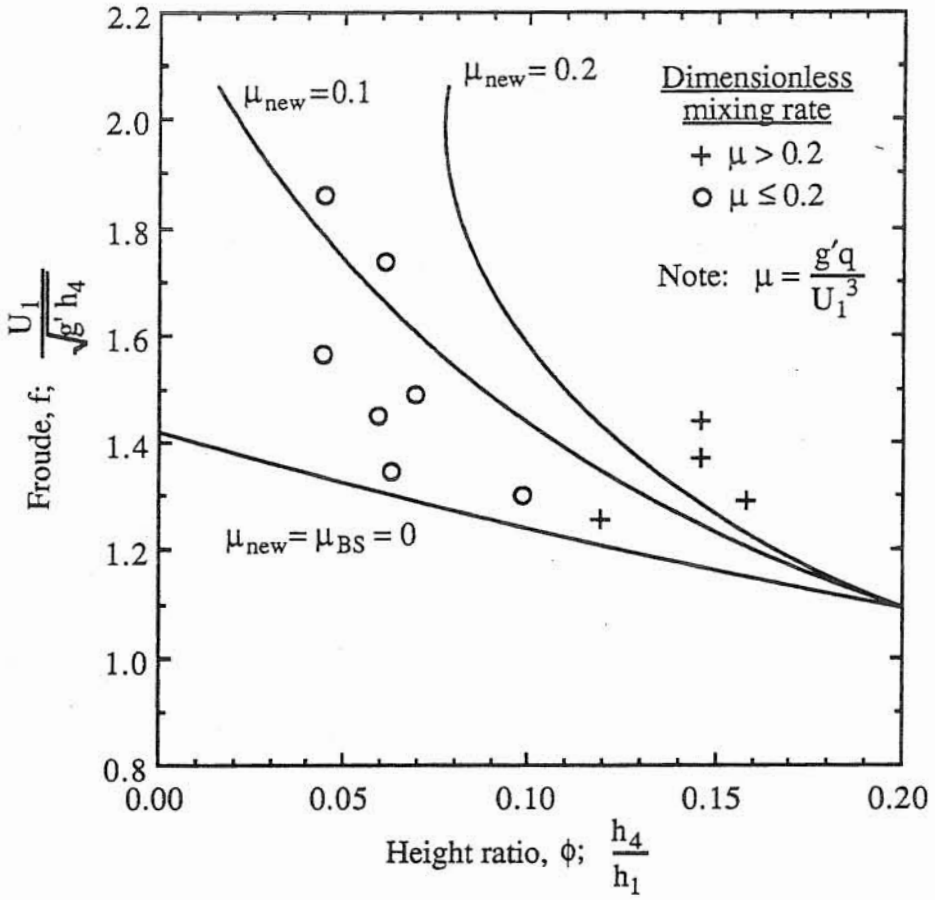

Figure 4.13 Evaluation of theory against experimental data for fixed values of the dimensionless mixing rate. Fixed values of the dimensionless mixing used in the solution of (4.2.18a) here and (2.9a) of BS are denoted μ_{NEW} and μ_{BS}; respectively.

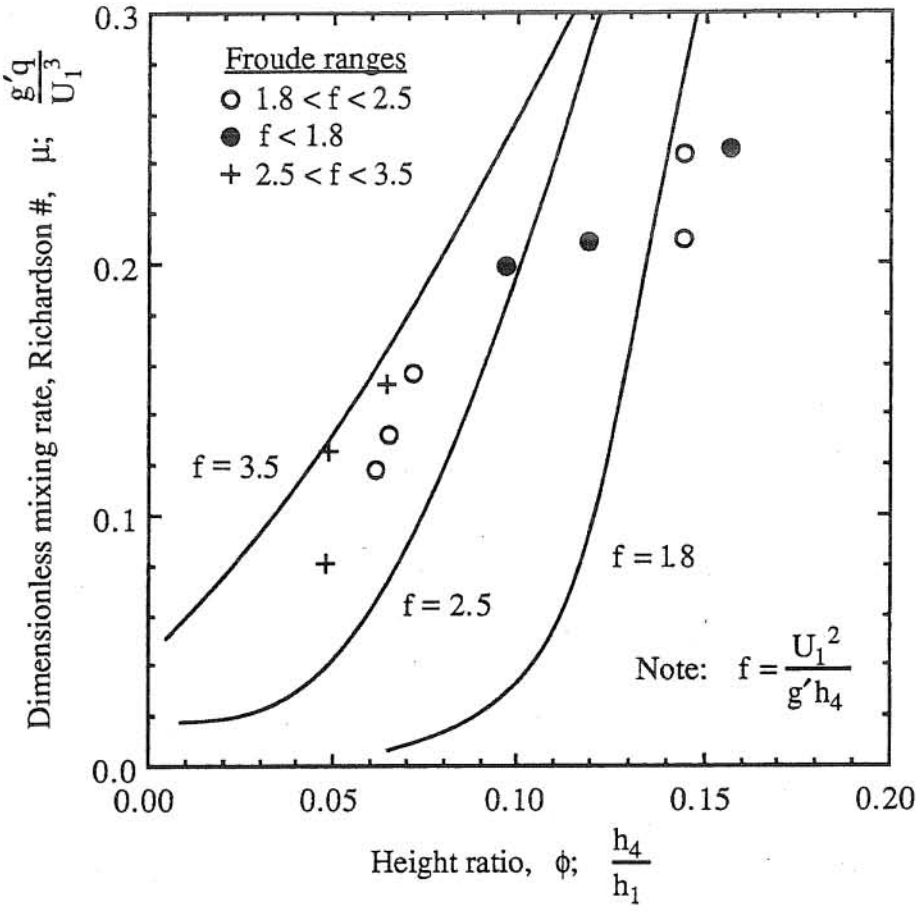

Figure 4.14 Evaluation of theory compared to experimental data for fixed values of the densimetric Froude number

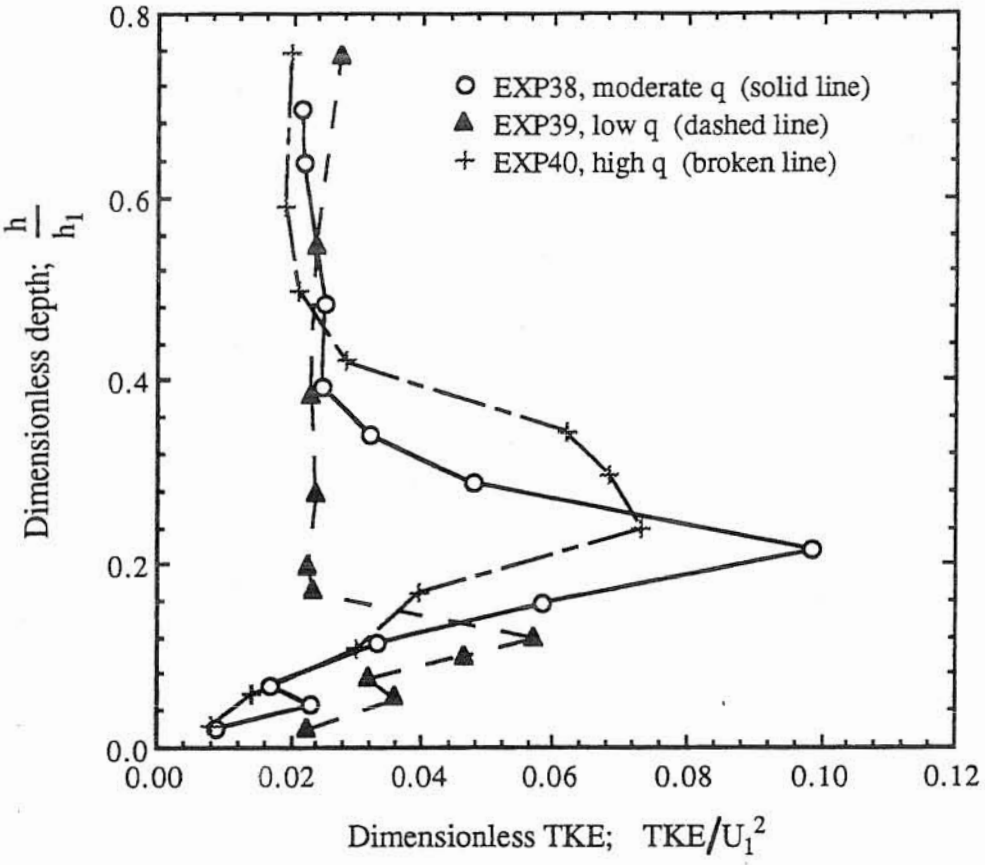

Figure 4.15 Dimensionless TKE profiles for different mixing rate fronts

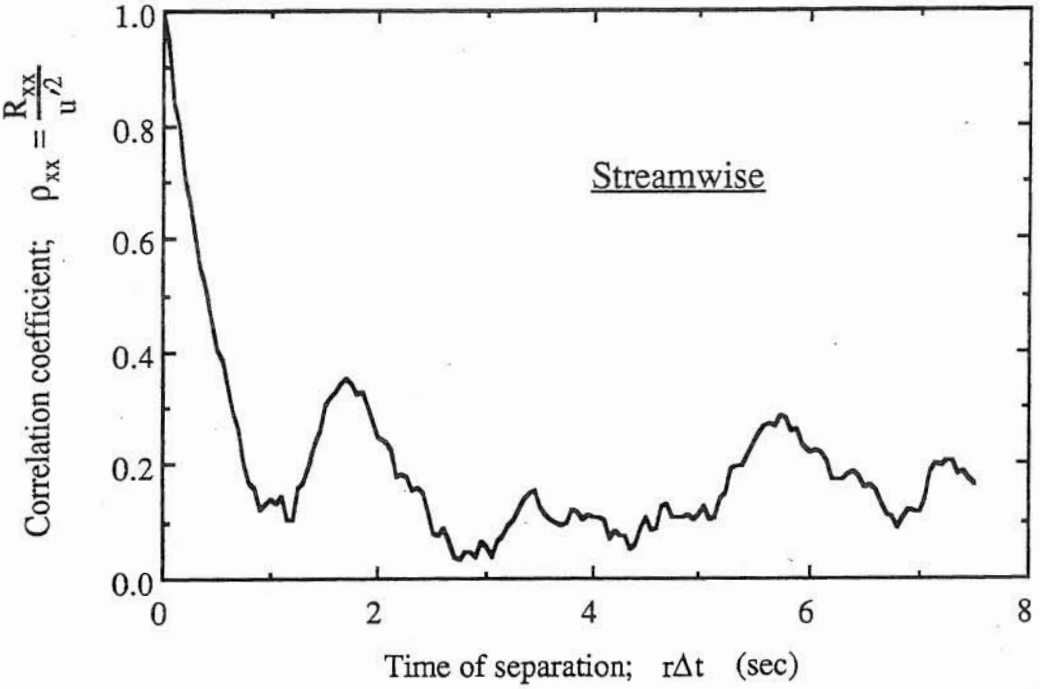

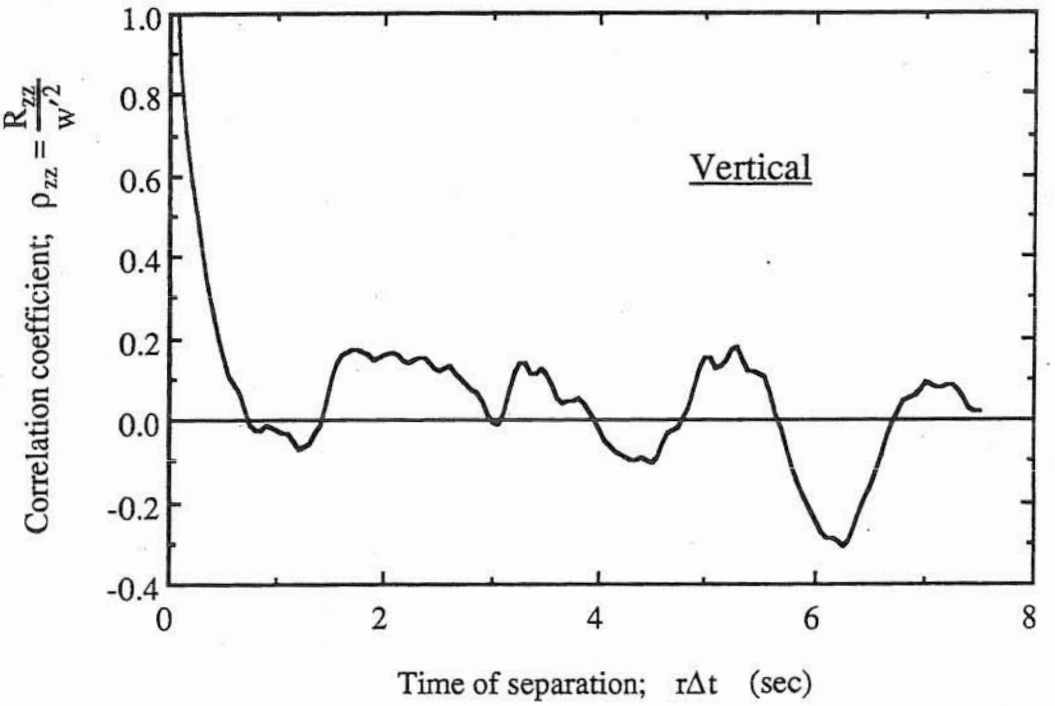

Figure 4.16 Autocorrelations of streamwise and vertical velocity in EXP38. The data was acquired 8.31 cm above the bed. EXP38 was a moderate mixing rate experiment.

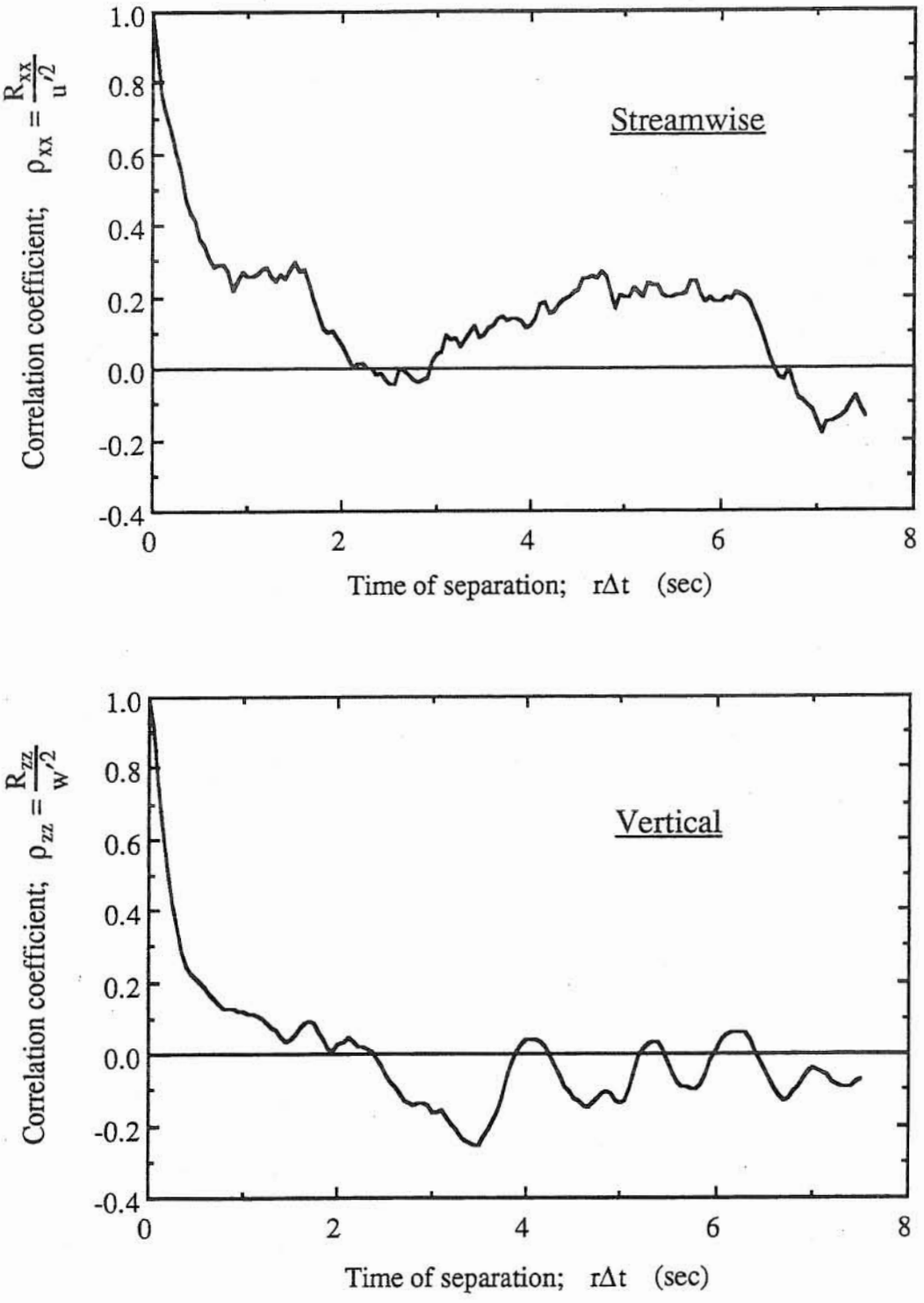

Figure 4.17 Autocorrelations of streamwise and vertical velocity for a point in EXP39. The data was acquired 4.63 cm above the bed. EXP39 was a low mixing rate experiment.

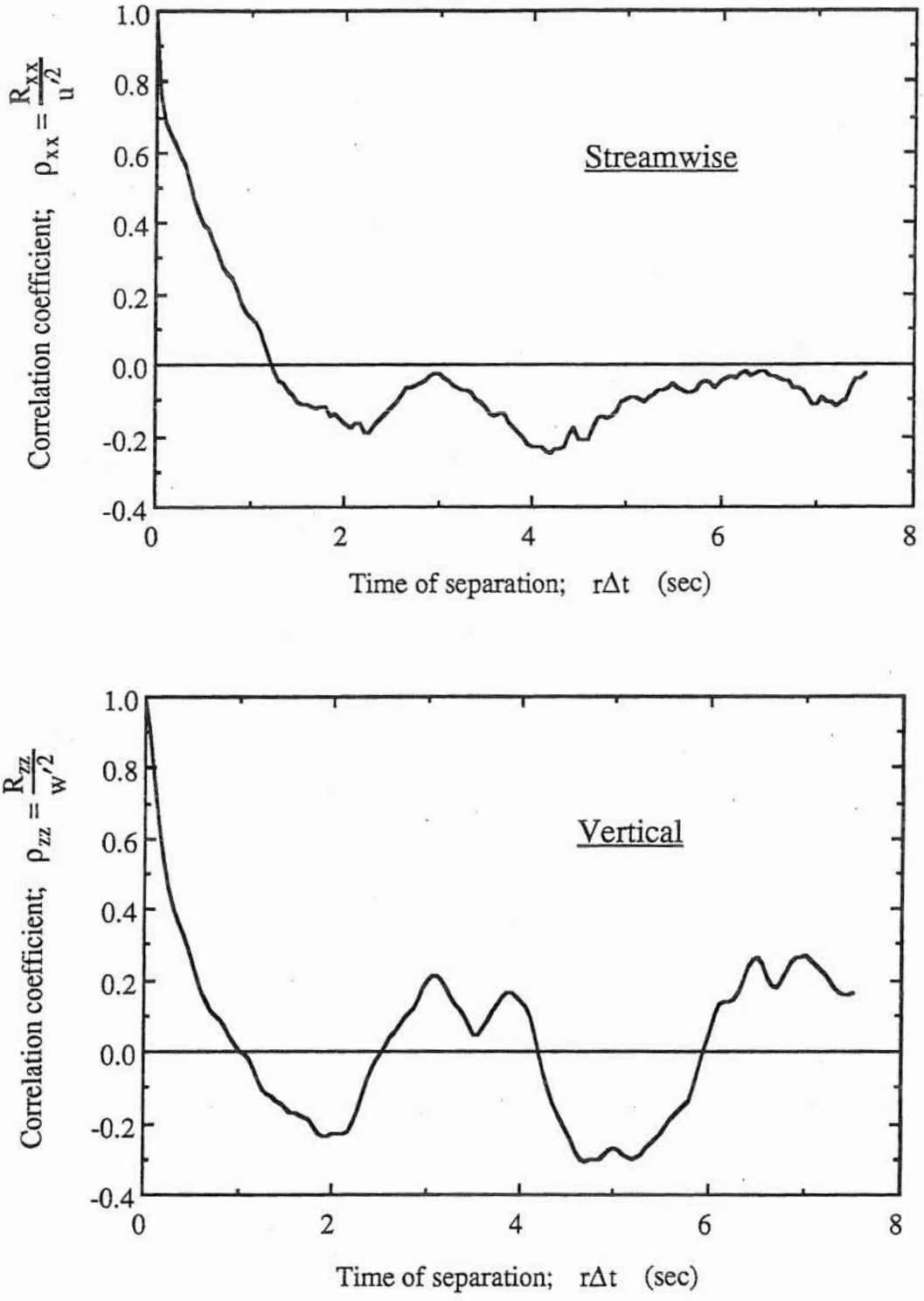

Figure 4.18 Autocorrelations of streamwise and vertical velocity in EXP40. The data was acquired 9.19 cm above the bed. EXP40 was a high mixing rate experiment.

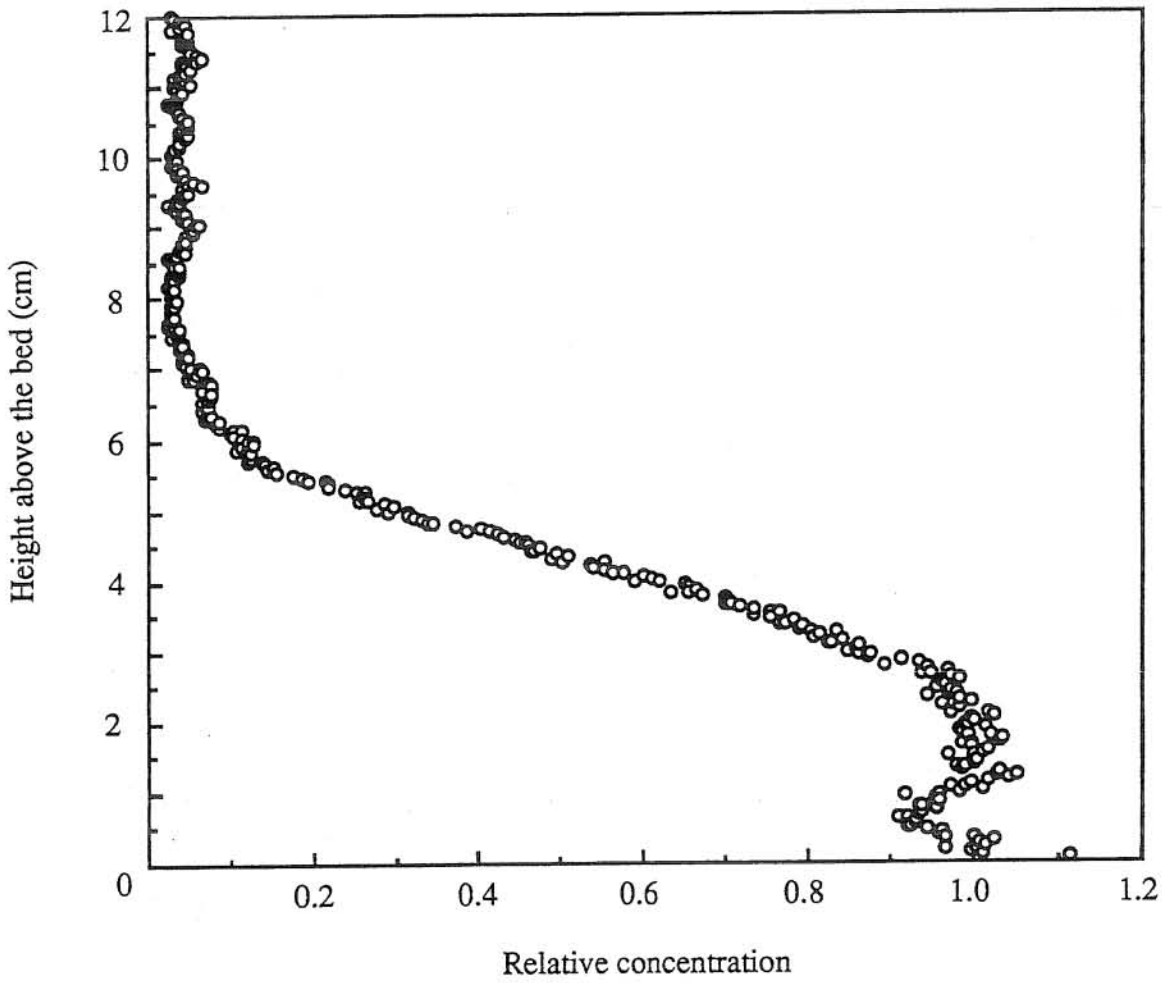

Figure 4.19 Relative concentration profile for experiment nominally similar to EXP38.

Billowing

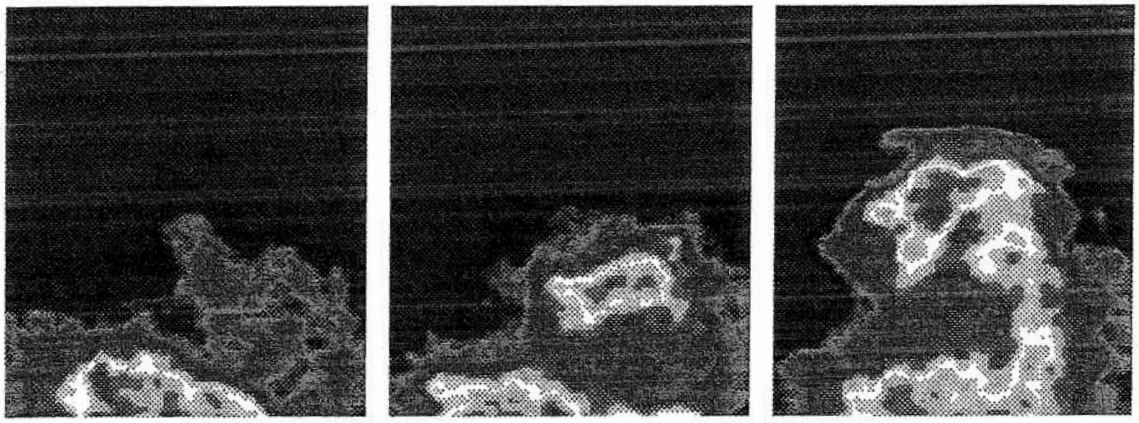

Nibbling

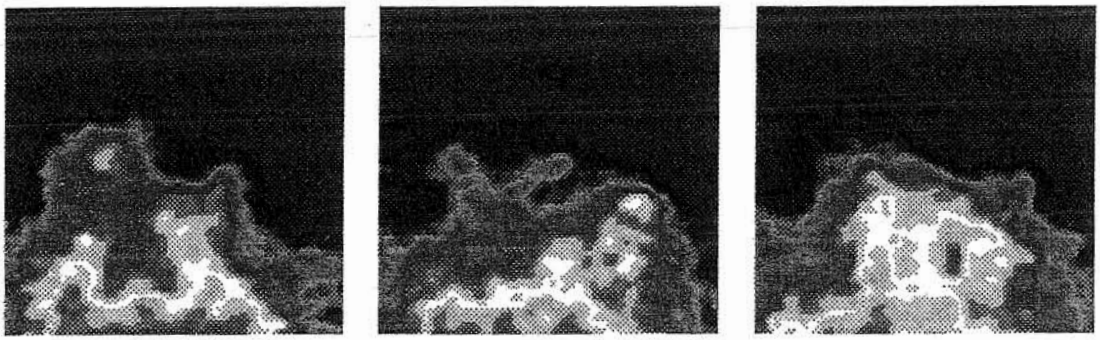

Figure 4.20 Illustration of major mixing processes in large scale saline gravity current fronts

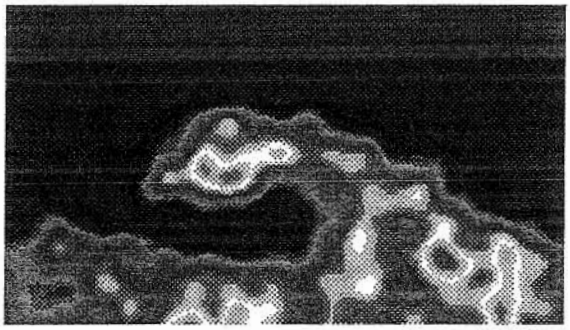

Figure 4.21 Billow of low Reynolds number front

5. ANALYSIS OF BULK FLOW RESULTS

5.1 Generalities

As can be seen from the results of the bulk flow experiments, scale influenced the behavior of the fronts. The duplication of the relationship of the height ratio to the densimetric Froude number, as well as the dimensionless mixing rate for smaller flows (BS-sized), found by BS was a testament to the validity of the increased mixing rates seen in the larger scale flows. Aside from proving scale effects, an important goal of the research conducted here was to establish a simple relationship between the three important dimensionless parameters (dimensionless mixing, densimetric Froude number and height ratio) for field-scale conservative gravity current fronts.

5.2 Froude Number

Fig 3.5 graphically illustrates the range of densimetric Froude numbers covered in the experiments herein. The range was similar to a portion of the data range of BS. Duplication of height ratio and densimetric Froude number data should occur according to the similarity theory proposed by Keulegan (1957a, 1958). It should be noted, however, that the way h_5 is defined in this study was somewhat different from the definition of BS. To clarify these differences in definition, these parameters will be specifically defined again. First, h_5 was the visible height of the current behind the front, whereas h_4 was found by locating the height at which the velocity reverses (velocity is equal to zero) in the laboratory reference frame. BS did not distinguish between these two definitions for the characteristic height of the current behind the front or underflow. They simply referred to a general characteristic underflow height, h_4. This was partly due to the mixture of methods used to measure this value. In their experiments, h_4, like the definition used here, referred to the height above the bed where the velocity was equal to zero. However, because they used a device which could not detect flow reversal (a hot-film anemometer), they first determined this point visually from dye streaks, which was similar to the visual method used in the determination of h_5 herein. Discrete, quantitative velocity samples (for profiles) were, however, found with a hot-film. Uncertainty to the exact details of their experimental procedure prohibits any further analysis of the comparison.

In the first experiments conducted here, the velocity profile was not resolved at all. Therefore, it was necessary to use the visual definition of h_5. The way these two different definitions (h_4 and h_5) compare for the range of the experiments presented herein is shown in Fig 5.1. Again, it should be noted that the point of zero streamwise velocity was found because the ADV (see Chapter 4 for details) was capable of capturing flow reversal of the streamwise

component of velocity. From this graph it can be seen that for relatively low height ratios, the two values are approximately equal. Because the height ratio is basically inversely proportional to the Froude number, this range corresponds to higher Froude numbers. The relationship becomes more complicated for higher height ratios, with the two definitions becoming increasingly distinct. It seemed that the location of interface behind the front (which defines the current height, h_5, in the preliminary experiments) was dependent on whether the front was supercritical or not. All of the corresponding currents of the fronts examined here were theoretically supercritical (current Froude number, $U_f/g'h_5$, greater than unity), however, some of the higher height ratio experiments were only marginally supercritical. In this case, the interface behind the front was not as distinct (no refraction or reflection of light was seen from the interface) and was estimated to be much lower than the actual point of zero velocity. This phenomena has been observed before by Tsihrintzis (1988) and Alavian (1986). Their reasoning of the process was similar to that presented here.

5.3 Mixing

The most important parameter for the purposes of this study, however, was the dimensionless mixing rate. Fig 3.6 illustrates the relationship between this parameter and the height ratio. The relationship was not unique and seemed to depend strongly on the weir height, which could be thought of as a measurement of scale. For each weir height, it seemed that the relationship for dimensionless mixing was linear with height ratio. This simple relationship should not be taken as something inherently fundamental, but rather a somewhat coincidental result of the particular variation of Reynolds and Froude number and dimensionless mixing rate, unique to the experimental procedure and apparatus. Actually, a significant finding of this study was that this relationship between the Froude number, height ratio and the dimensionless mixing was far from unique and quite complex. These interdependencies will be explored further in later sections.

It is interesting to note that the results of BS can be duplicated rather precisely for their set of initial experimental conditions, where a seemingly weak linear relationship occurred between the dimensionless mixing rate and the height ratio. After making the facility operate at a much larger scale, using an identical procedure, a different linear relationship could be found. Though (3.2.7) attempts to explain this linearity from theoretical grounds, it can only show that the relationship will be linear if the Reynolds number and Froude number are constant.

Though BS and Simpson and Britter (1979) never claimed that their relations were entirely unique, though it was implied in later works (*e.g.*, Thomas and Simpson, 1985). The fact that the range of Froude numbers was quite limited for both the facility here and BS suggested a possible 'equilibrium' Richardson number. A Richardson number of the overflow region can be defined by

$$R_L = \frac{g' h_3}{\Delta U^2} \tag{5.3.1}$$

where R_L is the Richardson number, g' is the reduced gravity, h_3 is the height of the overflow and ΔU is the velocity defect or difference in the velocity of the underflow (U_4 or $\overline{U}_4$) and the velocity of the overbearing clear flow (U_2). Thorpe (1973) formulated this Richardson number and theorized that it should be constant for fully developed, 'equilibrium' billows. BS confirmed this result by finding a nearly constant value for all their experiments ($R_L = 0.35 \pm 0.1$). A similar result was found in the experiments herein, with a slightly larger spread in the data ($R_L = 0.35 \pm 0.15$). The ramifications of this relation to dynamics of the mixing will speculated upon briefly in Chapter 6.

5.4 Scale Effects

As mentioned in the previous section, the scale effects cannot be completely attributed to a viscous term (*e.g.*, a Reynolds number). This is illustrated quite well in Fig 5.2. In this graph, the Froude number is plotted against the slope of the line on the mixing plot (Fig 3.6), represented by the ratio of dimensionless mixing rate and height ratio. The third parameter in (3.2.7), the mixing Reynolds number (Re_q), stratified the data. The complexity of the function Φ_7 of (3.2.7) can also be seen in Fig 5.2. However, a monotonic trend in the slope of the mixing rate line for a constant Froude number with increasing Re_q was unmistakable. The slope of the dimensionless mixing rate line, however, was strongly dependent on both the Froude and Reynolds number. This indicated that the viscous limit was dependent on Froude number, which was why the effects described herein were referred to as 'scale' effects and not 'viscous' effects. The function that would relate the 'critical' Reynolds number and the densimetric Froude number was thought to be extremely complex and highly nonlinear. In the past, the product of these two dimensionless parameters has been taken to form what could be called a Keulegan number. It could be defined as in Harleman (1961), however, experimental data did not achieve similarity with respect to this dimensionless number.

Therefore, a more subtle relation was sought out between the three parameters of (3.2.6) by manipulating only the Reynolds number. An ideal relation would collapse all of the data for each scale (weir height) onto one point on the graph of the new collapsed function of Froude and mixing Reynolds number and the slope of the dimensionless mixing rate line. The function of Froude and Reynolds number that best met this criterion can be described by

$$P = \frac{U_1}{\sqrt{g'h_1}}\left[1 + \frac{1}{\log_{10}(q/\nu) - 1.5}\right] \qquad (5.4.1)$$

where $U_1/(g'h_1)^{1/2}$ is the Froude number and q/ν is the Reynolds number in (3.2.6). P is the nonlinear function that accounts for both effects and can be thought of as a scaling parameter. This parameter is plotted against the slope of the dimensionless mixing rate in Fig 5.3. BS was shown as a range because of the uncertainty in the actual range of Re_q. The data collapsed fairly well, particularly for the 22 cm weir height.

Interpretation of Fig 5.3 and the function that describes P was quite complex. It should be noted first that the function that describes P was the best one found from the various techniques that were attempted. A better collapse could exist that describes the phenomena more completely, however, no such relationship was found. Questions also arose as to whether (5.4.1) was a spurious correlation because of the apparent abundance of 'coefficients'. Further analysis of the functional form that describes P, relaxed some of these concerns. First, the function was not as complex as it first appeared. The form, $(1+1/f(Re_q))$, was consistent with a mathematical expression that tends to unity as the limit of Re_q tends to infinity, which agrees with the concept of similarity for large scale flows. Therefore, the only empirical parameter that needs to be found is the constant represented by 1.5 in (5.4.1). A close look at what this parameter represents yielded the idea of a 'critical' Reynolds number. From inspection, it was obvious that P became undefined for mixing Reynolds numbers less than $10^{1.5} \approx 30$. Fronts at this scale would most certainly not be similar with respect to the original Froude similarity of Keulegan (1958) (*i.e.*, using $Re_f = U_f h_f/\nu >$ 2000), as well as the internal processes found here (large Re_q). However, as scale increases, similarity is obtained only with respect to the Froude number, as in some of the experiments herein and in those of BS. Further increases in scale (to the size of fronts in nature) would yield similarity with respect to both external (*i.e.*, Froude similarity of Keulegan) and internal (*i.e.*, mixing) processes.

Though not readily apparent from Fig 5.3, justifications can be made for assuming a lower limit to the parameter P. It is fairly obvious that P, for extremely large scale experiments (*i.e.*, viscosity becomes negligible and Re_q goes to infinity), will simply be equal to the Froude number. It can be hypothesized, however, that the Froude number, as defined above, will also have a lower limit. For larger height ratio experiments the lower limit is clearly defined by the physical condition of non-negative dimensionless mixing rate. This lower limit found theoretically by Benjamin (1968) and can be expressed by

$$\frac{U_1^2}{g'h_1} = \frac{\phi(2-\phi)(1-\phi)}{1+\phi} \qquad (5.4.2)$$

where ϕ is the height ratio. Therefore, the only portion of the physically realizable space of the parameter values left was for smaller Froude numbers in the limit of the height ratio equal to zero. Analysis of this limit was complicated and contained many assumptions. However, BS devoted quite a bit of analysis to quantifying the parameter values in this range from physical reasoning. They suggested, on the basis of the Froude number defined by $(q/h_5)^2/(g'h_5)$ being necessarily subcritical (< 1), that a finite amount of mixing would exist in the limit height ratio equal to zero. From their analysis, they suggested that this limit would be about 0.1. This would correspond to $U_1/(g'h_1)^{1/2} = 0.3$. Though extrapolation of Fig 5.3 was difficult and somewhat suspicious, an ultimate upper limit of the dimensionless mixing rate slope, from this analysis, should be about four to five.

Our data, plotted in Fig 3.5, also suggested this kind of lower limit, though the data here predicted a value somewhat larger. In the case of an inviscid front, the lower limit of the densimetric Froude number would impose an upper limit on the slope of the dimensionless mixing rate line (as seen in Fig 3.6 and argued above). Again, this type of behavior was suggested in the large scale range of experimental data. The theory that was derived in Chapter 4, and which will be verified below in Chapter 6, also showed the presence of a lower limit to the Froude number (however, here the Froude number was defined by $U_1/(g'h_4)^{1/2}$, the differences being meaningless in the case of this analysis). This resulted in the collapse of large range of Froude numbers (for nearly inviscid fronts) on one slope of the dimensionless mixing rate graph. All of the above evidence suggested that the limiting Froude number was somewhere near the largest Froude numbers seen in the experiments herein. Further, the largest slopes seen in the data herein would be the limiting case for inviscid, deeply submerged, steady-state saline gravity current fronts. As was mentioned before, with the approximation of fine sediment, this limiting case would describe a large range of oceanic turbidity currents. From the data it was found that this limiting case yielded a rather simple result for the description of dimensionless mixing in terms of the height ratio

$$\frac{g'q}{U_1^3} = 3\frac{h_5}{h_1} \tag{5.4.3}$$

where h_5 is defined by the visible height of the current behind the head, however the differences between this definition of the current height and the point of zero velocity are not that substantial (see Fig 5.1). The constant, represented by 3 in (5.4.3), could be taken to be slightly larger (more like 4 or 5) if the limiting Froude number was somewhat smaller than what was extrapolated from the data here. Environmental density currents, however, rarely have height ratios less than 0.01 (usually turbidity currents are 0.05-0.10, García, 1992) which falls well within the range explored

in this study. Also, the Reynolds number (Re_q) would be somewhat significant in (5.4.2), even for values of 10^6, typical of gravity currents in nature. Both of these constraints force the parameter P to be somewhat larger than the limit of 0.3, and more like 0.5 or 0.6. This type of behavior and extrapolation of (5.4.2) to such limits should be viewed, however, with extreme caution. Despite this, additional support for use of (5.4.3) for environmental flows was shared by the limiting effect of scale seen the observations here (see Fig 3.6) and in the analysis of Chapters 4 and 6, where, for a wide range of Froude numbers, inviscid fronts appeared to be described well by (5.4.3). Remember, Froude similarity of environmental fronts was already insured by Keulegan (1958), and validated with comparisons of the data here to BS. Therefore, a complete characterization of environmental gravity fronts can be made using the simple relation above and the plots of Froude number from the experiments here and those of BS.

5.5 Effects of Boundary Condition

Effects of boundary condition, whether no-slip was enforced or not, were thought to be of importance when the study was originally undertaken. But as can be seen in Fig 3.10, the effects of the boundary condition were fairly small when the dimensionless parameter combinations are compared for a given scale. A theory explaining this can be found in the mean internal flow structure analysis of Chapter 6. The only difference between Equation 2.9a of BS and (4.2.18a) here was the slight alteration of the distribution of momentum in underflow. When the analysis was originally done, this change was assumed to be small for the sake of simplicity (*i.e.*, the ability to use Equation 2.9a without having to derive a new formula). Therefore, the theoretical equation of BS was solved using the approximations about the shape used in Chapter 4 for the physically realizable range of parameters. After going back to the theory and modifying it to account for the change in the distribution of momentum in the underflow, the physically realizable space of parameter values was recalculated. It was found, as stated in Chapter 4, that the change in the results was extremely small. If the change in boundary condition can be assumed to only affect the velocity profile, the slight modification of the momentum distribution in the underflow can be shown to be analogous to the change in boundary condition. This property was reflected in the comparison of the theory (the modification of momentum in the underflow) to the empirical results of Fig 3.10. Both the theory and the experimental data exhibited only small differences between the two situations (moving and fixed boundary conditions) for small (< 0.25) values of the dimensionless mixing rate, while at larger dimensionless mixing rates the difference was somewhat significant (10-20%). In conclusion, it seems that the change in bed boundary condition can be modeled as a modification in the momentum of the underflow, in which case, the differences in

bulk flow parameters for various bed boundary conditions are small for smaller height ratio experiments.

Other qualitative differences in the two boundary conditions were not so subtle. The billows which formed on the top of the fronts and which were responsible for a large portion of the total mixing forced the propagation velocity to oscillate. The propagation velocity data of Keulegan (1958) exhibited this sort of pattern, however, he attributed the oscillations to the surges in the main body of the fluid. In the experiments herein, the oscillations were somehow related to both types of mixing observed (which will be elaborated upon in Chapter 6) and their time scale was fairly large (as large as or larger than the integral time scale of the billows themselves). The point of this discussion is, however, to focus on the differences in the boundary conditions with respect to these oscillations. It seemed that the oscillations were changes in the distribution (between potential and kinetic) of energy at the front. The total amount of energy, however, remained constant. Therefore, after a large mixing event (*i.e.*, a large billow peeled off and/or a large frontal movement passed), the front had, on the whole, lost some potential energy. To compensate for this, some of the energy available was transferred from kinetic to potential energy, and therefore, the front lost some momentum and the propagation velocity decreased somewhat. As the potential energy was built up again with the temporary lack of mixing (which occurred because the front shrank as result of the loss of fluid from before), the kinetic energy strengthened (*i.e.*, the front speed up) and the cycle continued.

When the front was stopped on the belt, there was nothing to inhibit these oscillations. However, when the front was stopped at the toe of the belt an interesting phenomenon seemed to occur. The reasons for this phenomenon are graphically illustrated in Fig 5.4. As the front propagated down the channel before reaching the belt, it propagated over a fixed (in the laboratory frame) bed. Here, a well developed boundary layer in the clear water made the current much like a salt wedge. This type of behavior was similarly described by BS. In this regime, the front (or wedge) had little to no mixing with the overbearing clear water due to boundary layer in the clear flow. This also meant that energy losses were small in this regime. Therefore, a small potential energy input (supplied by the buoyancy flux) was required to force the front to propagate further downstream. This occurred until the front encountered the belt. At this point an extra amount of energy was required, not only to push the front further downstream, but also to overcome the additional mixing that was certain to take place as a result of density current behavior. Once on the belt, the potential energy again, like in the fixed bed portion, was directly proportional to the position where the front was located. Therefore a plot can be made, as in Fig 5.4, of the potential energy required to arrest the front in a particular position for a given experimental setup. The behavior shown in the figure resembles a plot of temperature versus energy input for a substance undergoing a phase transition (*e.g.*, ice to liquid water). This behavior is typically referred to as a

hysteresis and can be exploited for certain properties. One of these properties is stability. Because the oscillations in potential energy are bound to occur as result of billowing and other resonant phenomena discussed above, these small changes are not enough to perturb the position of the front in the streamwise direction when it is stopped at the toe of the belt. This, however, will not be the case when the front is stopped on top of the belt. Here, small changes in potential energy are directly related to changes in streamwise position of the front. An interesting thing to note was that the fronts at the upper end (near density current behavior) of the hysteresis were nearly identical to the pure density current case. However, unlike in the fixed bed experiments, in this region the oscillations in the distribution of energy did not alter the position of the front. For this reason, most of the later experiments (*e.g.*, areal LIF, *etc.*) that required absolute stillness focused on situations where scale effects were minimized by high dimensional mixing rates (high Re_q) and approximate similar behavior of no-slip/fixed bed experiments for moving bed experiments (*i.e.*, experiments conducted at the toe of the belt) was achieved.

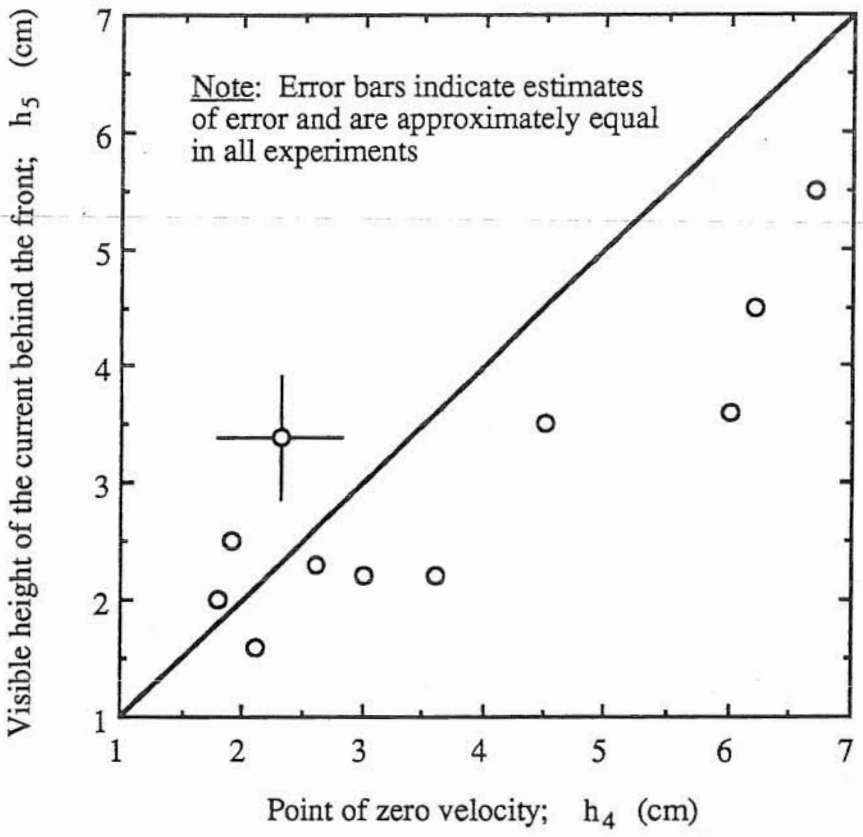

Figure 5.1 Relation between the two definitions of the interface between underflow and overflow with error bars.

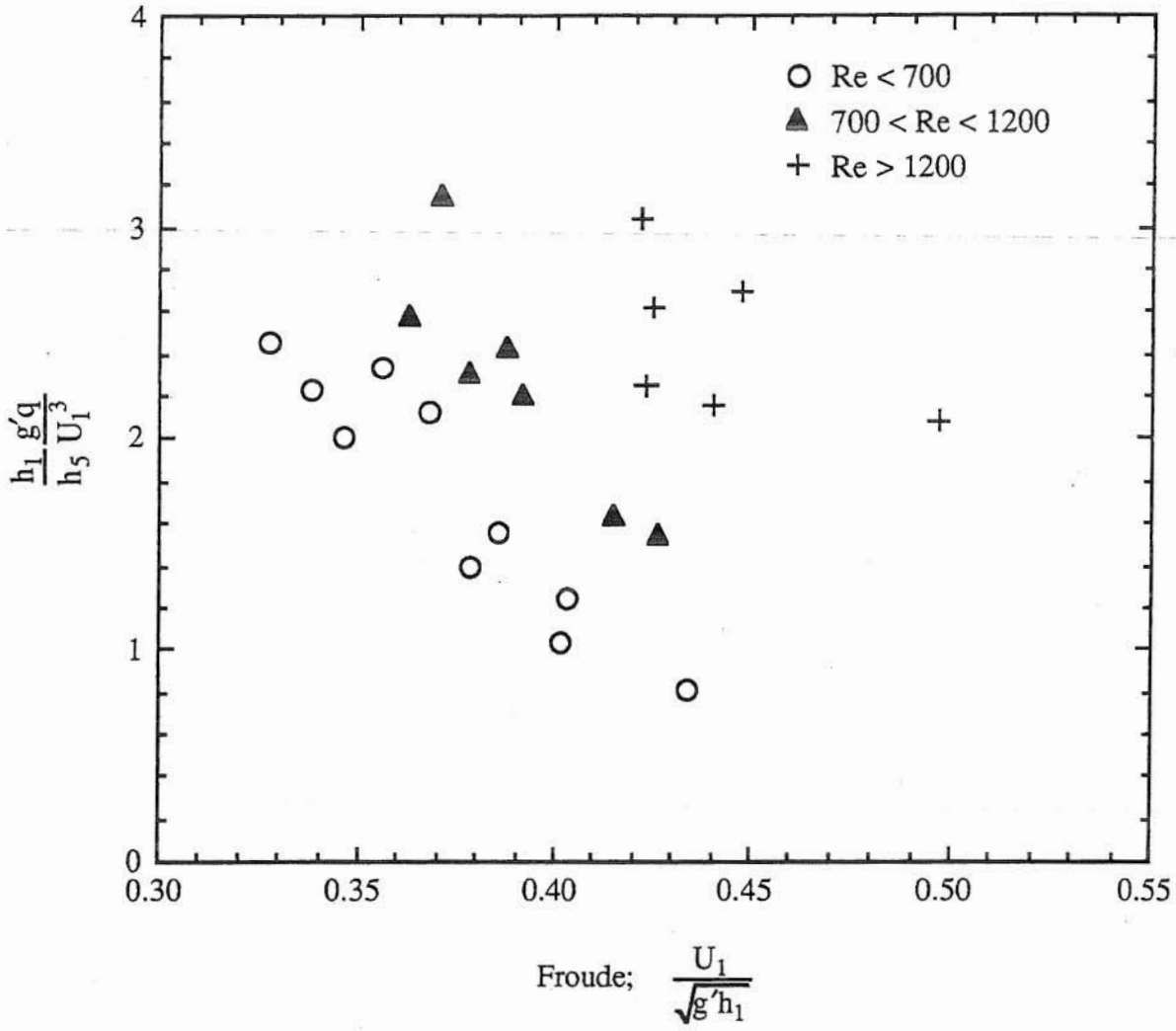

Figure 5.2 Effect of mixing Reynolds number on the relationship between the densimetric Froude number and slope of the dimensionless mixing rate line

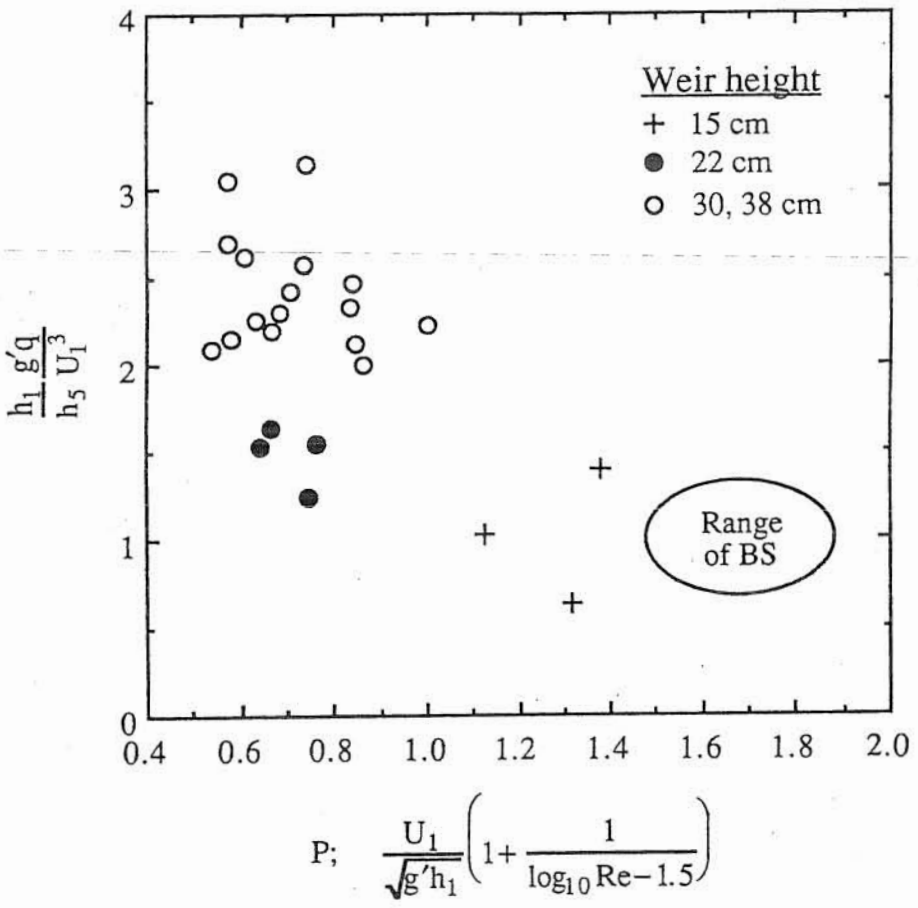

Figure 5.3 Attempt at collapse of the four important parameters with manipulation of viscous effects

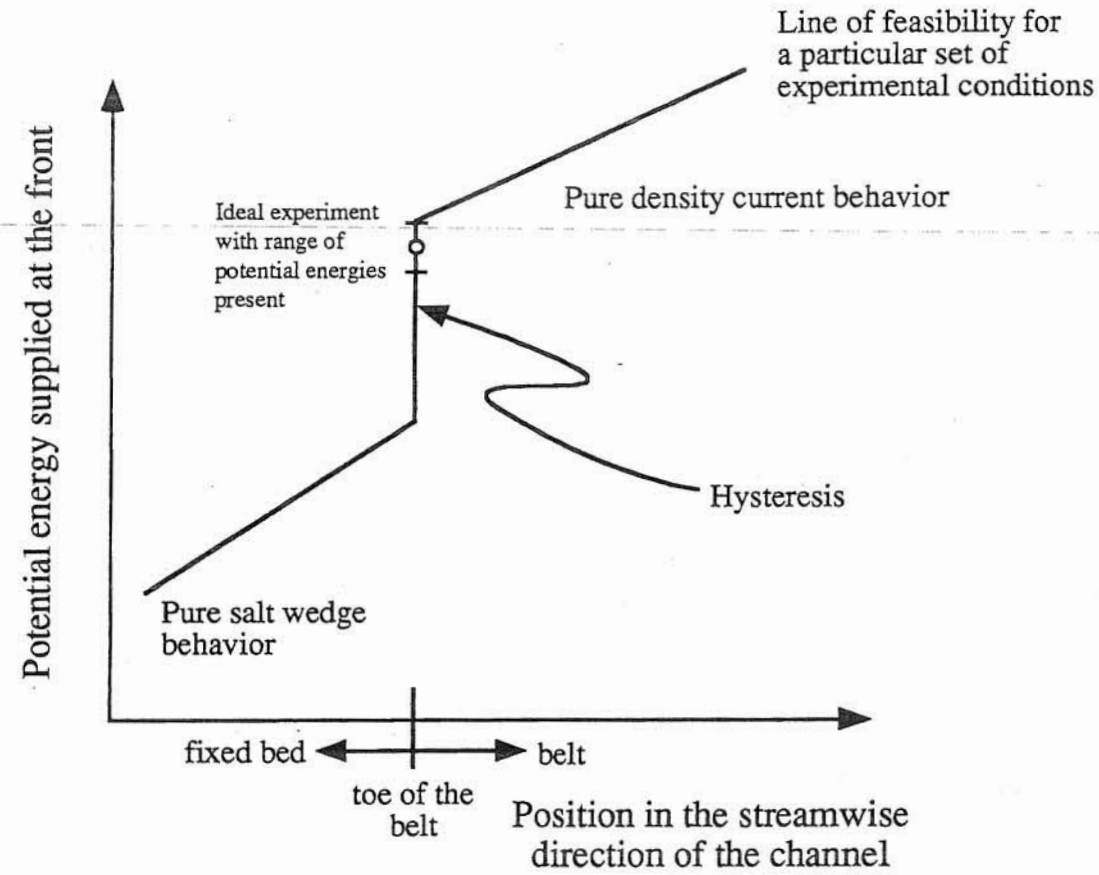

* Note that the curves representing pure salt wedge and density current behavior are both arbitrary and not necessarily linear

Figure 5.4 Representation of hysteresis in potential energy supplied to the front with respect to streamwise front position

6. ANALYSIS OF INTERNAL STRUCTURE EXPERIMENTS

6.1 Generalities

The effects of scale mentioned in the previous chapter were thought to have been a result of changes in the internal structure of the fronts. From early analysis of the profile results, it was found that this was indeed the case. The theory of Benjamin (1968) was then altered, as in Chapter 4, to accommodate these differences. The thrust of the experiments relating to the profiles was to ascertain the particular shape of both the mean velocity and concentration profile for large-scale (high Re_q) flows. Matching the profile results to the bulk flow results produced independently for each experiment using theory was another goal of the experiments herein. The results, as shown in many of the figures of Chapter 4, exhibit relatively good matching of profile and bulk flow results.

Previously, all of the work was based upon duplication and comparison to earlier experiments. In this chapter, the new techniques employed here will attempt to extract new information about the turbulent and spatial structure of saline gravity current fronts. First, all of the profiles (described above in Chapter 4) were examined for higher order statistical properties. Also, the LIF tapes were replayed and examined, with the areal techniques outlined in Chapter 4, qualitatively for spatial characteristics. Interesting phenomena were observed for a range of flow conditions which seemed to validate the comments on scale effects on the dimensionless mixing rate. These early flow visualization experiments were indicators for the type of research that could be performed in the future. Characteristics of the billows were quite clear and the differences were quite dramatic between different scale fronts.

6.2 Comparison to Previous Work and Experimental Technique Effects

The first question about the shape factors was why, even for the smaller flows, did they vary systematically from those found in BS. After careful consideration, it was discovered that the two measuring devices used (hot-film anemometry in BS, ADV here) each had their own problems. These difficulties tended to create opposite effects, possibly amplifying the differences in the shape of the velocity profiles. In the case of BS, the procedure used to determine the velocity profile accentuated the strong gradient of velocity in the vertical that defines the underflow-overflow interface. Also, the hot-film, because it measured a kind of weighted modulus of absolute velocity rather than distinct velocity components, tended to over exaggerate small streamwise velocity components near that interface. In addition, the hot-film could not sense flow reversal and therefore could not tell the sign of the velocity. This could play havoc with the highly

turbulent, low mean velocity measurements near the interface, further accentuating it. A hot-film, at the very least, would not be the best measurement tool for the flows described herein. However, in defense of BS, the technology employed here did not exist at the time of their experiments.

In contrast to the errors incurred in using a hot-film probe, the errors of this study might have damped the sharpness of the interface. This was because the profiles obtained herein were essentially spatially, low-pass filtered, as a result of the large sampling volume of the ADV. BS predicted that the most dramatic change in velocity (or inflection point) would occur at the underflow-overflow interface. This interface, from the mathematical definition of a Kelvin-Helmholtz instability, should not contain the profile inflection point, but it (the inflection point) should occur somewhere in the overflow. In the profiles measured and modeled here, this point typically occurred one-third to one-half the height of the overflow above the interface. In this region the effects of the smearing due to the consequential filter could be significant in the smaller experiments here. However, in the most important region of the profile, at the underflow-overflow interface, the smearing effects in the larger fronts were most likely negligible. Also, the basic character of the profile (polynomial versus power) should not be affected adversely, regardless of minor smearing at the inflection point. Also, in all of the runs the spacing of the data points was always several times larger than the measuring volume. Another testament to the process was that profiles were similar for a wide range of front scales. If smearing was a problem, peculiar scale effects would be observed as result of the shrinking effect of the large control volume.

The concentration profiles found with an LIF technique (Fig 4.19) seemed to reproduce the profiles by BS. This was to be expected because the primary influences on the concentration profile are gravitational effects, which were already in a regime of similar behavior (Keulegan, 1958). The power law shape of the concentration profile predicted by BS for the overflow is well demonstrated in Fig 4.19. The power, however, appeared to be slightly smaller (3 or 4) than that found in BS (4 or 5). The difference however, was small, not only with respect to theory of (4.2.18a), but also with respect to the actual differences in concentration observed. The differences were well within the errors of both experiments.

One interesting characteristic of the LIF concentration profiles, was a slight (about 10%) decrease in concentration as the bed was approached (within 1 cm). This was very unusual and was not predicted or mentioned in BS. Lock-exchange experiments have been seen to exhibit this type of behavior as result of the no-slip condition at the bed. The mixing associated with this type of phenomena was discussed at length in the previous chapter and shown to be negligible to the first order. Here, however, the mixing underneath could have manifested itself without the no-slip forcing. The reason for the mixing underneath the front, as mentioned previously, was an

elevation of the stagnation point (point O in Fig 4.1), also referred to as the nose height, h_n. In the all of the experiments that were compared to the theory of (4.2.18a), the fronts were stopped at the toe of the belt. As mentioned previously, this situation created a moving bed boundary condition. According to physical reasoning of the author, BS and others, this would result in a stagnation point at the bed (as in Fig 4.1). However, it may have been that the stagnation point was not on the bed because the moving bed was slower than the fluid in the underflow. In the experiments herein, particularly the higher mixing rate experiments, this would have been more dramatic. Also, the fronts examined here were quite large compared to the resolution of the LIF measurements. It could be possible that BS may have had the same behavior, but because their length scales were on the order of 5-10 times smaller, they could not have resolved such a small anomaly. The height of the nose here (if it was assumed to be located at the smallest height where constant concentration still exists) was consistent with the 10-20% of h_f which was found by Keulegan (1958) and confirmed by Simpson and Britter (1979) for fixed bed experiments. Though the nose was not apparent from viewing the front, a finite-height, stagnation point looked possible from some of the qualitative areal analyses of the billows (shown below). It was also possible that the slight decrease in concentration is the attenuation of the laser due to saturation by the fluorescein, as in (4.4.1). This was unlikely, however, because some other experiments, not explicitly shown here, exhibited these same patterns for integral concentrations much smaller than (orders of magnitude) the point of saturation discussed in Section 4.4. Extremely near the bed the concentration estimated was artificially high because of reflection off of the bed, however, the region over which this occurs was on the order of 1 mm (2-5 pixels).

6.3 Profile and Integral (Shape) Factors

Extensive analysis of (4.2.18a) yielded some insight of the importance of each of the shape factors. From this analysis, the most important shape factors in this equation were found to be δ and β. The former, though it only appears in one term of the equation, strongly regulates the structure of the flow. This factor was found to be the integral of the square of the dimensionless velocity over the entire height of the overflow. It can be thought of as the dimensionless flux of kinetic energy out of the control volume in the overflow region. Small changes in the shape, particularly near the overflow-underflow interface, of the profile produced relatively large changes in this parameter. And because the third term of (4.2.18a) was found to be predominate (which δ strongly regulates), δ seemed to play a major role in the overall characteristics of the front. When higher mixing rates were considered, where the buoyancy terms become less important, the importance of δ increased. It then became a kind of drag coefficient (the ratio of two velocities squared), like in the case of a wall-bounded jet.

However, probably the most important parameter was found to be β, which could be thought of as the dimensionless representation of the flux of contaminant out of the control volume in the overflow region. As was shown in (4.2.3) from conservation of mass, β is the constant of proportionality between the product of the maximum velocity in the overflow (U_2) and the height of the overflow (h_3) and the mixing rate. As U_2 was fairly constant in the experiments and largely dominated by the propagation velocity (U_1), it was found that β was the only parameter that regulated the size of the front (dominated by h_3) and the mixing rate. This importance was also glaringly obvious from manipulation of (4.2.18a) with respect to various values of β. The most important term of (4.2.18a), as mentioned above, was calculated to be the third term and β is also an important part of it, both by itself and as a part of a ratio with α. Beta was also found to be highly dependent on the shape of the concentration and velocity profile near the overflow-underflow interface. The integrand of the integral that defines β was typically zero for most of the height above the overflow (h_3), except in this region. This would suggest, as mentioned above, that this region heavily regulated the dynamics of the flow. A possible reason for this was that the region was the place where the billows and the internal waves on the interface of the current interacted. This interaction, as will be discussed below, had much to do with the stability of a given front, not to mention regulation of the dimensionless mixing rate.

The ratio, β/α, was also found to be a very important term. It manifests itself in different combinations of the compressed variables; B, x, and ψ. This ratio could be thought of as a mixing efficiency. The parameter, β, as mentioned above, was symbolic of the flux of concentration out of the front via the overflow. Alpha, though not significant on its own, was demonstrative of the total flux of fluid out of the front via the overflow. The maximum of this ratio was found to be 1 (where the concentration in the overflow is constant, positive and equal to the concentration in the underflow). The minimum of this ratio, on the other hand, was zero, in the case where no concentration exited the overflow. For the generalized theory, this efficiency varied depending on the situation (the set of parameters). In BS, it was constant and equal to 0.11. For the theory here, this ratio (as can be derived from Table 6.1) was typically on the order of 10%. Beta and α varied the most with scale, as opposed to the other parameters. This made sense because they dealt with the combination of inertial and buoyancy distributions. Their ease of representation as a mixing efficiency also made them a candidate for change as the dimensionless mixing rate changes.

The other terms (γ and ε) related only to the distribution of concentration in the vertical. These parameters were found to be strongly dependent on the gravitational (or Froude) effects. Effects such as these were already taken into account by BS and their measurement techniques of concentration were as good as, if not better than, the ones employed here. Therefore, little difference was expected in the values calculated here and the ones found earlier by BS. The results

of Table 6.1, a table of typical experimental values of all the shape factors, show that this was indeed the case. The results shown were found from numerical integration on the experimental profiles. These values were virtually the same as can be found from the equations of (4.2.18a), where $\xi = -1$, the typical value found in the experiments herein.

6.4 Performance and Accuracy of Proposed Model

The accuracy of the model (presented as (4.2.18a)) is best illustrated in Figs 4.13 and 4.14. In these plots, the physically realizable solution to the equation is plotted along with the data found in this study. There are other solution sets to (4.2.18a), however, this was the only set that occurred in the physically realizable range outlined in BS. This range was also discussed in Chapter 5. Most of the other real solutions did not occur in the first quadrant of three-dimensional space defined by the Froude number, the dimensionless mixing rate and the height ratio. All of these variables were necessarily non-negative, and therefore their physically realizable solution set necessarily occurred in the first quadrant. Other solutions in this set did occur, but only for outrageous (over 10), unrealizable values of the Froude number. Therefore, the model, in this case, was solved in the general sense (no information was necessary about the velocity profile, *i.e.*, the velocity shape factors were determined by the mixing rate). Other solutions, where empirical velocity information was input into the solution, will be discussed below.

Though agreement to the data was fairly good, it should be noted that the model assumed completely inviscid behavior. This was most likely not the case for all of the experiments, however. Fully turbulent behavior was probably only attained for the highest dimesionless mixing rate, largest scale experiments. Therefore, small errors in the estimation of dimensionless mixing rate were most likely due to both the effect of lack of fully similar behavior and experimental error. Because the similarity limit appeared to be so close to the limit of the facility, it was difficult to specify any such criterion and throw away the appropriate fronts. Even the notion of an absolute inviscid limit should be viewed with some skepticism because of the dependence of that limit on densimetric Froude number (as shown in Chapter 5).

The model of Benjamin (1968), and (4.2.18a) here, however, accurately described the way the three important parameters (Froude, dimensionless mixing, height ratio) varied with one another with little empirical input. Probably the best testament to the model was the verification of (3.2.6). This equation indicated that an inviscid model would necessarily have to produce a linear relationship between dimensionless mixing rate and height ratio for a fixed Froude number. As mentioned previously, Fig 4.12 demonstrates the solution of (4.2.18a) and this linearity for most of the experimental range. Deviations from this linear relationship did occur at extremely low dimensionless mixing rates (< 0.1), however. This type of flow would be extremely difficult to

produce and measure in the lab and even then would most likely be dominated by viscous effects (low Re_q). In nature, this type of phenomena would probably be better modeled with the saline wedge equations of Arita and Jirka (1987), where mixing can be ignored and the equations are more closely tied to theory. This type of problem (saline wedges) has been studied more extensively because of the ease of experimentation (no conveyor belt is needed to arrest the head). Also, saline fronts with dimensionless mixing rates as low as 0.05 appeared, from qualitative experimental observations, similar to saline wedges, characteristic of virtually no billow activity. In the fully developed turbulent, natural scale case, the nibbling phenomena (described more thoroughly below) would most likely dominate in these type of flows.

The model equation (4.2.18a) assumed that the velocity profile could accurately predict bulk flow dimensionless parameters and vice versa. The intermediary between these two was the parameter, ξ. And though the shape factors could have been accurately predicted if (4.2.13) was used to predict them (*i.e.*, using some bulk flow information about each particular front), they were not well predicted from the general solution of (4.2.18a). Deviations from the general theory in the bulk flow dimensionless parameters were lessened if the empirical value of ξ was used as a constant in (4.2.18a). In other words, if the velocity profile was known *a priori*, the dimensionless parameters (dimensionless mixing rate, *etc.*) were predicted much better than if the general theory was used. Typically, ξ ranged around -1 in the experiments (found from an experimental fit of the profile or solution of (4.2.13) with bulk flow parameters), while the general theory predicted values between 0.5 and -1, given a set of dimensionless parameters. The improvement in the prediction was not that substantial, however. The improved data fit lent more support to the link between the dimensionless parameters and the velocity profile shape given in (4.2.13). And because the improvement was not substantial, this indicated that the assumptions of the general theory were not that poor. And for the basics of the asymptotic analysis below, these assumptions should be adequate.

With the model equation verified, one could look at the limits and behavior of (4.2.18a). For the purposes of the discussion here, only the limits that appealed to physically realizable fronts in nature or in the laboratory will be discussed. The first of these limits was the limit of low height ratio. This limit was discussed at great length by BS. Despite the fact that their theory proved to be slightly in error by the study here, the problems in their theory became negligible in this asymptote. Proof of this was their conclusion that as height ratio goes to zero the front can be described by

$$\frac{U_1^2}{g'(h_4 + \gamma h_3)} = 2 \qquad (6.4.1)$$

where g' is reduced gravitational acceleration, U_1 is the oncoming flow velocity, h_4 is the height of the underflow, h_3 is the height of the overflow and γ is a shape factor dealing with only concentration, defined in (4.2.18b). A conclusion similar to this can be made from the theory formulated here. It seemed that at extremely small height ratios, the mixing rate was not zero, but some small value (< 0.1). This small value can be related to the Froude number. The formulation above, (6.4.1), can be derived identically from a physical analysis, that BS mentions, which was independent of the particular theory, where γ is just a representation of the stratification. This derivation was more physically based and relied on the assumption that flow velocities high in the water column will not be affected by the front. BS later concluded that for their assumed shape, the maximum that the dimensionless mixing rate could be attained for $h_4/h_1 \rightarrow 0$ was 0.089. The maximum mixing rate using the velocity profile shape here was about 0.07. This idea of maximum dimensionless mixing as $h_4/h_1 \rightarrow 0$ was in fact another argument for a limiting Froude number. As can be seen in Fig 4.14, the intercept (the dimensionless mixing rate at height ratio equal to zero) increased steadily for increasing Froude. Above f = 3.5, the dimensionless mixing rate for zero height ratio was above this theoretical maximum, and if the theory holds, this Froude number, and the corresponding fronts, would not be physically realizable (*i.e.*, an unrealizable dimensionless mixing rate would result).

In the opposite case (large height ratio, which in this limit also corresponds to high dimensionless mixing rate), the theory seemed to have solutions for sets of parameters where the dimensionless mixing rate was arbitrarily high. Dimensionless mixing rates above 0.3, however, were not observed in the experiments here. This maximum value agreed roughly with the experiments of BS. This limit could be an artifact of the experimental device, however, it was felt that this limit was most likely a result of an unknown instability which caused the front to short-circuit over the weir. As a result, large height ratios were unattainable. Benjamin (1968) presented a quite lengthy discussion of the upper limit of height ratio. The discussion ended with a conclusion that the absolute limit on the height ratio was 0.5, but that the function that described the zero mixing case had an unrealizable solution (*e.g.*, net energy gain for increasing front height) for height ratios greater than 0.347. However, neither of these limits seemed to be even close to possible (the largest height ratio produced here was about 0.1) because of the stability problems mentioned above.

The most important limiting situation, however, was not the result of taking any one of the parameters to the extreme, but rather looking at the behavior of the function for a large range of commonly found Froude values. The Froude number, as seen in Fig 3.5 did not vary much throughout the entire range of the experiments presented here. In fact, many early works, mentioned in Benjamin (1968), suggested that it was constant for all fronts. Benjamin (1968) and others (Middleton, 1966) showed this not to be the case, however, they did show that Froude

number would most likely be found for a wide range of flows in the slightly supercritical region ($2 < f = U_1^2/g'h_4 < 4$). In Fig 4.12 it can be seen that the slope of dimensionless mixing rate line, previously proved to be linear for density currents, is approximately 2.5 to 3 for the entire range of physically realizable Froude numbers. Most of these lines of 'isoFroude number' also had an intercept at or near the origin. If we assume that the differences in current height definition (*i.e.*, the difference between h_4 and h_5) are small, for a large range of inviscid density currents, it can be mathematically stated

$$\frac{g'q}{U_1^3} = 3\frac{h_5}{h_1} \tag{6.4.2}$$

which is identical to (5.4.3). This reinforced the idea of a simple relationship between the dimensionless mixing rate and the height ratio for most large scale (virtually inviscid, slightly supercritical) environmental flows.

6.5 Turbulent Characteristic Profiles

It should first be noted that the turbulence measurements were made with devices not specifically designed for such kind of data acquisition. The ADV used was designed only to give reliable mean data. Real-time measurement of the velocity was not one of the manufacturers main goals. However, they did considerable work with establishing the extent of the acoustic noise in the signal (personal communication, Atle Lohrmann). According to them, the acoustic noise for signals typically seen in the experiments should be on the order of 1%. This was considerably smaller (by an order of magnitude) than the turbulent fluctuations generated by the walls (about 10%) and much smaller (50%) than the fluctuations generated inside the fronts.

Before the ADV was implemented (except for a few ignorant trials; EXP30, EXP34, EXP37) in the channel, it was tested without the belt moving and without a front. The resulting flow is a kind of narrow open-channel flow. Results compared reasonably with accepted limits. As was mentioned earlier in Chapter 4, the probe did have noise difficulties early in the experiments at a certain height (discovered in the process of the verification run). This problem was quickly rectified with an updated version of the acquisition software. However, there was no precedent that could be used to verify the velocities in the front (with varying degrees of salinity and high turbulent energy). On the other hand, there was no device, except for this one, that has the capability of even hoping to capture turbulence in this type of environment.

The turbulent kinetic energy (TKE) profiles obtained with the ADV were then analyzed. The pattern illustrated in Fig 4.15 is common to the other profile experiments at different scales

(represented by different weir heights). To elaborate, at low mixing rates, and thus low height ratios for a given weir height, the profile of TKE is bimodal. In other words, there are two peaks in the vertical distribution of the turbulent energy. The lower peak seemed to correspond to the interface of the underflow and overflow. In lower-mixing-rate experiments (which typically corresponds to higher Froude numbers), the interface was distinct and easily visible. Internal waves on the interface propagated in regular patterns. This appeared in the profile as a peak in the energy. The top peak occurred somewhat in the middle of the overflow. The upper peak was due to the turbulent energy relating to the billows. TKE in the overflow was typically distributed in a triangular fashion, culminating at this peak. The overflow peak was several times as great as the interfacial peak. As mixing rate and relative front size increased the billow TKE peak increased (even in a dimensionless sense) while the interfacial peak seemed to disappear. Once a certain point was reached, the dimensionless values of the peak decreased for increasing dimensionless size. The peak also became rounded and parabolic. This pattern continued for all of the weir heights studied and the general profile shape (corresponding to a given dimensionless size) was absolutely repeatable.

As described previously in Chapter 5, some fronts appeared to be more stable and easier to arrest. These highly stable fronts had high dimensionless (with respect to the mean flow kinetic energy, U_1^2) turbulent kinetic energy (TKE) peaks. The TKE profiles were triangular and fairly symmetric in the overflow about this peak. These fronts fell somewhere in the middle of the experimental range in terms of the dimensionless mixing rate.

As mentioned above, the ADV also produced consistent autocorrelations. This tool of turbulence measurement gave indications as to the dominant frequencies in the flow. Though its companion in the frequency domain, the power spectra, could have yielded this frequency more precisely, it was unable to be used because of the problems mentioned above. The autocorrelations exhibited periodic behavior with a dominant frequency ranging from about 1 Hz in the lower mixing rate experiments to 0.25 Hz in the highest dimensionless mixing rate experiments. Vertical velocity correlations illustrated these frequencies much clearer because they were not 'polluted' with the other scales, as was the case in the streamwise direction. The billows primarily acted in the vertical and a truer measurement of their mixing capability was demonstrated in this type of correlation. However, they too have some additional frequencies superimposed on them. These foreign frequencies could have been due to the frequency of the internal waves on the interface of the current behind the front or smaller billow frequencies. Though it seemed that Fig 4.16 (high mixing) had as clear a correlation as Fig 4.18 (moderate mixing), Fig 6.1 shows how pure an autocorrelation can be for moderate mixing, high TKE-peaked front, if the data can be acquired for an adequately long record. Fig 6.1 was taken from the velocity record used for the calibration of mean velocity of the probe (seen in Fig 4.6) inside the front. This record is 150 sec long and taken

at the peak in TKE of a moderate mixing front. Fig 6.1 shows that a velocity record obtained inside a stable (moderate mixing, high TKE-peaked) front was dominated by a small range of small (order one or smaller) frequencies. Inaccuracy in placing the probe at the true peak and shortness of record all plagued the autocorrelations of Figs 4.16, 4.17 and 4.18. All of these problems were eliminated in the calibration run because the velocity structure was not desired. Again, it is important to remember that the fronts, due to pollution of the overbearing clear water, could be run for 10-15 minutes. Therefore, sampling many points for long periods of time was an impossibility. In the future, experiments will be more typical of the calibration (one point sampled for a long period of time) than the profile experiments elaborated upon herein.

6.6 Billow Development and Qualitative Mixing Processes

The colorful pictures of Figs 4.20 and 4.21 are not only pleasing to the reader, but illustrative as well. The differences between the relatively high Re_q (about 1000) front and the relatively low Re_q (about 200) front were quite dramatic. A further illustration of the internal concentration structure of a large scale billow is seen in Fig 6.2. This picture was extracted from the animation sequence described in Chapter 5. The animation sequence allowed for a clearer picture of the sites where the larger billow 'cascades' into smaller eddies. This type of behavior did not occur in the smaller scale front visualizations (*e.g.*, Fig 4.21). Locations of these cascading eddies are illustrated with arrows in Fig 6.2. Also significant activity occurred just behind the front (marked with a 1 in Fig 6.2). In the large scale experiments, like Fig 6.2, there was considerable mixing here. These small fingers of fluid leaving the back side of the billow have been shown to be common features in fully turbulent Kelvin-Helmholtz billows (Sullivan and List, 1994). Fingers like these were not visible in any of the smaller scale (small Re_q) billows. The absence of other size eddies indicated that little inertial transfer occurred in these experiments. This confirmed earlier conclusions about the lack of similar behavior (in which some region of inertial energy transfer must exist) in these experiments.

Nibbling was another mixing process that seemed to be an artifact of larger scale. Nibbling, as illustrated in Fig 4.20, was a frontal movement which transported dense fluid slowly and semi-periodically into the overflow between billow events. It could have been the result, or combination, of many different processes. First, it could have been simply the result of the transverse movement of billows moving in and out of the plane of the laser. The billowing events at larger scales were less stable in the lateral direction and did not roll off in uniform sheets, as in the experiments of BS. Instead, they ejected from the underflow in large, powerful bursts, limited in extent in the lateral dimension (*i.e.*, they were purely two dimensional). Therefore, at the edges (in the lateral or transverse direction) they may have appeared as frontal movements rather dramatic

ejections. Another possible origin of this behavior was from the internal waves on the underflow. The frequency of the internal waves was, from qualitative inspection, not equal and typically larger than that of the large billow events. The billow frequency (in the absence of other mixing phenomena) has an lower limit that can be obtained from an analysis of (5.3.1). Therefore, a resonant interaction between the internal waves and equilibrium-sized billows (both of which operated at different frequencies) could have existed. This resonant interaction could have been manifested in the dramatic billow ejections, while in between small billowing occurred and appeared as a frontal movement. Nibbling was also found behind the head. Mechanisms governing this type of mixing are more accurately described by the mixed layer literature and can probably be attributed to turbulent diffusion. Mixing behind the head, however, was insignificant compared to massive amounts of mixing found at the front. Also, even though the current was arrested at the toe of the belt, lobes and clefts (another venue for mixing) appeared. However, they were not as prominent as in the fixed bed experiments. Further discussion of lobes and clefts and their impacts on the mixing characteristics will be presented below.

The oscillations in kinetic and potential energy, as first described in Chapter 5, were also apparent from the videos of the fronts. This phenomenon was observed in the two-dimensional plane illuminated by the laser sheet. Occasionally a large mass of dense fluid would be mixed out of the front. After this time, the front was extremely diminished and only small portion of the underflow was observed. After more time, the front built itself up until another strong billow event. The process was not orderly and smaller billow events and frontal movements typically occurred in between these larger movements. Without the energy buffer generated at the toe of the belt and described in the previous chapter, these large billow events would drag the front back and forth along the top of the belt as the total energy of the front was transferred from kinetic to potential energy. These oscillations typically occurred on a time scale of a few seconds to a few minutes. In a traditional unsteady experiment (*i.e.*, a lock exchange experiment), these effects would be extremely difficult to realize. This is because the change in front velocity would be much smaller (on the order of a couple percent) than bulk or mean velocity. Also these changes would occur over a length of meters to hundreds of meters, smaller than most laboratory setups.

The assumption that the mixing underneath the front was entirely prevented by this setup (moving bed) was probably in error. This, however, was not a problem, but rather an advantage because the characteristics of real flows (most of which are no-slip or fixed bed) were studied in the more steady, stable environment at the toe of the belt. Proof of this was the slight decrease in the concentration as the bed was approached, as shown in Fig 4.13. Also, the lobe and cleft behavior, described earlier, indicated some extent of fixed bed behavior. Fixed bed experiments, as mentioned above in this chapter and in Chapters 5, however, were plagued with unsteadiness problems. Fluctuations due to the large billows were still accounted for (*i.e.*, in the measurement

of TKE, for which they were important) in the moving bed experiments because the front would shrink considerably in the vertical extent. However, these fluctuations were not enough to move the front permanently away the point of measurement, and thus lose the proper positioning of the probe within the front.

Table 6.1 Experimental mean values of shape factors found from numerical integration of profiles. These values are typical for moderate mixing (*e.g.*, EXP38), large scale experiments

Shape factor	Typical experimental value
α	0.58
β	0.04
δ	0.20
γ	0.44
ε	0.03

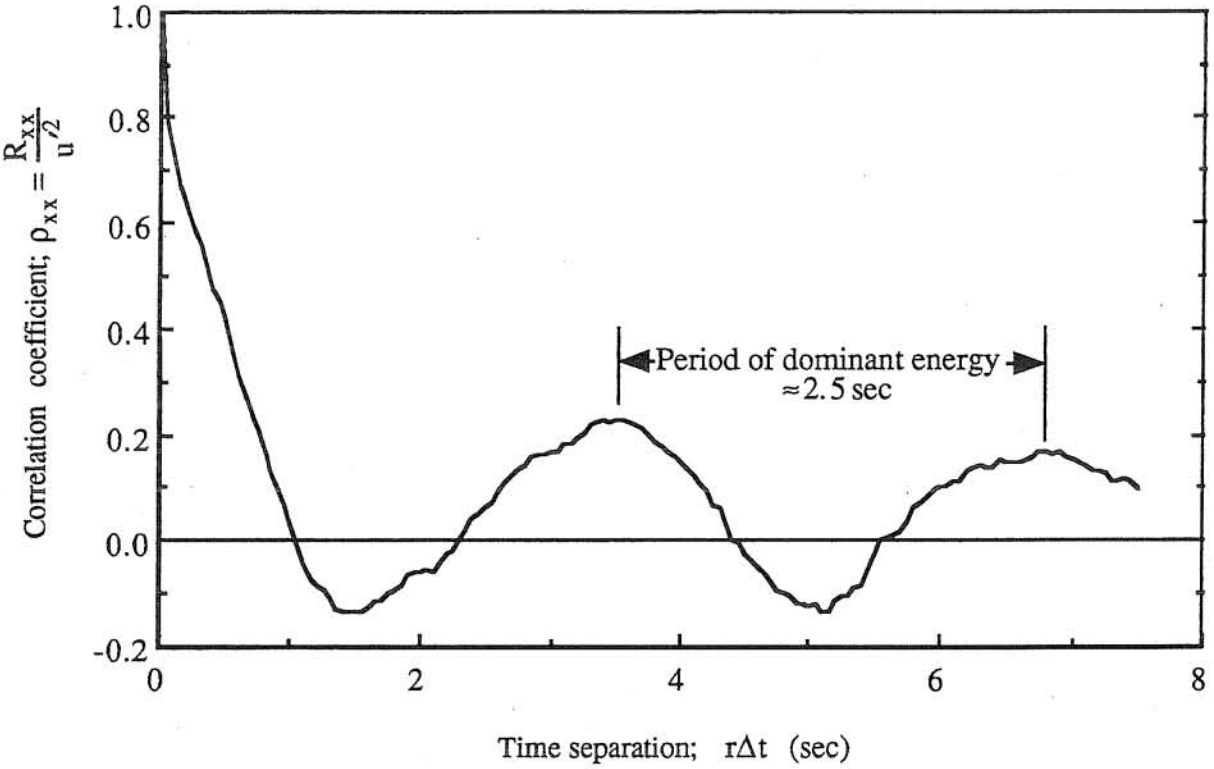

Figure 6.1 Streamwise autocorrelation of velocity record using a long record length (150 sec) in a moderate mixing rate front

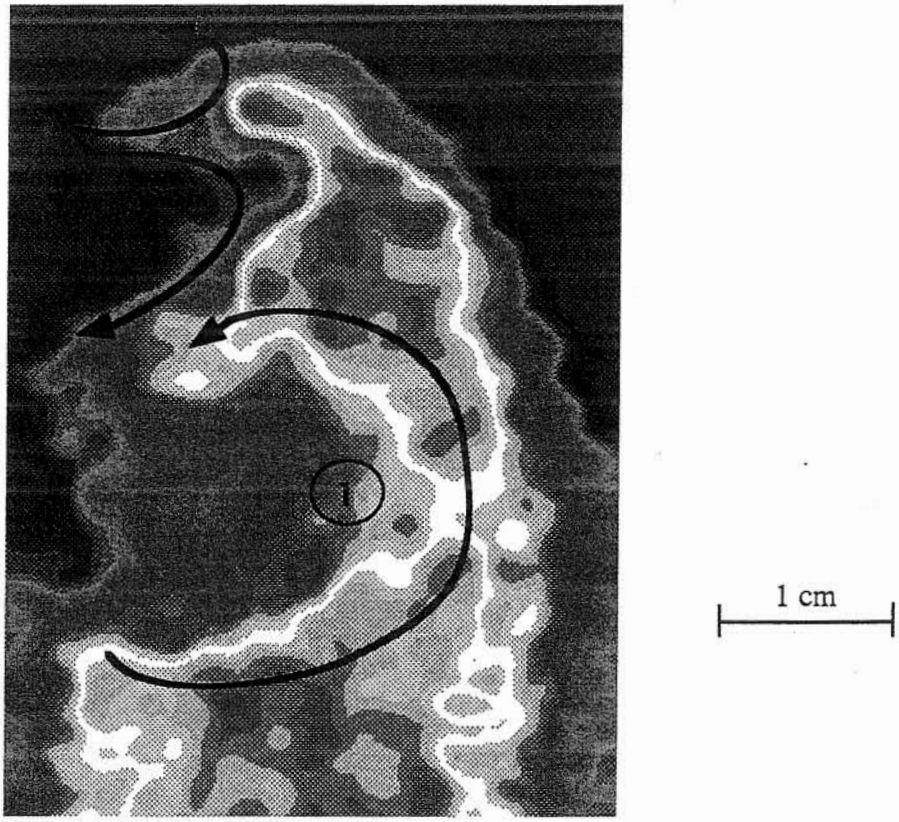

Figure 6.2 Internal structure of large scale billow

7. CONCLUSIONS AND FUTURE RESEARCH

7.1 Summary of Findings

In the course of the experiments presented above, many characteristics of saline gravity current fronts, previously undiscovered, were found. Most of these discoveries dealt with the effect of scale on the mixing phenomena of the fronts. Previously, dimensionless mixing was believed to be a relatively weak function of height ratio for physically realizable densimetric Froude numbers. However, the experiments performed herein found this was not the case. It was found that dimensionless mixing is only a weak function of height ratio for small, laboratory flows (*i.e.*, previous studies where the mixing Reynolds number, $Re_q < 200$), while for larger scale flows, the dimensionless mixing is more dependent on the height ratio. In the experiments herein, a large range of Froude and Reynolds numbers were explored. This allowed for trends in all of the dimensionless parameters to be realized more accurately. It was found that the nonlinear interaction between the densimetric Froude ($U_1/(g'h_1)^{1/2}$ or $U_1/(g'h_5)^{1/2}$) and Reynolds (q/ν) number was important in the assessment of these scale effects.

Increases in the scale of flows increased the effects of the height ratio on the dimensionless mixing rate. Fig 3.6 demonstrates this behavior quite dramatically. A limiting slope was also believed to exist because the data of the two of the largest scales (the 30 and 38 cm weir height experiments) collapsed onto virtually one line. This line had a slope of approximately three with an intercept of zero. Analysis was attempted to collapse both small and large scale data without much success. However, the idea of a limiting Froude number (argued a number of ways in Chapters 5 and 6) allowed for a simple result. The dimensionless analysis of Chapter 3, the limit of the experimental data, and the solution of the conservation equations of Benjamin (1968) all predicted that the dimensionless mixing rate would be proportional to the height ratio for large scale, inviscid fronts. From the considerable analysis, a simple mathematical expression results

$$\frac{g'q}{U_1^3} = 3\frac{h_5}{h_1} \tag{7.1.1}$$

where $g'q/U_1^3$ is the dimensionless mixing rate and h_5/h_1 is the height ratio. Though this equation was formulated previously in the text as (5.4.3) and (6.4.2), it is repeated here because of its significance. This equation was valid up to a dimensionless mixing rate of approximately 0.3, above which experiments showed that fronts were inherently unstable.

Mean internal flow structure experiments allowed for the theory of Benjamin (1968) and Britter and Simpson (1978), BS, to be modified to include the effects of scale on the fronts.

Because the scale effects did not alter the external densimetric Froude number, modifications in the velocity were expected to produce the scale effects (from a simple one-dimensional analysis of the flow). The resulting profiles exhibited differences not only in the important billow or overflow portion of the front, but in the underflow as well. The solution of the modified equations predicted increased dimensionless mixing rates (above those of BS) and increased dependence of the dimensionless mixing rate on the height ratio. Both of these theoretical results matched the data fairly well, considering that inviscid flow was probably an invalid assumption for some of the smaller scale flows. Impacts of boundary condition on the bulk flow dimensionless parameters were also investigated. It was shown that dimensionless mixing rates obeyed approximately the same behavior with respect to the height ratio, regardless of boundary condition.

Further studies investigated the internal dynamics and spatial structure of the fronts. Planar LIF experiments showed that low Re_q fronts, typical of BS, lacked the characteristics of turbulent billows present in the higher Re_q fronts here and in the turbulent mixing layers of Sullivan and List (1994). Also different modes of mixing were observed at these larger scales. This further reinforced the previous conclusions of increased dimensionless mixing with increased Re_q. Though the ADV was not designed specifically for turbulent data acquisition, information was derived about the bulk turbulence properties of the fronts. Turbulent kinetic energy (TKE) profiles were generated using the ADV. Autocorrelations of the velocity records allowed for the realization of dominant frequencies of the flow as well as identification of the stability properties. Simple qualitative energy relationships were found between the two competing forces in the fronts, the internal waves of the current and the Kelvin-Helmholtz billows.

7.2 Implications for Flows in Nature

Due to the highly inaccessible and unpredictable nature of density (in particular, turbidity) currents, data acquisition of the front characteristics of such flows has been extremely difficult. Some of the first attempts at measurement of turbidity currents were made on continuous flows, generated by the dumping of mine tailings, in Lake Superior (Normark and Dickson, 1976). In this case, no head or front was realized. However, a few recent attempts (*e.g.*, Inman et al, 1976 and Hay, 1987) focused on measuring bulk characteristics of the fronts and current bodies. These works, along with others, were summarized by García (1992). If typical values are used for the sake of example, water depths were on the order of 50 meters, current velocities were of about 1 m/s and turbidity current depths were on the order of 5 meters. Assuming that the observations made in the experiments apply for current in nature, the dimensionless mixing rate for density current fronts in continental shelves would be approximately equal to three times the ratio between

the current body height and the total water depth (h_5/h_1) according to (7.1.1). Thus the dimensionless mixing rate would be given by

$$\frac{g'q}{U_1^3} = 3\frac{h_5}{h_1} = 0.3 \qquad (7.2.1)$$

From the results presented in Chapter 3, Fig 3.5 gives $U_1/(g'h_5)^{1/2} = 1.3$. If a Galilean transformation is taken on the equations here, making $U_1 = U_f = 1$ m/s, reduction yields $g' = 0.12$ m/s^2 and $q = 2.5$ m^2/s. And the unknown in the example, the excess fractional density, would be approximately 1.2 %, which would be considered quite reasonable for the dilute currents studied here. It should be noted that in the natural, non-transformed case, the mixing rate per unit width and the flow rate in the underflow are not equal. Estimates of the current Reynolds number, q/v (where q here is the total flow rate per unit width, which is q, found from the mixing analysis, plus the height of the current multiplied by the flow velocity), would yield values on the order of 10^6 which are also representative of large scale gravity currents (Simpson, 1987).

7.3 Conductivity Probe and Future Comprehensive Turbulence Experiments

As was mentioned previously in Chapter 4, the ability to transfer the data acquired thus far to the frequency domain was plagued with problems. Aliasing, probably the biggest problem with the current data set, will be eliminated by using a high-resolution conductivity probe. The probe was purchased during the time of the writing of this thesis and the preliminary work was not included because of insufficient data and analysis. Specifications of the probe, outlined in the thesis of the manufacturer (Head, 1984), claim that a sampling rate of 800 Hz is possible. Preliminary data acquisition has only been able to sample at 300 Hz, mostly due to the inefficient software (written partially by the author) of the analog-to-digital converter. Even at this lower rate, most of the energy in the flow can be captured. However, considerable adjustments (*e.g.*, the addition of a low-pass filter to eliminate some high frequency electrical noise) need to be made before quality, spectral data can be extracted from the fronts. Confirmation of the hypotheses made in the LIF measurements will be the first test of the new technique. Validation of mean, and possibly turbulent profiles, will conducted before spectral information will be accepted. Then, the area of particular interest (the overflow region) will be studied at length. As was illustrated in Chapter 6 with the autocorrelations, record lengths should probably be on the order of minutes rather than seconds. Only then, will it be possible to process the data in such a way as to produce repeatable results in frequency space.

Once in the frequency domain, verifications can be made as how far apart the scales of the flow really are. In other words, whether any kind of inertial regime exists in the billow region for relatively moderate Re_q flows. It could be hypothesized that for even smaller flows (*e.g.*, BS-sized) no inertial regime would exist and merely a spike in the frequency domain would remain due to the frequency of the billows. A more important use of the frequency information would be the estimation of dissipation rates. Viscous dissipation is function of the integral of the energy spectrum and the kinematic viscosity. It is the only parameter needed in the turbulent energy budget (Tennekes and Lumley, 1972) that cannot be found from the measurements taken thus far. With this last term in the energy balance, a theory including the dynamics of the turbulent energy inside the front could be formulated, possibly explaining in a more quantitative way (rather than qualitatively as in Chapter 8) the stability of fronts for a given set of parameters. In other words, the feasible range of gravity current fronts (limits of the range of Froude for a given height ratio) seen in the experiments here, in BS and Keulegan (1958), could be established quantitatively from theory.

7.4 Turbidity Currents

The most challenging experiments to be run, however, are those involving a nonconservative contaminant (sediment). These fronts will most likely be much more difficult to produce and to measure. Difficulties of settling in the pipes of the flume leading to the channel, settling before the front and contamination of the clear tank are two of the problems that need to be addressed before data acquisition can start. Different measurement techniques, such as particle image velocimetry (PIV), optical probes, *etc.*, might have to be sought out in order to produce quality results. The basic theory will also have to be manipulated in order to account for the change in concentration due to settling and erosion. No experiment has ever been attempted to study turbidity currents in this way which makes data acquisition, as well as the basic analysis, very difficult and challenging.

However, in order to study turbidity currents and their behavior properly, such an experiment needs to be done. The knowledge of the heads of turbidity currents is primitive to say the least. Most of the work done today totally ignores the head and its complexities, or simply assumes the head as a continuation of the body of the current. These simplifications, though necessary today, could be easily avoided with a simple model for the head, like the one formulated here for saline currents. All that would be needed to be added would be a term that accounts for the settling flux (or erosive flux) of the contaminant.

Finally, confirmation of all of the laboratory work of the turbidity current study should be made with field observations. This project was a part of a larger research effort in which the goal

was to decipher the sedimentary record of oceanic beds. Turbidity currents have a major role in laying down these sedimentary layers. Future work should be attempted that integrates the newly formulated head-mixing model with the previously formulated codes (as mentioned in the previous paragraph) for the body. After some calibration tests, the final model should attempt to duplicate field data of sedimentary layers where turbidity currents dominate sedimentation processes. Work should be continued for a wide range of shelf-slope geometries and sediment types.

REFERENCES

Adrian, R. J. (1991) Particle imaging techniques for experimental fluid mechanics. *Ann. Rev. Fluid Mech.*, **23**, 261-304.

Alavian, V. (1986) Behavior of density currents on an incline. *J. Hydr. Engrg.*, **112(1)**, 27-42.

Allen, J. R. L. (1971) Mixing at turbidity current heads, and its geologic implications. *J. Sedimentary Petrology* **41**, 97-113.

Altinakar, M. S., Graf, W. H. and Hopfinger, E. J. (1990) Weakly depositing turbidity current on a small slope. *J. Hydr. Res.*, **28(1)**, 55-80.

Arita, M. and Jirka, G. H. (1987) Two-layer model of saline wedges I: Entrainment and interfacial friction. *J. Hydr. Engrg.*, **113(10)**, 1229-1248.

Bagnold, R. A. (1974) Fluid forces on a body in shear-flow; experimental use of stationary flow. *Proc. Roy. Soc. London, Ser. A.*, **340**, 147-171.

Bendat, J. S. and Piersol, A.G. (1986) *Random data: Analysis and measurement procedures.* 2nd Edition. Wiley-Interscience, New York.

Benjamin, T. B. (1968) Gravity currents and related phenomena. *J Fluid Mech.*, **31(2)**, 209-248.

Britter, R. E. and Simpson, J. E. (1978) Experiments on the dynamics of gravity current head. *J. Fluid Mech.*, **88(2)**, 223-240.

Drazin, P. G. and Reid, W. H. (1981) *Hydrodynamic stability.* Cambridge University Press. New York.

Denton, R. A. (1990) Accounting for density front energy losses. *J. Hydr. Engrg.*, **116(2)**, 270-275.

García, M. H. (1992) "Turbidity currents". In: *Encyclopedia of Earth System Science*, Academic Press, Inc. **4**, 399-407.

García, M. H. (1993) Hydraulic jumps in sediment-driven bottom currents. *J. Hydr. Engrg.*, **119(10)**, 1094-1117.

Giger, M., Dracos, T. and Jirka, G. H. (1992) Plane turbulent jets in a bounded fluid layer. *J. Fluid Mech.*, **241**, 587-614.

Goldstein, R. J. (1983) *Fluid mechanics measurements.* Hemisphere, Washington, D. C.

Guilbault, G. G. (1973) *Practical fluorescence: Theory, methods and techniques.* Dekker, New York.

Hay, A. E. (1983) On the frontal speeds of internal gravity surges on sloping boundaries. *J. Geophys. Res.*, **88(C1)**, 751-754.

Hay, A. E. (1987) Turbidity currents and submarine channel formation in Rupert Inlet, British Columbia. *J. Geophys. Res.*, **92**, 2875-2881.

Harleman, D. R. F. (1961) "Stratified flow". In: *Handbook of fluid mechanics*. McGraw-Hill, Chicago.

Head, M. J. (1984) The use of miniature four-electrode conductivity probes for high resolution measurement of turbulent density or temperature variations in salt-stratified water flows. PhD Thesis, University of California, San Diego.

Inman, D. L., Nordstrum, C. E., and Flick, R. E. (1976) Currents in submarine canyons: an air-sea-land interaction. *Ann. Rev. Fluid Mech.*, **8**, 275-310.

Jirka, G. H. and Arita, M. (1987) Density currents or density wedges: boundary-layer influence and control methods. *J. Fluid Mech.*, **177**, 187-206.

Karman, T. von (1940) The engineer grapples with nonlinear problems. *Bull. Am. Math. Soc.*, **46**, 615-683.

Keulegan, G. H. (1957a) An experimental study of the motion of saline water from locks into fresh water channels. *U.S. Nat. Bur. Stand. Rep.* no. 5168.

Keulegan, G. H. (1957b) Form characteristics of arrested saline wedges. *U.S. Nat. Bur. Stand. Rep.* no. 5482.

Keulegan, G. H. (1958) The motion of saline fronts in still water. *U.S. Nat. Bur. Stand. Rep.* no. 5831.

Kraus, N. C., Lohrmann, A. and Cabrera, R. (1994) New acoustic meter for measuring 3D laboratory flows. *J Hydr. Engrg.*, **120(3)**, 406-412.

Middleton, G. V. (1966) Experiments on density and turbidity currents 1. Motion of the head. *Can. J. Earth Sci.*, **3**, 523-546.

Normark, W. R. and Dickson, F. H. (1976) Sublacustrine fan morphology in Lake Superior. *Am.Assoc.Petroleum Geologists Bull.*, vol. 60. no. 7.

Nowell, A. R. M. (1978) Dissipation and fine-scale structure in turbulent open channel flow. *Water Resour. Res.*, **14(3)**, 519-526.

Simoens, S. and Ayrault, M. (1994) Concentration flux measurements of a scalar quantity in turbulent flows. *Exp. in Fluids*, **16**, 273-281.

Simpson, J. E. (1969) A comparison between laboratory and atmospheric density currents. *Quart. J. Roy. Met. Soc.*, **95**, 758-768.

Simpson, J. E. (1972) Effects of the lower boundary on the head of a gravity current. *J. Fluid Mech.*, **53(4)**, 759-768.

Simpson, J. E. and Britter, R. E. (1979) The dynamics of the head of a gravity current advancing over a horizontal surface. *J. Fluid Mech.*, **94(3)**, 477-495.

Simpson, J. E. (1986) Mixing at the front of a gravity current. *Acta Mechanica*, **63**, 245-253.

Simpson, J. E. (1987) *Gravity currents in the environment and in the laboratory*. John Wiley and Sons, New York.

Sullivan, G. D. and List, E. J. (1994) On mixing and transport at a sheared density interface. *J. Fluid Mech.*, **273**, 213-239.

Tamburrino, A. and Gulliver, J. S. (1992) Comparative flow characteristics of a moving-bed flume. *Exp. in Fluids*, **13**, 289-298.

Taylor, G. I. (1950) The instability of liquid surfaces when accelerated in a direction perpendicular to their planes. *Proc. Roy. Soc. London, Ser. A*, **201**, 192-196.

Tennekes, J. L. and Lumley, H. (1972) *A first course in turbulence*. MIT Press, Cambridge, MA.

Teseker, E. (1969) Uniform turbidity currents. PhD Thesis, University of Norway.

Thomas, N. H. and Simpson, J. E. (1985) Mixing of gravity currents in turbulent surroundings: laboratory studies and modeling implications. In: *Turbulence and diffusion in stable environments*. Clarendon Press, Oxford.

Thorpe, S. A. (1969) Experiments on the instability of stratified shear flows: immiscible fluids. *J. Fluid Mech.*, **39**, 25.

Thorpe, S. A. (1971) Experiments on the instability of stratified shear flows: miscible fluids. *J. Fluid Mech.*, **46**, 299-319.

Thorpe, S. A. (1973) Experiments on instability and turbulence in a stratified shear flow. *J. Fluid Mech.*, **61**, 731-751.

Tsihrintzis, V. A. (1988) Theoretical and experimental investigation of three-dimensional boundary-attached density currents. PhD Thesis, University of Illinois at Urbana-Champaign.

Turner, J. S. (1973) *Buoyancy effects in fluids*. Cambridge University Press, New York.

Walker, D. A. (1987) A fluorescence technique for measurement of concentration in mixing liquids. *J. Phys. E: Sci. Instrum.*, **20**, 217-224.

Wood, I. R. and Simpson, J. E. (1984) Jumps in layered miscible fluids. *J. Fluid Mech.*, **140**, 329-342.

APPENDICES

Appendix 1 - Moving Bed Experiments

Exp Number	Oncoming Velocity (U1); cm/s	Excess Density Difference (g'/g)	Flow Depth (h1); cm	Visible Current Ht. (h5); cm	Front Height (hf); cm	Temperature (T); deg C	Inflow per Unit Width of Dense Fluid (q); cm^2/s	Weir Height cm
15	9.0	0.012	39.0	4.0	15.0	15.6	19.6	30
18	9.9	0.014	39.4	3.5	13.0	14.4	16.4	30
20	10.2	0.020	39.4	2.0	6.0	13.3	5.9	30
23	8.9	0.016	46.8	2.5	9.0	13.9	5.9	38
24	8.3	0.010	46.7	3.3	14.0	13.3	9.9	38
25	8.6	0.008	46.9	4.5	18.0	13.3	20.9	38
30	11.7	0.031	30.3	2.5	8.0	18.9	6.8	22
31	11.4	0.025	30.6	3.5	9.5	16.4	11.2	22
34	9.0	0.017	38.6	2.0	7.5	17.8	5.4	30
36	9.0	0.014	38.6	3.5	13.0	18.2	10.7	30
37	9.5	0.012	39.6	4.5	15.5	18.2	17.9	30
38	9.0	0.015	38.7	3.5	11.0	16.0	10.4	30
39	9.5	0.018	38.8	2.3	7.5	20.0	7.4	30
40	9.0	0.012	38.7	3.6	13.0	18.1	13.1	30
41	7.9	0.010	46.7	2.2	10.0	17.6	7.6	38
42	8.3	0.013	47.0	1.6	8.0	18.0	3.4	38
43	8.3	0.006	47.1	5.5	19.0	19.3	23.4	38
45	9.0	0.018	38.6	2.2	8.0	18.6	4.8	30
56	11.7	0.028	30.7	3.4	10.5	14.7	8.1	22
57	11.7	0.025	30.8	4.0	13.3	15.3	13.1	22
59	5.9	0.013	19.6	1.7	6.0	13.6	2.0	15
60	5.9	0.010	19.7	2.4	6.5	13.5	2.1	15
61	7.6	0.018	20.4	2.3	7.4	14.4	2.9	15
63	7.6	0.018	20.4	1.5	5.0	15.1	1.7	15

Appendix 2 - Fixed Bed Experiments

Exp Number	Oncoming Velocity (U1); cm/s	Excess Density Difference (g'/g)	Flow Depth (h1); cm	Visible Current Ht. (h5); cm	Front Height (hf); cm	Temperature (T); deg C	Inflow per Unit Width of Dense Fluid (q); cm^2/s	Weir Height cm
49	9.03	0.015	38.59	3.8	14.5	15.3	10.45	30
50	9.03	0.019	38.65	3.6	11.0	17.0	7.31	30
51	9.03	0.021	38.56	2.9	9.0	15.6	5.33	30
52	9.03	0.013	38.59	6.0	17.5	16.5	15.42	30
53	9.03	0.023	38.47	2.7	9.5	15.0	4.13	30
54	8.28	0.011	46.91	4.0	12.5	15.6	6.13	38
55	8.28	0.012	47.03	3.4	12.0	15.9	5.94	38

Experiment number	Height above bed (cm)	Streamwise velocity (cm/s)	Transverse velocity (cm/s)	Vertical velocity (cm/s)	TKE (cm^2/s^2)
EXP30	20.27	14.14	0.48	1.04	3.31
	18.16	14.77	0.20	1.74	4.32
	16.05	14.95	-0.01	2.15	4.21
	11.17	15.83	-1.00	1.84	4.67
	7.68	16.70	-2.37	2.17	6.23
	7.25	16.23	-2.61	2.54	9.46
	6.71	15.83	-2.84	2.22	5.51
	6.08	15.70	-2.57	2.74	8.40
	5.09	13.48	-2.04	2.01	5.74
	3.82	5.40	-1.07	0.41	3.71
	2.93	4.06	-1.30	0.05	34.16*
	2.02	0.06	-0.39	0.14	5.56
	1.17	-1.03	0.20	-0.16	2.05
	0.95	-2.69	0.04	-0.21	2.10
EXP34	27.28	10.92	-0.53	0.44	1.96
	22.80	11.25	-0.97	0.83	2.02
	19.25	11.34	-1.10	0.72	1.74
	14.69	11.75	-1.46	0.59	1.96
	9.70	11.97	-1.10	0.67	2.36
	7.45	11.84	-0.85	1.32	8.70
	5.40	6.86	-1.07	0.60	6.03
	4.09	3.67	-0.66	0.43	4.79
	2.39	1.58	0.37	-0.53	393.98*
	1.28	-0.97	0.25	0.26	4.11
	0.67	-2.49	0.15	0.09	1.56
EXP36	25.42	12.53	-0.83	1.12	2.28
	22.55	12.99	-0.76	0.68	1.89
	19.77	13.32	-0.71	0.51	2.55
	17.38	12.52	-0.78	-0.04	2.26
	15.61	12.58	0.04	-0.01	2.94
	13.81	12.23	-0.41	0.04	3.96
	12.54	13.08	-0.45	-0.17	5.19
	11.26	13.22	-0.20	0.25	8.11

Experiment number	Height above bed (cm)	Streamwise velocity (cm/s)	Transverse velocity (cm/s)	Vertical velocity (cm/s)	TKE (cm^2/s^2)
EXP36	9.47	11.14	-0.02	0.34	8.88
	7.66	6.34	0.15	0.17	18.74*
	5.15	0.93	0.33	0.09	69.73*
	3.14	-2.56	0.97	-0.54	339.88*
	2.47	-1.42	1.53	-0.07	745.37*
	1.49	-3.11	-0.09	0.04	5.69
	0.88	-3.10	-0.04	-0.05	3.28
	0.48	-2.81	-0.05	0.02	3.33
EXP37	27.37	14.09	-0.49	1.01	2.20
	24.63	14.88	-0.70	1.40	2.73
	20.88	15.33	-0.99	1.18	3.27
	18.24	14.91	-0.40	1.25	3.11
	16.11	15.14	0.07	2.43	3.74
	13.55	13.50	0.21	1.47	7.37
	11.24	9.20	0.22	1.35	6.18
	8.04	2.82	0.00	0.51	8.41
	5.75	-0.70	-0.13	0.04	7.13
	3.86	-2.06	-0.07	-0.06	23.06*
	1.57	-2.68	-0.09	-0.17	2.75
	0.55	-1.92	-0.15	-0.19	2.25
EXP38	26.86	12.01	0.30	0.96	1.73
	24.65	11.94	0.09	1.22	1.79
	18.65	13.11	-0.33	1.22	2.04
	15.20	13.30	0.28	1.11	2.01
	13.16	13.94	0.13	0.94	2.60
	11.19	13.63	-0.24	0.27	3.87
	8.31	7.80	0.23	0.11	8.04
	6.04	1.86	0.39	0.14	4.73
	4.35	-0.41	-0.18	0.29	2.71
	2.60	-2.26	-0.16	0.17	1.38
	1.84	-2.83	0.10	0.00	1.89
	0.78	-3.35	0.12	0.20	0.72

Experiment number	Height above bed (cm)	Streamwise velocity (cm/s)	Transverse velocity (cm/s)	Vertical velocity (cm/s)	TKE (cm^2/s^2)
EXP39	29.31	11.71	-0.29	0.71	2.50
	21.23	11.63	-0.60	1.18	2.17
	14.95	12.70	-0.85	1.21	2.10
	10.77	13.01	-0.58	1.85	2.14
	7.64	13.34	0.10	2.05	2.13
	6.70	12.91	-0.66	2.11	4.17
	4.63	4.73	0.26	0.40	5.14
	3.79	2.23	0.12	0.34	4.20
	2.94	0.42	0.15	0.11	2.88
	2.16	-0.87	0.42	0.47	3.25
	0.77	-3.32	0.03	0.04	2.06
EXP40	29.29	13.15	0.32	1.20	1.61
	22.81	13.63	-0.65	1.34	1.54
	19.21	14.08	-0.88	1.27	1.70
	16.33	14.71	-0.33	0.56	2.32
	13.24	13.82	-0.32	0.78	5.05
	11.53	9.61	-0.13	0.44	5.57
	9.19	4.93	0.32	0.21	5.97
	6.54	0.83	-0.20	0.28	3.25
	4.21	-1.70	-0.16	0.49	2.43
	2.20	-2.95	-0.08	-0.06	1.17
	0.85	-2.80	0.24	-0.05	0.65
EXP41	30.52	9.91	-0.29	0.83	1.33
	25.10	9.65	-0.26	0.47	1.52
	19.77	9.12	-0.36	0.11	1.07
	13.70	9.87	0.33	0.70	1.02
	10.93	10.31	0.60	0.84	1.30
	8.90	10.38	0.81	1.04	1.49
	7.05	7.49	0.91	0.85	4.83
	6.45	6.73	0.61	1.09	5.15
	5.53	3.80	0.46	0.92	4.72
	3.90	1.05	0.14	0.03	2.00
	2.17	-1.26	-0.06	0.00	1.14
	1.45	-2.08	-0.08	0.01	0.38

Experiment number	Height above bed (cm)	Streamwise velocity (cm/s)	Transverse velocity (cm/s)	Vertical velocity (cm/s)	TKE (cm^2/s^2)
EXP41	0.58	-2.48	-0.09	-0.04	0.75
EXP42	25.63	9.26	-0.45	0.49	1.06
	20.21	9.33	-0.36	0.61	1.25
	12.16	9.47	0.29	0.92	1.20
	9.18	9.87	0.64	1.46	1.19
	8.26	9.86	0.42	1.34	1.62
	7.25	10.43	1.43	1.58	1.89
	6.37	8.25	0.86	1.22	4.33
	5.27	7.89	0.82	1.51	4.71
	3.95	3.56	0.64	0.20	3.26
	2.50	0.72	0.14	0.07	1.72
	1.59	-1.25	-0.01	-0.07	0.90
	1.13	-1.07	0.09	-0.03	0.71
	0.52	-1.83	-0.04	-0.15	0.60
EXP43	31.62	12.77	0.24	0.44	1.43
	25.97	12.28	-0.09	1.00	1.26
	21.47	11.82	0.26	0.84	1.24
	19.18	12.07	0.40	1.11	1.56
	15.72	11.80	0.62	1.69	1.83
	12.10	7.48	0.78	0.67	3.97
	8.27	1.95	-0.82	0.17	3.45
	5.21	-2.11	-0.62	0.10	1.23
	3.10	-2.64	-1.07	0.51	2.15
	1.02	-2.88	-0.68	-0.18	0.66
EXP45	27.62	11.55	-0.23	0.75	1.69
	20.74	12.13	-0.68	0.79	1.88
	15.57	12.14	-0.26	0.37	2.17
	11.59	11.95	0.28	0.03	2.19
	9.49	12.75	0.38	0.98	2.77
	7.90	13.05	0.11	1.72	2.23
	6.25	10.89	0.31	1.39	6.71
	5.30	4.33	0.53	0.20	7.58

Experiment number	Height above bed (cm)	Streamwise velocity (cm/s)	Transverse velocity (cm/s)	Vertical velocity (cm/s)	TKE (cm^2/s^2)
EXP45	4.06	2.10	0.15	-0.07	4.30
	2.79	1.18	0.06	0.10	4.01
	1.83	-0.95	0.36	0.12	2.01
	0.80	-2.89	0.15	0.16	1.03

Experiment number	Streamwise RMS (cm/s)	Transverse RMS (cm/s)	Vertical RMS (cm/s)
EXP30	1.55	1.43	1.49
	2.04	1.57	1.42
	1.87	1.57	1.57
	1.70	2.03	1.53
	2.19	2.44	1.31
	2.33	3.42	1.34
	1.96	2.33	1.32
	2.60	2.78	1.53
	2.54	1.92	1.17
	1.94	1.64	0.99
	5.83*	5.67*	1.48*
	2.41	2.02	1.10
	1.72	0.90	0.58
	1.39	1.39	0.58
EXP34	1.09	1.18	1.16
	1.20	1.13	1.14
	1.10	1.07	1.07
	1.30	1.14	0.97
	1.34	1.32	1.09
	2.23	3.34	1.14
	2.63	1.87	1.29
	2.26	1.79	1.13
	19.99*	19.26*	4.15*
	2.11	1.61	1.08
	1.17	1.14	0.67
EXP36	1.28	1.33	1.06
	1.27	1.10	0.98
	1.39	1.41	1.09
	1.42	1.21	1.03
	1.68	1.44	1.00
	1.63	2.09	0.94
	2.28	1.96	1.17
	2.66	2.74	1.29

Experiment number	Streamwise RMS (cm/s)	Transverse RMS (cm/s)	Vertical RMS (cm/s)
EXP36	3.17	2.54	1.11
	4.49*	3.93*	1.38*
	8.25*	8.21*	2.00*
	16.91*	19.54*	3.50*
	25.53*	28.51*	5.13*
	2.45	2.25	0.56
	1.94	1.61	0.49
	1.87	1.71	0.49
EXP37	1.38	1.28	0.92
	1.51	1.47	1.03
	1.72	1.49	1.16
	1.68	1.40	1.19
	1.58	1.92	1.13
	2.43	2.60	1.43
	2.53	2.06	1.31
	3.02	2.57	1.07
	2.59	2.64	0.77
	4.58*	4.89*	1.12*
	1.63	1.55	0.67
	1.55	1.39	0.41
EXP38	1.24	1.00	0.97
	1.25	1.04	0.96
	1.33	1.10	1.05
	1.24	1.33	0.85
	1.55	1.27	1.09
	1.73	1.69	1.38
	3.11	2.06	1.48
	2.23	1.65	1.33
	1.59	1.28	1.12
	1.08	1.00	0.76
	1.46	0.92	0.89
	0.82	0.76	0.43

Experiment number	Streamwise RMS (cm/s)	Transverse RMS (cm/s)	Vertical RMS (cm/s)
EXP39	1.31	1.39	1.16
	1.38	1.14	1.06
	1.19	1.25	1.11
	1.47	1.18	0.85
	1.35	1.28	0.89
	1.99	1.70	1.22
	2.12	2.11	1.16
	2.08	1.56	1.27
	1.46	1.61	1.02
	1.52	1.60	1.28
	1.58	1.01	0.76
EXP40	1.14	1.03	0.93
	1.17	0.93	0.92
	1.24	1.03	0.90
	1.47	1.24	0.98
	2.11	1.81	1.54
	2.44	1.76	1.44
	2.60	1.84	1.34
	1.84	1.31	1.18
	1.31	1.49	0.96
	1.03	0.74	0.85
	0.87	0.64	0.37
EXP41	0.92	1.00	0.90
	1.09	1.09	0.82
	0.85	0.82	0.87
	0.82	0.93	0.72
	1.10	0.84	0.83
	1.22	0.82	0.90
	2.55	1.41	1.08
	2.74	1.37	0.96
	2.37	1.57	1.17
	1.31	1.13	0.99
	1.10	0.77	0.68
	0.57	0.52	0.40

Experiment number	Streamwise RMS (cm/s)	Transverse RMS (cm/s)	Vertical RMS (cm/s)
EXP41	1.02	0.55	0.38
EXP42	0.86	0.96	0.68
	1.11	0.83	0.76
	1.04	0.94	0.66
	0.95	0.90	0.82
	1.29	0.80	0.97
	1.29	1.10	0.95
	2.34	1.35	1.18
	2.47	1.39	1.19
	1.95	1.39	0.89
	1.32	1.11	0.67
	0.81	0.84	0.67
	0.83	0.63	0.59
	0.81	0.54	0.51
EXP43	1.02	0.96	0.95
	1.02	0.92	0.80
	1.03	0.80	0.87
	1.08	1.01	0.96
	1.10	1.13	1.08
	2.12	1.53	1.07
	1.77	1.64	1.03
	1.00	1.00	0.68
	1.28	1.12	1.18
	0.74	0.74	0.50
EXP45	1.01	1.17	1.00
	1.09	1.12	1.15
	1.22	1.22	1.17
	1.15	1.38	1.07
	1.50	1.37	1.19
	1.21	1.50	0.87
	2.82	1.89	1.37
	3.03	2.00	1.42

Experiment number	Streamwise RMS (cm/s)	Transverse RMS (cm/s)	Vertical RMS (cm/s)
EXP45	1.99	1.71	1.30
	2.10	1.49	1.18
	1.31	1.20	0.94
	0.97	0.80	0.69